A new independent age model for type-Maastrichtian chalk near Hallembaye (Gulpen Formation, Upper Cretaceous) using a cyclostratigraphic approach based on X-ray fluorescence data

Jarno J.C. Huygh

Master Thesis – Master of Science in Chemistry

Promotor: Prof. Dr. Philippe Claeys

Supervisors: Dr. Johan Vellekoop, Dr. Matthias Sinnesael, Pim Kaskes

Academic year 2020 – 2021

Acknowledgements

First and foremost, I'd like to thank Prof. Dr. Philippe Claeys for giving me the opportunity to carry out my master thesis in the department of Analytical, Environmental and Geo- Chemistry (AMGC). It has been another great experience for me, being able to pick up where I left off for my bachelor thesis. Thank you for helping in creating such a welcoming environment, for broadening my horizon and for all your support. Secondly I'd like to thank Prof. Dr. Anne-Christine da Silva for welcoming me at ULiège to learn about magnetic susceptibility and giving me access to carry out my own magnetic susceptibility measurements. Thanks for always being available and the valuable feedback, it has been a pleasure to learn from you.

I'd also like to acknowledge the International Association of Sedimentologists (IAS) for their support and for financing part of this master thesis through the Judith McKenzie Field Work grant. Even when field works could no longer be planned due to the ongoing Covid-19 pandemic, continued support was provided by the IAS nevertheless – even out of the original scope of the grant.

A very, very big "thank you" goes out to my supervisors Dr. Johan Vellekoop, Dr. Matthias Sinnesael and Pim Kaskes. It's been a privilege working with you again for the past year and I'm very grateful for your support – both on a technical and on a human level. Thanks for believing in me, thanks for sharing your expertise, thanks for pushing me out of my comfort zone and introducing me to IAS, EGU and the world of cyclostratigraphy (and everything around it). I really appreciate the freedom you've given me and the opportunities you've helped creating. I've been in the most luxurious situation, with support of three specialists each in their own field showing me the ropes. I'd also like to thank David Verstraeten for once again contributing to a nice laboratory environment to work in and for being available whenever help, explanations or assistance was needed. Similarly, I'd like to thank Prof. Dr. ir. Christophe Snoeck for the lab tours, helping out with lab resources and planning, and for sticking around late which gave me some additional, much-needed flexibility. Lastly, I'd like to thank Prof. Dr. Steven Goderis and everyone else at AMGC for being so welcoming, for all the nice chats and the support.

"Not everyone walks the same path" is what Philippe said when he welcomed me – and he couldn't have been more right. I've been given the chance to interrupt my working career in order to pursue my dream of continuing my academic studies, for which I'd like to thank my employer. I'd also like to express my utmost gratitude and respect to my colleague, mentor and friend Muhiddin Elguweri. Thanks to you, I really started believing in myself and my capabilities, and got the confidence and motivation needed to take this big step in my life. Of course, I'd also like to thank my parents who've welcomed me back home and supported me throughout my studies, and finally this master thesis. Thanks to you, I had next to no worries which allowed me to focus 100% on my goals. When you're 19 years old, you take your parents and everything they do for you for granted. When you're 29 years old, you realize how lucky you are they're still there to support you through thick and thin. Last, but not least, I'd like to thank all my friends who have been my greatest support and biggest supporters. Thanks for listening to my stories of how the movement of planets can affect the chemical composition of little rocks. Thanks for being the silver linings during this mess of a pandemic that even caused the most interesting research to become a challenge from time to time.

Abstract

Cyclostratigraphic analyses of Upper Cretaceous chalk successions, based on high-resolution geochemical data, has proven successful for dating and correlating rock strata. However, this approach has not yet been applied in the type-Maastrichtian area in the southeastern part of the Netherlands and northeastern Belgium – which would put its rich paleontological record better in time . Even though other apparent cyclic variations, such as changes in bioclast compositions and suggested Milankovitch-paced flint cycles, already have been used to build a tentative cyclostratigraphic age model for the type-Maastrichtian, the interpretation of these signals is rather complex. This Master dissertation is a contribution towards the Maastrichtian Geoheritage Project, presenting a new high-resolution (5 cm) micro X-ray fluorescence geochemical dataset and cyclostratigraphic interpretation of the type-Maastrichtian chalk elemental composition of the Gulpen Formation. The selected, continuous interval of 22.75 m is characterized by a gradual increase in chalk purity and corresponding increase in flint occurrence. A methodological assessment was carried out for micro X-ray fluorescence measurements on type-Maastrichtian chalk. In addition, finetuning of magnetic susceptibility measurements on type-Maastrichtian chalk was carried out and the potential of magnetic susceptibility as a proxy for terrigenous material was explored.

Analyses of the geochemistry of the type-Maastrichtian chalk yielded an immense dataset on the major and trace elemental composition. Concentration of calcium and silicium reflect the main lithological variations observed in the section and can potentially even be related to early-diagenetic formation of flints. Other elements, such as terrigenous potassium, aluminium and titanium reveal insight in the amount of detrital influx into the carbonate sediment. Even though indications are present of a diagenetic alteration of the record, the diagenesis-resistant Ti/Al serves as a proxy for changes in the detrital cycle.

A new, independent astronomical age model for the Vijlen Member and part of the Lixhe 1 Member type-Maastrichtian chalk exposed at the Kreco quarry near Hallembaye was developed based on a cyclostratigraphic approach using the Ti/Al ratio as proxy for variations in terrigenous input. The ~20 kyr precession, ~40 kyr obliquity and ~125 kyr short-eccentricity cycles were identified in the record using a variety of tools, including spectral analyses and time series analysis. The investigated interval, encompasses about 1.12 Myr based on astronomical tuning using the ~40 kyr obliquity Milankovitch cycle. This new floating astronomical time scale was anchored based on newly developed carbon isotope-based chemostratigraphy, which was used to correlate the type-Maastrichtian chalk exposed at the Kreco (and ENCI) quarry with time-equivalent, astronomically dated sections at Gubbio (Italy) and the Stevns-1 core (Denmark). The basis of the Vijlen Member at the Kreco quarry was dated to 70.4 Ma based on chemostratigraphy, revealing that the Vijlen Member and part of the Lixhe 1 Member were deposited from roughly 70.40 Ma to 69.25 Ma. The anchored astronomical time scale provides an updated age model for the Gulpen Formation and enables correlation with Maastrichtian sections around the world. This way, dating of important events such as extinctions, periods of increased volcanism and tectonic activity is made possible. In addition, insight is obtained in global and/or regional processes such as sea level fluctuations, changes in fauna and flora, climate change and their driving mechanisms.

Table of Contents

1. Introduction

Cyclostratigraphy is a subdiscipline of stratigraphy that relates astronomically forced changes of the paleoclimate and paleoenvironment to changes in the sedimentary record (Strasser et al. 2006; Hinnov 2013; Sinnesael et al. 2019). Typically, it is attempted to link a changing paleoclimate, recorded as a primary signal by proxies such as the sedimentary elemental composition, to changing astronomical parameters of the Earth – the so-called Milankovitch cycles – that induces quasi-periodic changes in Earth's past climate (Sinnesael et al. 2019). This way, cyclostratigraphy is a powerful tool that has the potential to provide an independent age model via the construction of high-resolution astronomical timescales (Strasser et al. 2006; Hinnov 2013; Sinnesael et al. 2019). Once established, the astronomical timescale provides high-resolution absolute dating when "anchored", meaning its linked to an established absolute timeframe obtained e.g. via radiometric dating (Strasser et al. 2006). Alternatively, when no such framework exists – or if it is not well constrained – cyclostratigraphy can be used for constructing high-resolution "floating" timescales (Strasser et al. 2006), which is of high interest for periods in deeper geological time such as the Cretaceous. The Cretaceous (or "Krijt" in Dutch) is named after the abundant amount of chalk (or "krijt" in Dutch) that was deposited during this Period.

The Late Cretaceous is of interest within the geological community most notably for the mass extinction at the Cretaceous-Paleogene boundary (Chiarenza et al., 2020), which marked the end of the Maastrichtian as latest age of the Late Cretaceous (Gradstein and Ogg, 2020). Especially the Chicxulub impact event is believed to have played a major role in the latest mass extinction event, which also led to the demise of the non-avian dinosaurs (Chiarenza et al., 2020; Goderis et al., 2021). Another event believed to have contributed to changes in the paleoclimate was the Deccan Traps volcanism, which left its signature in the global sedimentary record of the Upper Cretaceous (Font et al., 2018). Moreover, the Late Cretaceous was also characterized by drastic changes in sea level (Håkansson et al. 1974) and a progressively cooling global climate, albeit with cooler and warmer fluctuations (Thibault et al., 2016).

A large variety of work has already studied the Late Cretaceous climate using a plethora of proxies and different stratigraphic approaches, applied on sections such as Kronsmoor, Germany (Engelke et al., 2018; Voigt and Schönfeld, 2010), the Stevns-1 core from Denmark (Thibault et al. 2012; Voigt et al. 2012; Surlyk et al. 2013), at Zumaia, Spain (ten Kate and Sprenger 1993; Batenburg et al. 2014), at Gubbio, Italy (Voigt et al. 2012; Sinnesael et al. 2016; Sinnesael et al. 2019). However, the age equivalent sections located in the Netherlands/Belgium border area, i.e. the regional where the Maastrichtian Stage was originally defined, have not yet been investigated using latest developments – while this region is known as the type-Maastrichtian area.

Named after the area around the city of Maastricht (The Netherlands), the Maastrichtian finds its origin in the type-area sedimentary record initially named 'système maestrichtien' by Dumont in 1849 (Jagt et al. 2003). Already having provided a wealth of knowledge in the past, e.g. the discovery of mosasaur fossils already in 1770 (Gallagher et al., 2004; Zijlstra, 1994), the Type-Maastrichtian chalk potentially has more secrets to be unlocked. Being a contribution towards the Maastrichtian Geoheritage Project, this master thesis aims at characterizing and analyzing the type-Maastrichtian chalk before this geological heritage becomes inaccessible. So far, preliminary age models for the type-Maastrichtian chalk are based on biostratigraphy and the apparent Milankovitch-paced flint cycles (Zijlstra, 1994) and variations in bioclast composition used for the application of cyclostratigraphy (Felder 1997; Keutgen 2018). These age models remain questionable however, especially because of bioprovincialism and presence of hiatuses (Felder et al. 2003; Vellekoop et al. In prep.). The work of for example Engelke et al. (2018) on the Kronsmoor section has proven that high-resolution geochemical datasets can successfully be used to construct an improved astrochronological age model for Late Cretaceous chalk successions via identified obliquity and long-eccentricity Milankovitch cycles. In addition, insight in changes of sea level, paleotemperatures, obliquity-forced dust influx etc. was obtained (Engelke et al., 2018).

In this work, focus is put on the chalk succession from the Vijlen and Lixhe 1 Members of the Gulpen Formation exposed at the Kreco quarry near Hallembaye (Belgium), deposited during the Maastrichtian (Late Cretaceous) roughly 70 million years ago (Ma) (Keutgen 2018). By analyzing the chalk using X-ray fluorescence, it is investigated whether visual observations such as chalk color and flint occurrence – either scattered as individual nodules or as true flint layers – are reflected by the elemental composition. A similar, exploratory study will be carried out by analyzing the chalk magnetic susceptibility signal. Based on these geochemical and geophysical measurements, it will be assessed whether astronomical forcing of the paleoclimate was translated as a primary signal into the type-Maastrichtian chalk record from the Kreco quarry and, if so, suitable proxies for the application of cyclostratigraphy can be identified. In addition, it is investigated to which extent the chalk geochemistry reveals information on the flint-formation. This way, it is assessed if flint occurrence in the chalk corresponds to a primary, astronomically forced signal.

Finally, the current age model for the type-Maastrichtian chalk for these Members is improved using a cyclostratigraphic approach based on high resolution geochemical datasets. This improved age model will contribute to geochronology and will further help constraining existing uncertainties when included in an integrated stratigraphic approach, for example when combined with the latest developments in carbon isotope-based chemostratigraphy (Vellekoop in prep., 2021). Using the chemostratigraphy, anchoring of a new age model is possible and will enable correlation between other aforementioned age-equivalent sections.

2. Background and Literature Review

2.1. Geochemistry of Carbonate Rocks

Carbonate rocks can be considered amongst the most abundant (bio)chemical sedimentary rocks on Earth. They can be subdivided based on their mineralogy, into limestones and dolomites (Boggs 2006). The rock sequence exposed at the Kreco quarry near Hallembaye is composed mainly of limestone, which in turn is composed primarily of calcite. From a chemical point of view, calcium (Ca^{2+}) and carbonate (CO_3^{2-}) ions dominate the composition of limestone, which is often represented using the formula $CaCO_3$ (Boggs, 2006).

Many other elements however, originating from different sources, can also be found in the limestone. Most commonly, the positive counter-ions to carbonate are calcium (Ca), magnesium (Mg) or a combination of both (Swart, 2015). However, as limestone often originates from calcareous skeletons of microorganisms, which tend to incorporate trace amounts of barium (Ba), strontium (Sr) as well as magnesium (Mg) in the calcite crystal lattice (Brand et al. 1998), it can easily be rationalized that small amounts of these elements are expected to be present in the limestone. Depending on the environmental composition and characteristics, other elements such as manganese (Mn), iron (Fe) and sulfur (S) can also be incorporated in the calcite mineral, in general in ionic form (Fantle et al. 2020). So-called terrigenous elements such as aluminum (Al), potassium (K), titanium (Ti) and even silicium (Si) that originate from non-carbonate sources such as silicate minerals (quartz, feldspars) and clay minerals, can also be present in the carbonate as a result of terrigenous influx, such as riverine input or aeolian dust (Boggs, 2006; da Silva et al., 2012).

Even though often referred to as carbonates, a more subtle terminology is applicable to very pure limestones. To be more precise, the micro crystalline or “micritic” limestones (Folk, 1959) of the Cretaceous found at the Kreco quarry are typically called “chalk”. The Cretaceous chalk is composed of micrometer-sized remains of planktonic algae, such as coccolithophores (Hancock, 1975) and has a soft nature and fine texture. Even though there is a considerable diversity in origin, composition and even nomenclature, in essence the limestones are composed mainly of calcium carbonate. For this reason, it is relevant to explore the chemistry of calcium carbonate formation, deposition and processes that affect them, such as diagenesis.

2.1.1. Chemistry of Calcium Carbonate Deposition

According to Henry’s law, an equilibrium exists between the carbon dioxide (CO_2) concentration in the atmosphere and in the water surface. The Henry solubility *H* for CO_2 is often defined by the ratio of the concentration of CO_2 in the aqueous phase to the partial pressure of CO_2 in the gas phase, as illustrated by formula (1) (Gao, 2019).

$$H = \frac{[CO_2]_{aq}}{p_{CO_2}} \quad (1)$$

The exchange of CO_2 between the atmosphere and ocean (solubility pump) depends not only on the amount of carbon dioxide present in both bodies, but also on the temperature and salinity of water. CO_2

is less soluble in warm, high-saline waters and vice versa, which is of importance when looking at the carbonic acid (H_2CO_3) – bicarbonate (HCO_3^-) – carbonate (CO_3^{2-}) equilibrium in water (2) (Swart, 2015).

$$CO_2 + H_2O \leftrightarrow H_2CO_3 \leftrightarrow H^+ + HCO_3^- \leftrightarrow 2H^+ + CO_3^{2-} \quad (2)$$

Based on Henry's law, the carbonic acid formation and the carbonic acid equilibrium (equation 2), it can easily be understood that the global amount of CO_2 as well as the ocean acidity determines the concentration of dissolved carbonate species in seawater. A higher CO_2 concentration will eventually lead to an increased amount of H^+. And, if ocean waters are more acidic, less CO_3^{2-} will be available in the water for the production of $CaCO_3$ (3)(Gao, 2019).

$$Ca^{2+}_{(aq)} + CO^{2-}_{3\,(aq)} \leftrightarrow CaCO_{3\,(s)} \quad (3)$$

Chemically formed $CaCO_3$ will precipitate as a result of a low solubility in water. Biochemically formed $CaCO_3$ on the other hand will first be incorporated in skeletons and shells of marine organisms. Marine organisms such coccolithophores (and to a lesser degree some pelagic foraminifera) have skeletons composed mainly of $CaCO_3$, which will accumulate at the seafloor upon their death as an ooze and subsequently lithify to form chalk (Friedman, 1996). Because of their huge numbers, disintegration of calcium-carbonate-secreting organisms has the potential to be a large source of carbonate sediment at the ocean floor. The many shallow, warm epicontinental seas of the late Cretaceous offered the ideal circumstances for the carbonate formation and consequently carbonate sedimentation, and, are therefore often called "carbonate factories" (Boggs, 2006). These carbonate factories were typically open, tropical shelf seas of moderate depth (up to roughly 250 m) and were quite abundant in the regions of what is now Western Europe (Friedman, 1996).

Aside from calcareous marine organisms, other species such as siliceous organisms (siliceous sponges) were also present in the carbonate factories (Friedman, 1996). Remains of these siliceous organisms became a source of biogenic silica in the chalk sea which was eventually incorporated in the sedimentary record, for example as cherts or flints (Friedman, 1996; Van Os et al., 1994).

2.1.2. Diagenesis and Occurrence of Flint and Chert in Carbonates

Carbonates often undergo considerable changes in mineralogy, structure and even chemical composition over time – a process that is referred to as diagenesis (Fantle et al. 2020). Diagenesis is very broad term for a large variety of processes, including but certainly not limited to dissolution, recrystallization, cementation, bioturbation, etc. (Fantle et al. 2020). Given the large variety of chemical species present in the carbonate (as briefly summarized in Chapter 2.1.), different diagenetic processes can alter the carbonates in many different ways before they are sampled for analysis in a cyclostratigraphic study. Given the chalk near Hallembaye holds silicium-containing material such as flints and cherts, either as nodules scattered throughout the carbonate matrix or as true beds, their importance in this work cannot be neglected (Friedman, 1996). They are especially relevant for the present study because flint bed occurrence has already been used in preliminary cyclostratigraphic studies (for example Zijlstra, 1994) – see Chapter 3.5.

From a mineralogical point of view, chert and flints are composed mainly of microcrystalline quartz (SiO_2) minerals (Boggs, 2006). As already touched upon before, silica found in carbonates can originate from detritus (e.g. clays) but can also be of biogenic nature (siliceous organisms) (Koutsoukos and Hart, 1990; Van Os et al., 1994). Even though the geochemistry can easily be unraveled via modern characterization techniques, the same cannot be said about the exact mechanisms of flint formation. A potential mechanism behind the formation of flints present in Upper Cretaceous chalk is proposed by Lindgreen et al (2011). The higher the acidity of epicontinental seas, the higher the amount dissolved calcite was ought to be. As a result, higher concentrations of solid silicium-containing material remain and eventually flocculate and crystallize to form flint layers or nodules. Whenever the acidity is lower, the quartz is rather integrated as nano-sized particles in the chalk matrix (Lindgreen et al., 2011). In any case, diagenetic processes are responsible for the evolution of silica leading to flint and chert formation in carbonates (Boggs, 2006; Hancock, 1975).

2.2. Paleoclimatology

Evidence of global climate changes in Earth's history can be found in sedimentary sequences in the stratigraphic record (Zachos et al. 2001). Whereas these climate changes were of natural origin in the geological past, nowadays human activities are becoming more and more the driving force behind rapid climate change (Rosenzweig and Neofotis, 2013). In order to be able to understand processes behind climate change and to assess its implications, not only on nature but also on society, research is needed both in the fields of climate modeling and paleoclimatology (Marshak, 2008).

The field of paleoclimatology studies local and/or global climate(s) in the geological past. A plethora of paleoclimate proxies exist, which are physical, chemical and biological materials that are found in geological records that can be associated to climatic or environmental parameters. The geochemical composition of rock samples found in the stratigraphic record can for example be unraveled using isotope systems or major and trace elemental analysis techniques, e.g. based on X-ray fluorescence, offering a multitude of geochemical proxies (Govin et al., 2012). Assessment of geophysical characteristics, e.g. based on the magnetic susceptibility of a material which depends on its mineralogical composition, also provides insight in a changing paleoclimate (Ellwood et al. 2003; da Silva et al. 2015).

Dating of the paleoclimatic record can be challenging, especially absolute dating. Application of radiochronology via radiometric dating of e.g. zircon minerals based on the uranium-thorium-lead system offers absolute dating of the record, but inherently has its limitations as well (Renne et al. 1998). This is especially true when analyzing sedimentary rocks where, if present at all, most of the usable minerals present will have an age corresponding to the parent source rock and not to the sedimentary rock. Relative dating of a paleoclimatic record, for example using biostratigraphy, has proven valuable for local or regional correlation, but often an integrated stratigraphic (e.g. including magnetostratigraphy) approach is required for the determination of chronostratigraphic units and the corresponding division of time (Gradstein and Ogg 2020).

Another method allowing for high-resolution dating of stratigraphic records is cyclostratigraphy. Whenever a link can be established between astronomical forcing of the climate and the recording of that primary signal in the record, cyclostratigraphy can be applied to link variations in proxies to Milankovitch cycles (see Chapter 2.3). Knowledge on the quasi-periodicity of the Milankovitch cycles in turn allows for the determination of geological time and contribute to the chronostratigraphy (Hinnov 2013). While identifying a number of astronomical cycles can result in relative duration estimates, the process of linking interpreted expressions of Milankovitch cycles directly to astronomical solutions (i.e. astronomical tuning) can result in absolute age estimates.

2.3. Milankovitch cycles

Already in the nineteenth century, the astronomical theory of ice ages – based on ideas of Adhémar – was built upon for the application of astronomical tuning by Croll, Lyell and many others to follow (Berger and Loutre, 1992). Later, in 1941 in his "*Kanon der Erdbestrahlung und seine Auswirkung auf das Eiszeitenproblem*", Milutin Milankovitch attempted to rationalize certain paleoclimatic observations, such as the periodic advance and retreat of glaciers during an ice age, and evaluated the influence of changing astronomical parameters of the Earth on the astronomical forcing (Hilgen et al., 2015). It became apparent that Earth's orbit around the Sun as well as the orientation of Earth's axis gradually change through time.

In this context, three main astronomical parameters that undergo quasi-periodic variations because of gravitational interactions in the Solar System can be distinguished: orbital eccentricity, obliquity and precession (Hinnov 2013). Now often denoted as Milankovitch cycles, the eccentricity, obliquity and precession cycles affect not only the total annual amount of insolation but mainly the distribution thereof on Earth's surface throughout the year (Berger and Loutre, 1992). As the amount of insolation received by the Earth changes, so does the climate system. As illustrated by Fig. 1, complex atmospheric, oceanic, sedimentary and biological systems are influenced by changing astronomical-induced insolation (Strasser et al. 2006).

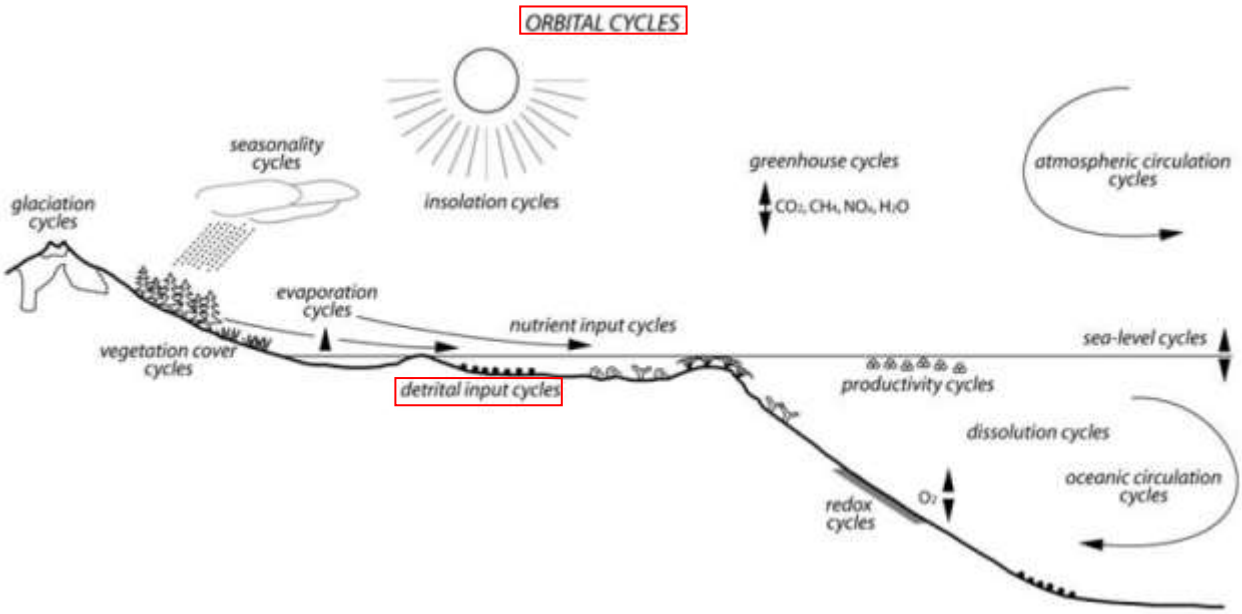

Figure 1: Influence of astronomical cycles on the atmosphere, geosphere, cryosphere, hydrosphere and biosphere (Strasser et al. 2006) Red: cycles of specific interest in this study: detrital input and the orbital cycles.

Along with other important factors such as changing albedo, CO_2 concentrations and changes in the thermohaline circulation, the Milankovitch cycles directly influence Earth's climate system on timescales ranging from 10^4 to 10^6 years (Laskar et al. 2004; Hinnov 2013). Within the context of astronomically forced climate changes, Milankovitch cycles can for example influence the eustatic sea level, depositional patterns and facies (Boggs, 2006). Because sedimentary systems are highly influenced by the eustatic sea level, one or more changing astronomical parameters may be recorded in these systems. Depending on

the sensitivity and whether or not astronomical forcing is translated linearly, proxy records contained within the sedimentary record may have the changing astronomical forcing embedded as a primary signal (Strasser et al. 2006).

2.3.1. Eccentricity

Already in 1890, Croll proposed that, when attempting to understand Earth's past climates, one of the key parameters to consider is the variation in Earth's eccentricity (Laskar et al. 2004). The orbital eccentricity '*e*' refers to the changing elliptically shaped orbit of the Earth around the Sun, caused by gravitational interactions between the major bodies in our Solar System (Pälike, 2005). As illustrated on Fig. 2, changes in the Earth's eccentricity inevitably lead to changes in the Earth-Sun distance and thus also to changes in the total amount of solar radiation reaching our planet over the course of one year. A consequence of the changing elliptical orbit of the Earth is that, due to an increase or decrease in the total insolation at a given latitude, Earth's climate is altered – leading to e.g. changes in the duration of the seasons (Dressing et al., 2010).

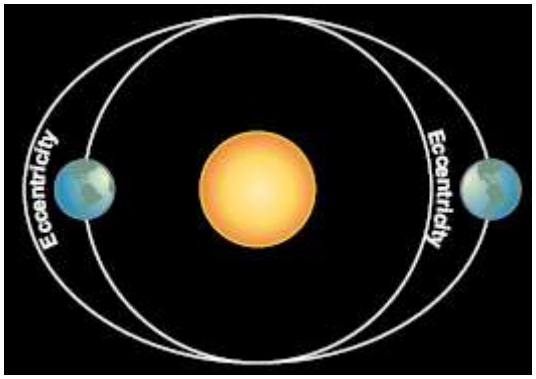

Figure 2: Changing eccentricity of the Earth's motion around the Sun (adopted from http://cimss.ssec.wisc.edu/)

Earth's orbital eccentricity varies quasi-periodically on timescales of 10^4 – 10^6 years. Whereas for circular orbits e = 0 and for parabolic orbits e = 1, the eccentricity of an elliptic orbit lies somewhere between these values. Present mean eccentricity of Earth is estimated to be e = 0.01671 (Pälike, 2005), it has varied from 0.00021 to 0.06696 over the last 40 million years with 3 main periodicities of roughly 100 kyr, 125 kyr and 405 kyr (Laskar et al., 2004).

Based on numerical solutions, for example calculated by Laskar et al. (2004, 2011) for 250 million years into the past and future, the complex modulation of the astronomical parameters is revealed. These amplitude modulations are due to interactions between different frequency components, which are often attributed to the influence of the planets of our Solar System (Pälike, 2005).

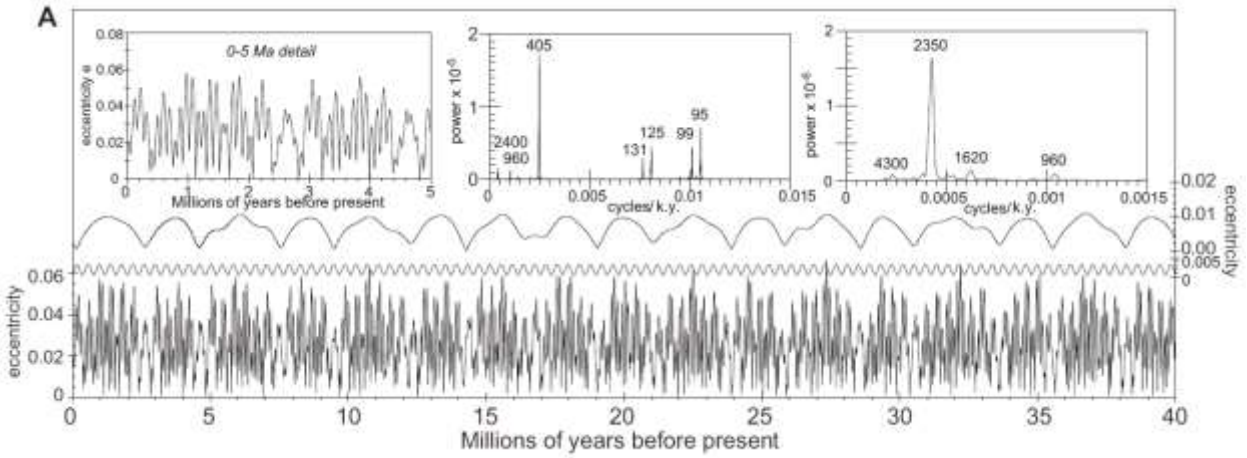

Figure 3: The La2004 nominal solution of the orbital eccentricity for the past 40 million years (Hinnov 2013).

The orbital eccentricity time series according to the nominal La2004 solution can be found on the bottom curve of Fig. 3. The major frequency components is the 405 kyr cycle, which is often denoted as the "405 kyr Metronome" which is, besides phasing discrepancies deeper in time, robust thanks to the large mass of Jupiter which stabilizes this eccentricity cycle over 10^8 years. (Hinnov 2013). This large-amplitude frequency component is mainly caused by gravitational interactions of Venus (lower mass, close approach) and Jupiter (large mass) (Laskar et al., 2004). Additionally, the 100 kyr components are also modulated due to an interaction between the orbital perihelia of Mars and Earth (2.35 Myr, top left on Fig. 3) (Hinnov 2013). Similar amplitude modulations can be observed for all orbital components of the Earth.

2.3.2. Obliquity

The obliquity or axial tilt refers to Earth's rotational axis being tilted relative to the elliptical plane of the Earth's orbit around the Sun (or ecliptic), see Fig. 4 (Hinnov 2013). A direct consequence of the obliquity of the ecliptic is the presence of seasons on Earth. As the Earth rotates around the Sun throughout the year, each hemisphere is oriented differently relative to the Sun, giving rise to seasonal variations. Depending on the angle between the Earth's surface and the incident sunlight, the insolation is distributed differently. Near the equator, the effect of the axial tilt is minor but at higher latitudes however, the influence is more outspoken as the same net amount of solar radiation is distributed over a more different surface area throughout the year. Note that the annual total amount of solar radiation reaching the Earth is not impacted by changes in obliquity, only the distribution thereof is (Pälike, 2005).

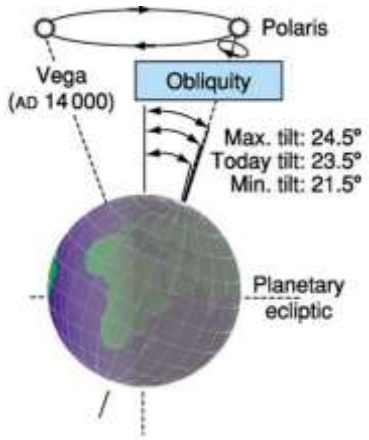

Figure 4: Earth's obliquity and precession of the equinoxes, adopted from (Pälike, 2005).

As the angle of incident solar radiation is directly affected by the obliquity, seasons become more outspoken at higher latitudes with increasing axial tilt. Obliquity however, does not remain constant over time. Variations in axial tilt range from 21.5° to 24.5° with a main frequency of 41 kyr, with the current obliquity being at about 23.5° as seen on Fig. 4. Deeper in time, the main obliquity frequency was shorter (40 kyr), as can be seen on Fig. 5 (top insert), which should be considered when studying e.g. the Cretaceous. In addition to the dominating 41 kyr oscillation of the obliquity, addition variation in amplitude is also observed due to 29 kyr and 54 kyr periods (Pälike, 2005). The La2004 nominal solution of the obliquity as well as the amplitude envelope (change in amplitude over time) is illustrated in Fig. 5 (Hinnov 2013).

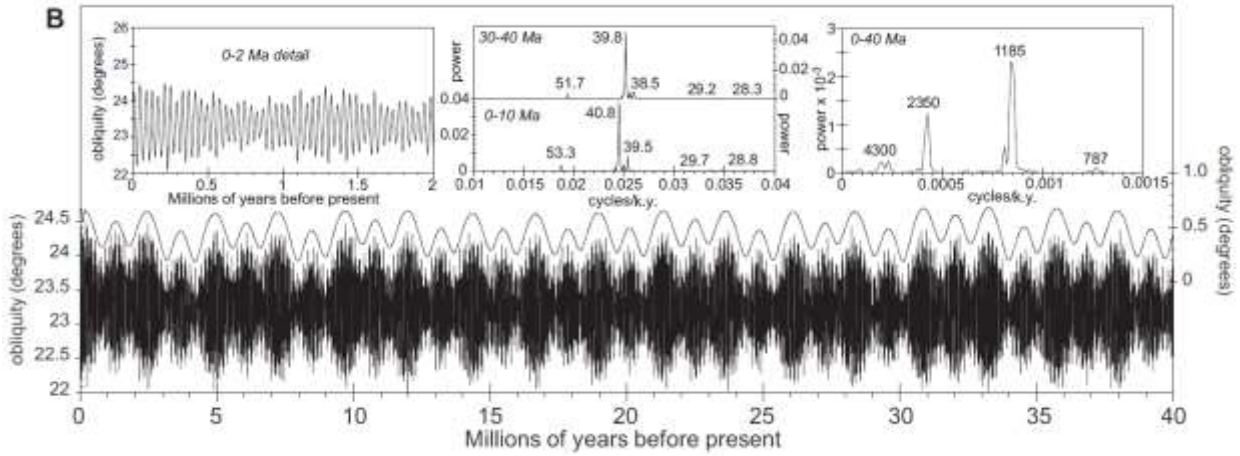

Figure 5: The La2004 nominal solution of the obliquity for the past 40 million years. Bottom: obliquity of the ecliptic, top: amplitude envelope (Hinnov 2013).

In addition to the aforementioned periodicities, a 173 kyr obliquity amplitude modulation, due to interference of secular frequencies related to Earth's and Saturn's precession, has been exploited by Boulila (2018) and co-workers. Aside from the well-known 405 kyr metronome, the obliquity modulation over 1.2 Myr and 173 kyr timescales are alternatives that could also be used for long-term astronomical tuning (Boulila et al., 2018).

2.3.3. Precession

Similar to the motion of a spinning top, Earth wobbles in space due to the gravitational pull of other celestial bodies – a motion called precession of the Earth's rotational axis (Fig. 6). Additional processes such as mass redistribution on Earth (e.g. mantle convection) and the equatorial bulge due to the Earth's rotation also contribute to the precession (Pälike 2005; Hinnov 2013). Similar mechanisms driving quasi-periodic changes in the orbital eccentricity and obliquity also induce cyclical variations in precession through time (Pälike, 2005). Earth's precession frequency components are superimposed, with most dominant periodicities of roughly 19 kyr, 22 kyr and 24 kyr – see Fig. 7, top middle insert.

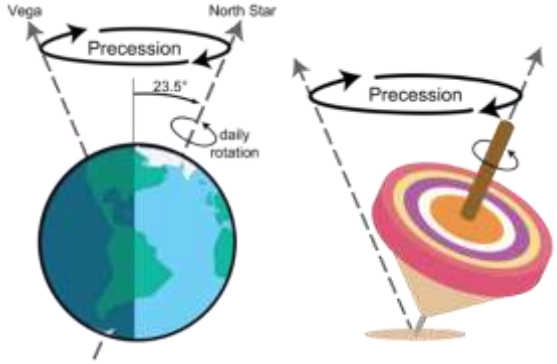

Figure 6: Precession of the Earth, similar to the wobbling of a spinning top, adopted from www.cyclostratigraphy.org (Noir).

The relationship between the timing of the seasons and variations in Earth's astronomical parameters is determined by precession. As the precession changes, the Earth's rotation axis is oriented differently relative to other systems. For example, the current north star is Polaris but in ~14 kyr the axis will point towards Vega as is illustrated on Fig. 6 (Pälike 2005; Hinnov 2013).

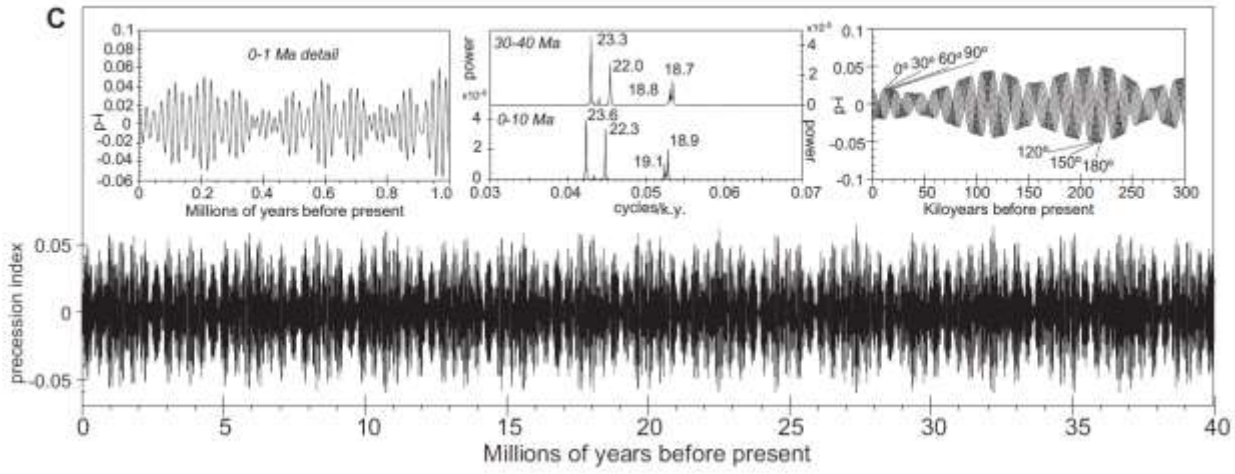

Figure 7: The La2004 nominal solution of the precession for the past 40 million years. Bottom: obliquity of the ecliptic, top: amplitude envelope (Hinnov 2013).

The amplitude of the precession signal is strongly modulated by the orbital eccentricity, meaning the effect of the precession on the insolation is larger for larger eccentricity values *e*. Conversely, at zero eccentricity, the effect of precession is zero as well (Pälike, 2005). This can easily be rationalized by considering the precession index '*e sin* ω_s', but is also illustrated by the bottom plot on Fig. 7. ω_s is a measure for how close the Earth is to the Sun at midsummer; when $\omega_s = 90°$, the Earth is close to the Sun during northern summer – hence leading to a warm summer. When $\omega_s = 270°$ the situation is opposite and summer in the northern hemisphere will be cooler (Marshak, 2008). However, the 19 kyr and 23 kyr insolation periodicities do not translate linearly to the paleoclimate record, something that has to be considered in climate models (Rubincam, 2004).

2.3.4. Divergence of Time-Domain Astronomical Models

Time-domain astronomical models used for calculating numerical solutions of insolation quantities for eccentricity, obliquity and precession are limited by several factors (Laskar et al., 2004; Waltham, 2015). These include uncertainties on initial conditions and chaotic evolution of orbits, that lead to diverging solutions beyond 50 million years – depending on the used astronomical cycle (Laskar et al., 2004). Variations in orbital eccentricity arise from Solar System dynamics only and provide well-constrained numerical solutions for the past 50 million years only, beyond which the stability of the solution for the Earth's eccentricity starts to decrease (Laskar et al., 2004). Due to additional chaos in the Solar System, for example by the unconstrained changes in motion and position of asteroids such as Ceres and Vesta, Earth's eccentricity evolution beyond 60 Myr cannot be determined exactly (Laskar et al., 2011).

However, the most stable elements of the solutions (e.g. 405 kyr eccentricity cycle) can even be extended into the early Mesozoic (250 Myr). Still, one has to consider errors less than 30 to 150 kyr, expressed in absolute time, for a period of 50 to 100 Myr in the past (Laskar et al., 2004), with uncertainty going up to 0.2% at 250 Myr (Meyers and Malinverno, 2018). Fig. 8 below shows differences (expressed in radians) between 6 solutions for the 405 kyr eccentricity cycle (Laskar et al., 2004).

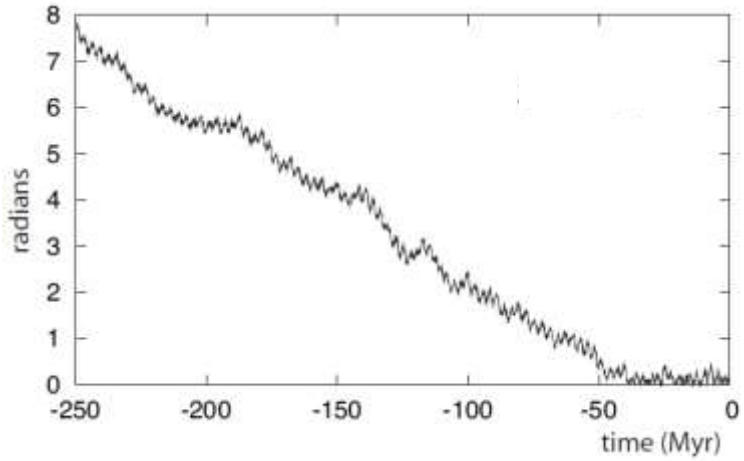

Figure 8: Maximum difference of 6 solutions (Laskar et al., 2004), expressed in radians for 405 kyr term in eccentricity.

Earth's precession and obliquity on the other hand, are – amongst others – also influenced by Earth-Moon dynamics. Because the long-term evolution of the Earth-Moon system is poorly constrained, so are the precession and obliquity solutions beyond 20 million years ago (Laskar et al., 2004; Waltham, 2015). A major source of uncertainty is the tidal dissipation or, in other words dissipation of tidal energy, in the Earth-Moon system. Due to the gravitational pull, the Moon raises a tidal bulge in the fluid and solid Earth. Deceleration of the Earth is a result of the Moon's gravitational forces acting on the tidal bulge, producing a torque directed opposite to Earth's rotation. As a result of tidal dissipation and conservation of total momentum, Earth's rotation speed is decreasing over time leading to an acceleration of the Moon around the Earth and an increase in the Earth-Moon system (Fig. 9). Limited geological data obtained from modulated fossil growth bands suggests the increase of the length of one day on Earth as increased over time inconstantly (Hinnov 2013). Recent work on rudist bivalves confirmed that, as predicted by astronomical models, the length of day has increased since the Late Cretaceous (de Winter et al. 2020).

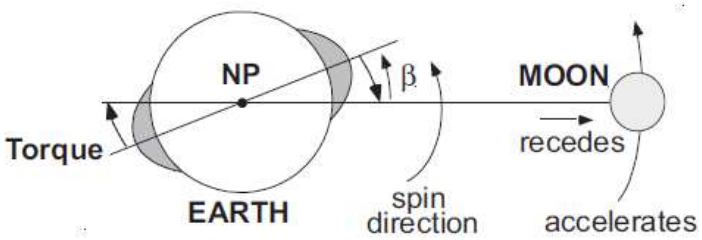

Figure 9: Creation of a torque due to gravitational forces from the Moon acting on tidal bulges leading to deceleration of Earth's rotation rate (Hinnov 2013).

The effect of the evolving Earth-Moon system on the obliquity and precession cycles can be directly observed on the periodograms of the obliquity of the ecliptic and precession index, on Fig. 5 and Fig. 7 respectively. A shift towards higher frequencies for the past 30 to 40 million years ago compared to 0 to 10 million years ago can be seen in both cases. (Laskar et al. 2004; Hinnov 2013). This uncertainty will of course have implications when using either precession or obliquity cycles to calculate sedimentation ranges, especially for records from the Mesozoic and older (66 Myr and beyond) (Laskar et al., 2004; Waltham, 2015). The "Milankovitch calculator" by Waltham (2015) allows for an estimation of the uncertainties (expressed in kyr) on the main obliquity and precession periods (Table 1).

Main Obliquity Period (kyr)	Uncertainty (kyr)
39.55	± 0.90

Precession Periods (kyr)	Uncertainty (kyr)
23.19	± 0.28
21.94	± 0.26
18.78	± 0.24
18.64	± 0.24

Table 1: Obliquity and precession period uncertainties calculated for 70 Ma (Waltham, 2015).

The contribution of many other dissipative effects, including but not limited to atmospheric tides, mantle convection and core-mantle friction have to be taken into account and introduce additional uncertainty to the numerical solutions (Laskar et al., 2004). It is also worth mentioning that climate friction, which is the delayed redistribution of ice/water mass and the isostatic adjustment to the surface loading in response to periodic variations in obliquity, is able to affect Earth's dynamical ellipticity as well (Levrard and Laskar, 2003). Changes in the dynamical ellipticity lead to variations in Earth's precession rate and consequently also influences the obliquity (Hinnov 2013).

2.3.5. Milankovitch Uncertainty and Period-pair Ratios

Based on known periodicities, certain ratios can be expected between various Milankovitch cycles. Knowledge on certain period-pairs can be exploited when trying to link Milankovitch cyclicity to observations made based on a sedimentary dataset (Waltham, 2015). However, as a result of aforementioned uncertainties in the previous chapter – especially deeper in time – careful interpretation of these period-pairs is required. For example, when assessing some typical values for long eccentricity (405 kyr), short eccentricity (100 kyr on average) and precession (e.g. 23 kyr), it can be observed that the ratio between long eccentricity and short eccentricity is nearly equal to the ratio between short eccentricity and precession.

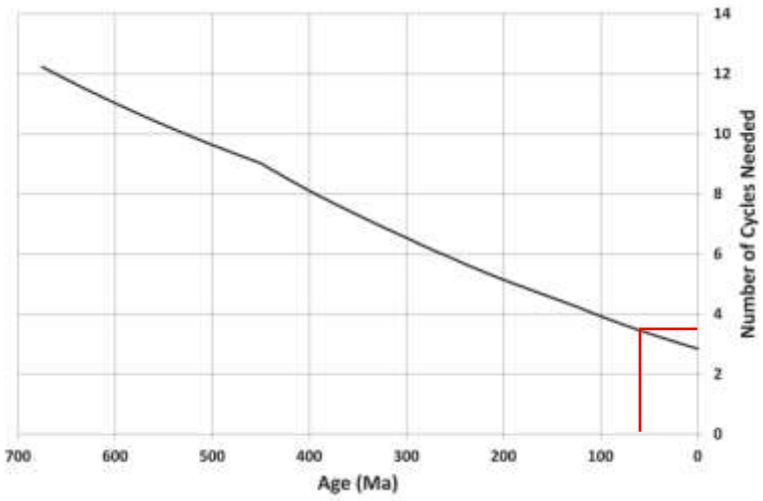

Figure 10: Number of cycles needed for statistically significant attribution to Milankovitch cyclicity (Waltham, 2015). Red lines; estimated amount of cycles needed for the Maastrichtian.

To conclude, in order to address uncertainty originating from all sources when attributing observed cycles to Milankovitch cyclicity, Waltham (2015) suggests that at least 3 observed cycles are required for statistical significance when using the pair-ratio methodology and the subsequent application of cyclostratigraphy for the Maastrichtian (Fig. 10).

2.4. Cyclostratigraphy

Numerous studies exploiting a large variety of proxies and analytical techniques have successfully proven that astronomical cycles, recorded as a primary signal in the stratigraphic record, can be used to improve the temporal framework of the Earth's geology via the application of cyclostratigraphy e.g. (Hays et al. 1976; Hinnov 2013; Sinnesael et al. 2019). Once astronomical signals are identified and thoroughly interpreted, application of astrochronology can be used to contribute to the overall geochronology (Meyers 2019). As defined by Meyers (2019) and based on work of Strasser et al. (2006) and Hinnov (2013), astrochronology is a subdiscipline of cyclostratigraphy and uses the astronomical signal extracted from the geologic record to develop or improve geological timescales. Not only can cyclostratigraphy be used for the dating of sedimentary sequences, but it is also invaluable as a tool for understanding astronomical climate forcing.

Matching cyclical signals originating from proxy records to changing astronomical parameters of the Earth does not immediately provide absolute ages. Initially, only relative time information is provided and depends on the used astronomical cycle(s). If no specific absolute numerical ages can be anchored to the astrochronology that provides relative times for series of stratigraphic records, the correct term to be used is a so-called floating astrochronology (Meyers 2019). Anchoring the relative, floating astrochronological timescales, for example using radio-isotopic dating, results in an anchored astrochronological timeframe (Boggs 2006; Hilgen et al. 2015).

Because not all rhythmical or cyclical patterns in the stratigraphic record were induced by astronomically forced climate change, it is important to confirm the true expression of Milankovitch cycles in the geological record. This is especially true for carbonate rhythmites, where diagenesis can either distort the primary signal or even erase it altogether (da Silva et al., 2012; Swart, 2015). Even more so, rhythmicity can even be introduced were there was none (Westphal et al. 2010; Nohl et al. 2021). Therefore it is important to not only consider carbonate contents when looking at carbonate rhythmites, but to also look at diagenetically inert proxies (such as the Ti/Al ratio) (Westphal et al. 2010). According to Westphal et al. (2010), an integrated stratigraphic approach (for example combining biostratigraphy, magnetostratigraphy and/or chemostratigraphy with cyclostratigraphy) is required to track the origin of the rhythmic signal and to constrain the uncertainties that go with the use cyclostratigraphy.

3. Geological Setting

The Late Cretaceous (100.5 Ma to 66.0 Ma, Gradstein et al., 2020) is represented by widespread chalk deposits in Western Europe as introduced in Chapter 1, including rhythmically distributed flints throughout these deposits, for example also in the succession of the type-Maastrichtian. Named after the Dutch city of Maastricht by Dumont in 1849, the stratigraphy of the Maastrichtian Stage and the corresponding type-Maastrichtian succession has been studied for many years (Jagt and Jagt-Yazykova 2012).

3.1. Maastrichtian Stage – Upper Cretaceous

The Maastrichtian Stage is the uppermost chronostratigraphic unit of the Upper Cretaceous. It represents a time interval spanning from 72.2 to 66.0 Ma. The Maastrichtian is preceded by the Campanian and succeeded by the Danian (marked by red box on Fig. 11). Classification of the different Stages of the chronostratigraphic scale is based on so-called Global Boundary Stratotype Section and Point or GSSP's ("golden spike"), which are internationally agreed upon points in time corresponding to the start of a specific rock succession (Boggs, 2006; Gradstein and Ogg, 2020).

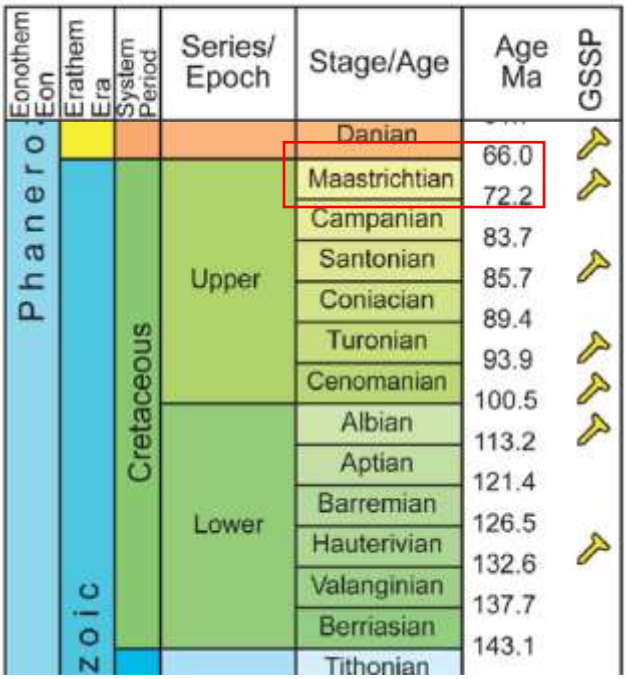

Figure 11: An extract from the Geological Timescale. GSSP (Global Boundary Stratotype Section and Point) define the base age (express in mega annum or Ma) (Gradstein and Ogg, 2020).

The end of the Maastrichtian Age marks the end of the Cretaceous, which is represented by a boundary clay layer characterized by an iridium anomaly and high concentrations of other siderophile elements, caused by the asteroid or comet impact in Yucatan (Mexico), linked to the K-Pg mass extinction (Goderis et al., 2021). Other points of interest are the massive Deccan Traps volcanism that might have contributed to the K-Pg mass extinction (Font et al., 2018) as well as the many mosasaur skeletons that have been excavated in the region around Maastricht (Gallagher et al. 2004). Even though these events are of

interest to the scientific community, much remains unknown of their impact. For example, cooling of the climate during the Campanian and Maastrichtian is not well understood up to date (Voigt and Schönfeld, 2010). Geochemical and cyclostratigraphic studies of chalk deposits have the potential to provide insight in these events, either by revealing changes in the paleoclimate or by providing high-resolution age models useful for dating. For this reason, the Maastrichtian Stage, and by extension the type-Maastrichtian successions, are of importance in worldwide geological research.

3.2. Late Cretaceous Paleoclimate, Paleogeography and Depositional Environment

The Cretaceous was characterized by considerable changes in paleoclimate; even though greenhouse conditions prevailed, the more extreme greenhouse world of the mid-Cretaceous disappeared during the Late Cretaceous (Huber et al. 2002; Voigt and Schönfeld 2010; Engelke et al. 2018). Along with active plate tectonics, seafloor spreading affecting ocean circulation (Engelke et al., 2018; Voigt and Schönfeld, 2010) and volcanism (e.g. Deccan Traps, (Font et al., 2018) were some of the main drivers of global change during the Late Cretaceous. Work carried out by Engelke et al. (2018) has already focused on the late Campanian to early Maastrichtian in the Boreal chalk successions of Northern Europe (Thibault et al., 2016) because of the aforementioned drastic changes in paleoclimate and paleoenvironment.

From a paleogeographic point of view, the Late Cretaceous is of interest due to a major rise in eustatic sea-level, which led to continental flooding. The land corresponding to nowadays North-West Europe was covered by an epeiric sea or Boreal Chalk Sea (Thibault et al., 2016). The region around Maastricht was part of the Late Cretaceous Chalk Sea, situated nearby the Mid-European Island (Engelke et al., 2018) – see white square on Fig. 12. Whereas this region was impacted by a sea transgression during the Campanian, during the Maastrichtian a series of phased regressions occurred (Håkansson et al. 1974; Anderskouv and Surlyk 2011).

Figure 12: Paleogeographic map of the region of interest, region around Maastricht marked by white square and region around Kronsmoor marked by black square (Engelke et al., 2018).

Changes in paleoclimate and paleoenvironment throughout the Campanian and Maastrichtian strongly affected sea water level and hydrodynamic conditions (Wilmsen et al. 2005) as well as weathering and erosion on land (Boggs, 2006). Erosion on land leads to an influx of weathered material, such as clay particles into the epicontinental carbonate factory seas via numerous processes and causes the presence of certain components to be finally included in the chalk (Voigt and Schönfeld, 2010). The presence of quartz minerals and clay in carbonate rocks can be attributed mainly to detrital input, from fluvial or aeolian sources (da Silva et al., 2015). Whenever eustatic sea-levels drop, variations occur in erosion and influx of detrital material (da Silva et al., 2009). For example, sea-level falls that have occurred during the Campanian-Maastrichtian interval (Voigt and Schönfeld, 2010) might have caused an increased influx of detrital (or terrigenous) material into the epicontinental carbonate factory seas (see detrital cycle on Fig. 1). Changes in the source or amount of detrital input can be traced back to changes in mineralogical composition or the amount of certain geochemical elements such as aluminum (Al), titanium (Ti), thorium (Th) and zirconium (Zr), which will be present as contaminations in the carbonate rocks (da Silva et al., 2015). Other elements such as Ca, Mg and Si are also released from source rocks via weathering and finally also partially contribute to the sedimentary carbonate rocks (Boggs, 2006).

According to Engelke et al. (2018), sea level was believed to be at a lower level at the Campanian-Maastrichtian boundary, which would be linked to an increased input of terrigenous material. Similarly, the Campanian-Maastrichtian boundary at the Gulpen Formation is characterized by a hiatus – represented by the Froidmont Horizon (Felder 1983; Felder et al. 2003), which is also indicative for a eustatic sea level fall. A rise in sea level and subsequential high stand occurred throughout the Maastrichtian, leading to an increase in carbonate content of the facies (Engelke et al., 2018; Voigt and Schönfeld, 2010).

3.3. Maastrichtian Geoheritage Project

Characteristic type-Maastrichtian limestones can be found in the area around Maastricht (southern Limburg, the Netherlands and neighboring Belgian and German regions) and served as a valuable resource in the cement-industry (Jagt and Jagt-Yazykova 2012). Because these soft limestones are prone to weathering and rapid overgrowth, and with many quarries already closed or planned to be closed in the coming years, access to this geological archive will become very limited in the near future. In order to record and preserve this geological heritage, the Maastrichtian Geoheritage Project (MGP) has been initiated. This master thesis is a contribution towards the Maastrichtian Geoheritage Project, focusing on the elemental composition of the chalk succession exposed at the Kreco quarry near Hallembaye, Belgium (Vellekoop 2019).

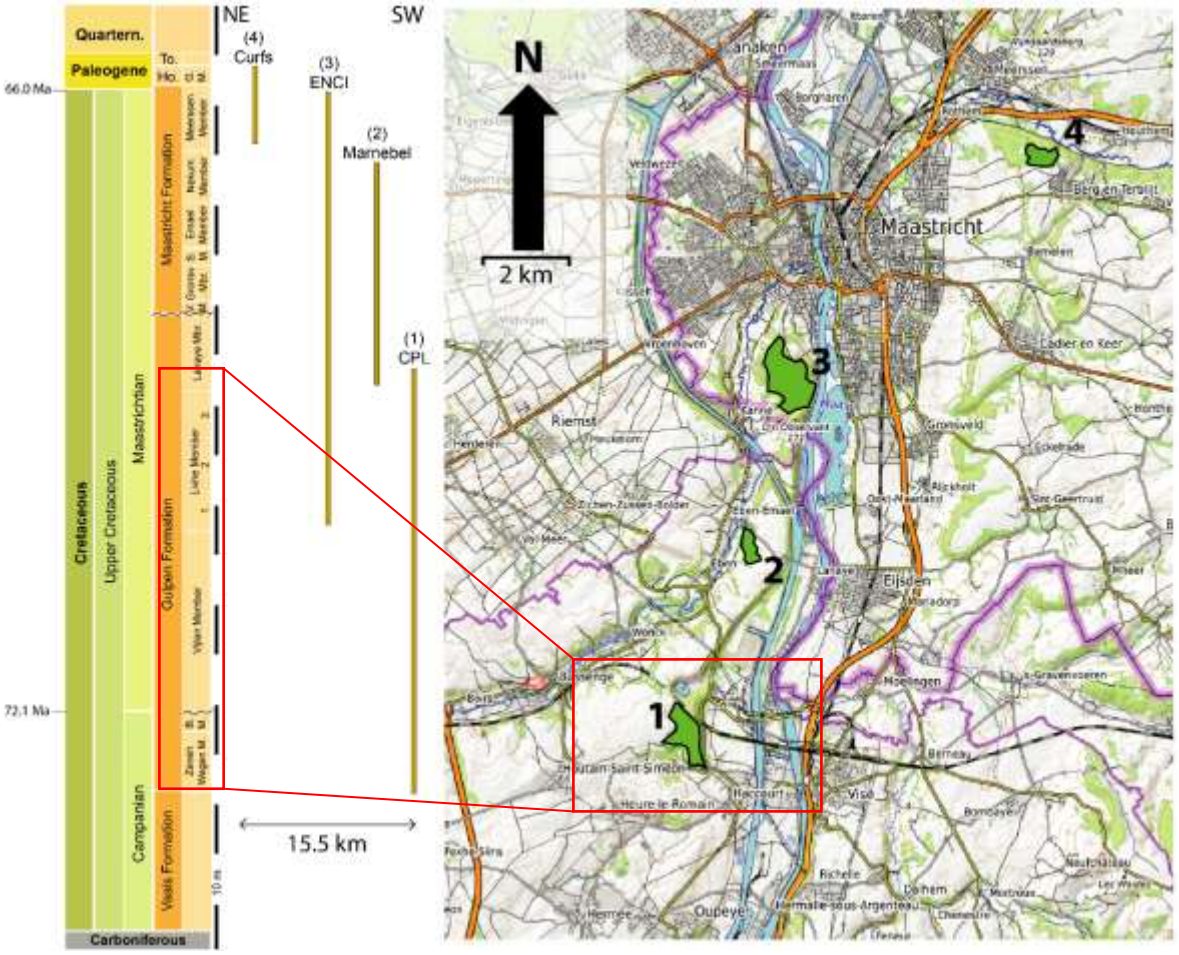

Figure 13: Stratigraphic column and geographic position of the Kreco, Marnebel, ENCI and Curfs quarries in the vicinity of Maastricht. Marked in red: Kreco quarry. Adopted from the MGP description (Vellekoop 2019).

3.4. Kreco quarry – Hallembaye

3.4.1. Setting and Stratigraphy

Formerly known as the “Ciments Portland Liégeois” (CPL) quarry, the Kreco quarry is situated about 10 km south of Maastricht (Keutgen et al. 2010) near the hamlet of Hallembaye, Liège (Belgium), marked in red on Fig. 13. As can be observed from the same figure, the Maastrichtian Stage as well as a part of the Campanian Stage is represented in the 50-meter-high stratigraphy exposed at the Kreco quarry – which is displayed on the picture below (Fig. 14).

Figure 14: Kreco Quarry (picture taken by Dr. Johan Vellekoop).

Almost the entire Gulpen Formation used to be represented in the Kreco quarry, with only Beutenaken Member missing and the Lanaye Member being incomplete. Nowadays the base of the Zeven Wegen Member, the upper part of the Lixhe 3 Member and the entire Lanaye Member are no longer exposed in the quarry (Vellekoop et al., In prep.). A hiatus of about 2.2 Myr is believed to be present in the stratigraphic record (Vellekoop et al., In prep.) between the Zeven Wegen Member (Campanian Stage) and the Vijlen Member (Maastrichtian Stage): the Froidmont Horizon (or Bovenste Bosch), which is the result of a regression phase (Felder 1997). As a result of the 2.2 Myr hiatus that is present at the Kreco quarry, only a small part of the Vijlen Member is represented (part of Vijlen 5 and Vijlen 6 intervals). Subsequently, the Vijlen Member 0 – 4 intervals are missing completely (Fig. 15) (Robaszynski et al. 1985; Felder 1997).

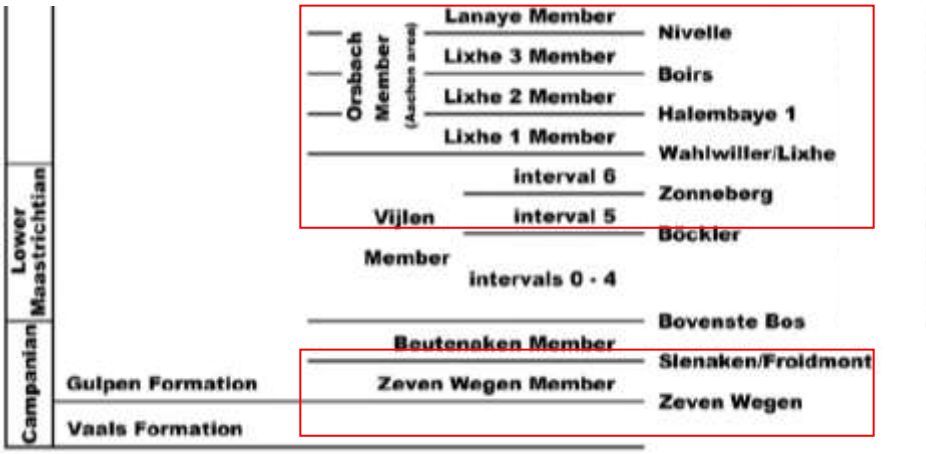

Figure 15: Local stratigraphy (Keutgen 2018). Red: local stratigraphy exposed at the Kreco quarry

The complete stratigraphic interval from 0 m to 49.5 m exposed at the Kreco quarry is treated in this work at a 0.50 m-low sampling resolution. In addition, an interval was selected for analysis at a 0.05 m-high sampling resolution, starting from the Froidmont Horizon (11.75 m), covering the Vijlen Member (part of intervals 5 as well as interval 6) up to the Lixhe 1 Member (34.50 m). This interval was selected for its interesting lithology, which encompasses a transition from greyish chalk with rare flint nodules to more whitish chalk with more regularly occurring flint bands. This study is an expansion on previous high-resolution work (Huygh, 2019) carried out on a limited range (18.50 m – 22.45 m) indicating potential for cyclostratigraphic analysis based on geochemical proxies rather than on biostratigraphy or lithology (Zijlstra 1994; Felder 1996; 1997; Felder et al. 2003; Keutgen 2018).

3.4.2. Lithology

Based on the stratigraphic log of the Kreco quarry near Hallembaye, created during the sample campaign in August 2018, several lithological transitions can be observed. At the bottom of the quarry the Zeven Wegen Member is characterized by monotonous white chalk (0 to 11.75 m) with rare individual black flint nodules (0 to 2 m) and dark gray flint nodules (2 to 5 m). At a stratigraphic height of 7 m, a horizon with individual black/grey flint nodules can be identified. At a stratigraphic height of 11.75 m, the Froidmont Horizon was identified as a prominent hardground.

The Vijlen Member is regionally variable in terms of lithology, with glauconitic chalk on the on hand and more pure, white fine-grained chalk containing small flint nodules on the other (Felder and Bless 1994; Felder 1997). Even though the Vijlen Member has a maximum thickness of about 60 m (Mamelis section), large variations persist in the region around Maastricht (Felder and Bless 1994). According to Felder and Bless (1994), the presence of an erosion channel coincides with changes in both lithofacies as well as bioclast contents of the Vijlen Member. At the base of the Vijlen Member, chalk was altered due to marine regressions, leading to erosion and the subsequent formation of strand plain gulley's (Felder 1997). Upon marine transgression, deposition of Vijlen Member occurred first in the strand plain gulley's, with sediments containing Belemnoidea bioclasts and pebbles. Due to their high concentration of belemnites, these deposits are locally known as a "belemnite graveyard". Later, when less turbulence was believed to be present, a lower energy environment yielded less pebbles and Belemnoidea bioclasts but more Echinodermata bioclasts (Felder 1997). At Hallembaye, the bulk matrix of the Vijlen Member is composed of limestone mainly, with flint and/or cherts occurring throughout the section as nodules or layers. The Vijlen Member is greyish, green-stained and contains some individual grey flint nodules (~12 m to 18 m). From 18 m to 27 m, faint flint bands occur more regularly with an apparent rhythmic pacing throughout the light grey chalk matrix. From 27 m onwards, the chalk has a more whitish color and at a stratigraphic height of appr. 28 m the Lixhe Horizon was recorded based on a 15 – 20 cm-thick layer of black flint nodules, after which black flints occur as nodules or as laminar layers.

Lixhe 1 – 3 Members are characterized by flint nodules and faint to clear flint layers scattered throughout the whitish chalk. At a stratigraphic height of 37.45 m, the Hallembaye Horizon was identified based on a 15 cm-thick flint band, separating Lixhe 1 and Lixhe 2 Members. Bulk chalk matrix of the Lixhe 2 – 3 Members remains white with (often faint) flint bands occurring at, an apparent rhythmic pacing. From 43 m onwards, regular, 5 to 15 cm-thick flint bands can were recorded up to the Boirs Horizon at about 46.75 m. The top of section A was recorded at about 47.05 m and for section B at about 50 m, with correlation between both sections based on the Boirs Horizon.

3.5. Current age model – A small historical review

Fist age models that allowed for a local correlation were based on biostratigraphy (foraminifera by Hofker in 1958 and belemnites by Schmid in 1959), which also allowed to assign the Campanian and Maastrichtian (Felder and Bless 1994). A description of the biostratigraphy of the Campanian-Maastrichtian boundary interval was presented by Robaszynski et al. in 1985, specifically focused on the type-Maastrichtian area as exposed in the Hallembaye Quarry (Robaszynski et al., 1985). Even though the identification of several distinct biozones served its purpose in the determination of relative ages and regional correlation, it remained limited with regards to the exact dating of type-Maastrichtian sections in the region around Maastricht. In order to achieve global correlation as well as to determine absolute ages, a cyclostratigraphic approach holds more potential.

Within the existing framework of biostratigraphy and ongoing research into the lithostratigraphy, it became apparent that the rhythmic pacing of strata could have been the result of astronomical forcing (Zijlstra, 1994). One of the first cyclostratigraphic age models for type-Maastrichtian successions was based on the presence of rhythmically-paced flint bands throughout the chalk by Zijlstra in 1994. Due to cyclic variations in the climate as a result of astronomical forcing, changes in sedimentation rates were believed to be present because of variation in hydrodynamics (named higher “storm intensity” by Zijlstra) and erosion (Zijlstra, 1994). Whenever sedimentation rates were lower, the concentration of authigenic silica would be higher (and eventually lead to flint formation). Alternatively, higher sedimentation rates would imply lower authigenic silica concentrations and thus no flint formation throughout the chalk. Zijlstra used photography, followed by manual black on white drawings, followed by video recording to finally quantify the successive, horizontally distributed silica layers of 5 – 20 cm in the chalk of the Lixhe 1 – 3 Members and Lanaye Member exposed at several locations near Maastricht, including the ENCI quarry (see Fig. 16 below) (Zijlstra, 1994).

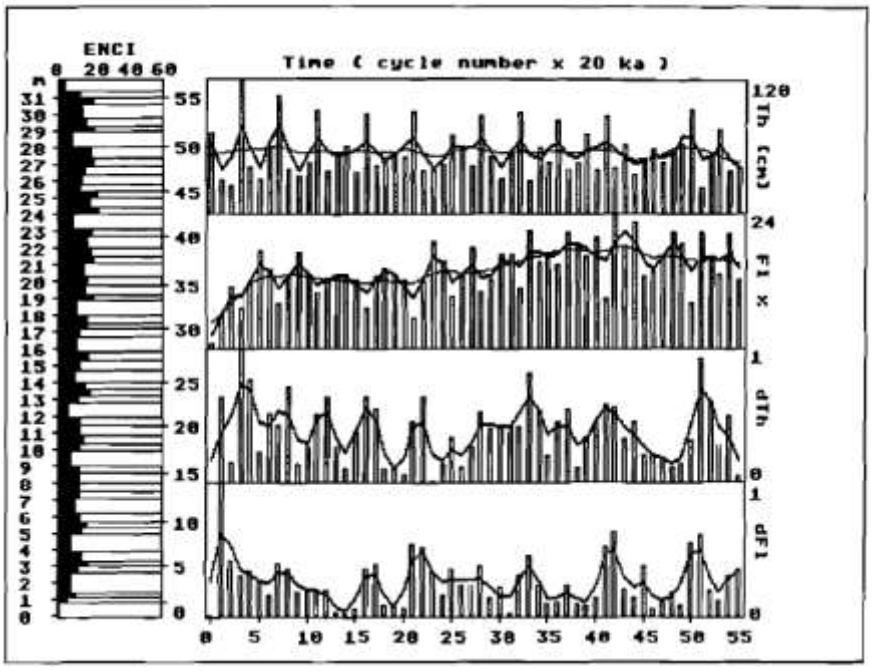

Figure 16: Silica concentrations of the Gulpen Formation (Zijlstra, 1994).

Based on biostratigraphic and lithological insight (including assumed sedimentation rates of cm-dm/kyr) and assuming astronomical forcing of the paleoclimate led to the rhythmically-paced flint cycles, Zijlstra (1994) concluded Milankovitch precession cycles to be registered by the alternations in lithology. The identified 75 cycles (of which 20 were attributed to the Lanaye Member) were then used to construct a preliminary age model by multiplying the cycle number by 20 kyr – presumably Milankovitch precession cyclicity (Zijlstra, 1994). This would mean the age of Lixhe 1 – 3 Members would add up to 1.1 Myr.

Felder (1996) hypothesized that changes in sea level and even Milankovitch cyclicity would be reflected in the bioclast composition. On one hand, the shallow water environment was believed to be affected by changes in storm energy and sea level, which in turn was due to Milankovitch-induced temperature variations. On the other hand, sea level changes and changes in storm energy were believed to affect seafloor ecosystems and thus favoring either bivalves or echinoderm – affecting bioclast composition (Keutgen 2018). These variations in bioclast composition were then compared to Milankovitch-paced interpreted flint cycles by linking lithostratigraphic positions to certain biozones (Felder 1996; Keutgen 2018). In 1994, Felder estimated early Maastrichtian sedimentation rates to be 1.33 to 2.4 cm/kyr based on lithostratigraphic units that were calibrated against biozones (e.g. of foraminifera). In this case, the Mamelis locality which has the greatest sediment thickness (60 m) for a maximum duration of 4.5 Myr to a minimum duration of 2.5 Myr respectively was used. However, Felder recognized that given the differences in sediment thickness observed at different localities, real sedimentation rates could have differed as well (Felder 1996). Three years later, Vijlen Member chalk, collected from several boreholes and outcrops from the Meuse-Rhine Euregio, were analyzed for bioclast content (Felder 1997), using mainly benthic foraminifera to correlate the sections and to subdivide the Vijlen Member. At the time of publication by Felder in 1997, most work focused on fossil content and biostratigraphy.

One of the first studies that used a 5 cm-high sampling resolution for the application of stratigraphy was carried out by Felder et al. in 2003. Two neighboring quarries (3 m section at CBR-Lixhe and 2.6 m section at ENCI) were sampled below the Nivelle Horizon (upper Gulpen Formation, Lixhe Members)(Felder et al. 2003). Both quarries were analyzed not only for dinocyst, pollen grains and bioclast contents but also for carbon and oxygen isotopic composition (Felder et al. 2003). Given that the CBR-Lixhe quarry and the Kreco quarry are back to back, low regional variability between the exposed strata can be expected. In their work, Felder et al. attempted to link biostratigraphy and the isotopic measurements to Milankovitch precession cycles assuming a sedimentation rate of 5 cm/kyr based on work by Felder published in 1996. Also, it was hypothesized that flint beds, used for correlation of both sections, are not necessarily linked to primary deposition due to their diagenetic origin (Felder et al. 2003).This implies that a potential primary signal recorded during deposition might have been distorted by the diagenetic processes that led to the flint bed formation. Moreover, more recent work on carbon and oxygen isotopes (Huygh, 2019) carried out on a part of the Vijlen Member of the nearby Kreco quarry also revealed potential diagenetic overprint of the oxygen isotope signal, questioning the reliability of the results by Felder et al., 2003.

Keutgen suggested in 2018 that the changes in bioclast content, as reported by Felder in the past, could be related to Milankovitch cyclicity. The entire sedimentary succession of the type-Maastrichtian was studied based on Felder's approach of using bioclasts, but with addition of index fossils such as dinoflagellate cysts and calcareous nannofossils. Comparison between established 20 kyr precession cycles as calibrated via Milankovitch-paced flint cycles by Zijlstra (1994) with Felder's bioclast cycles leads to the conclusion the latter might be interpreted as either short or long eccentricity cycles (Keutgen 2018). Based on work by Zijlstra (1994) and Schioler et al. (1997), Keutgen reported in 2018 that the upper Maastrichtian succession from Lixhe 1 Member up to the Berg en Terblijt Horizon, in the type-Maastrichtian encompass about 2.2 Myr.

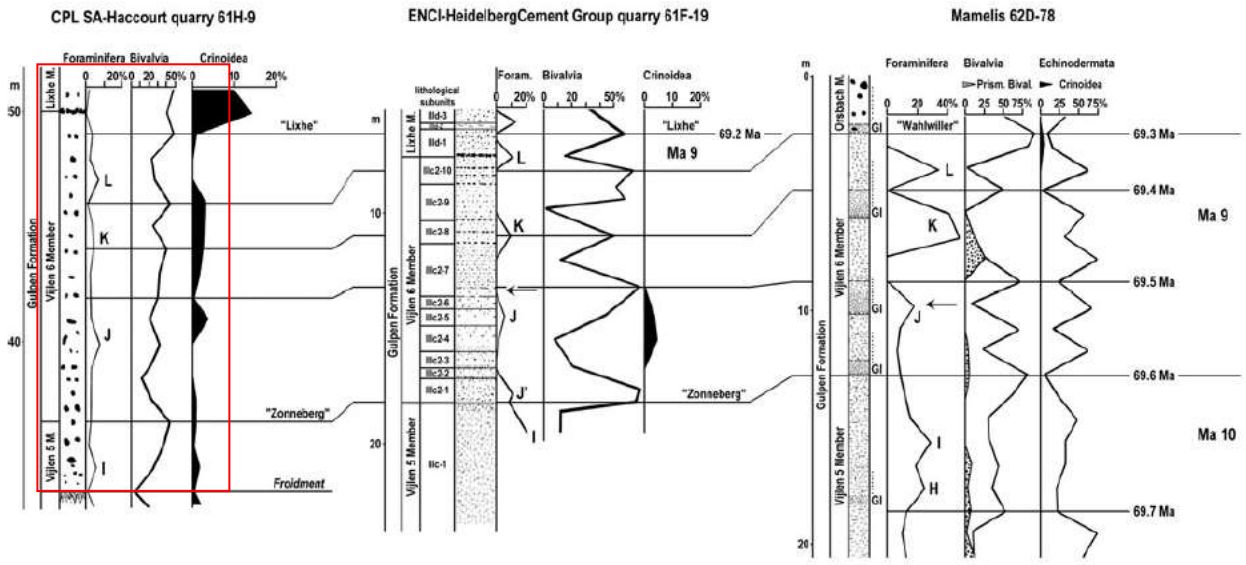

Figure 17: Lithology and bioclast composition of the Vjilen Member for the Kreco-quarry near Hallembaye, with Ma 10 and Ma 9 corresponding to 405 kyr long eccentricity cycles that are based on bivalve maxima (Keutgen 2018).Red: interval of interest in this study.

As illustrated on Fig. 17, 400 kyr eccentricity cycles (Ma 9, Ma 10) were designated based on observed maxima in bivalve content, which were also used to attempt correlating the Kreco (formerly CPL SA-Haccourt), ENCI quarries as well as the section near Mamelis. The base of the Vijlen 0 Member is established at 70.2 Ma, however given the presence of a hiatus (Froidmont Horizon) at the Kreco quarry, no clear dating for Vijlen 0 to 5 Members is provided. The Zonneberg Horizon, marking the transition from the Vijlen 5 to 6 Member is dated to 69.6 Ma. Based on these interpretations and correlations with other quarries of the type-Maastrichtian, the Vijlen Member at Kreco should not encompass more than 800 kyr over a stratigraphic interval of roughly 16 m (corresponding roughly to an average sedimentation rate of 2 cm/kyr). This also means that the entire Vijlen Member, taking into account other quarries and boreholes in the type-Maastrichtian, should span no more than 1.4 Myr (Keutgen 2018).

The Lixhe Horizon (top of the Vijlen Member) can be dated back to 69.2 Ma, based on dating of index species (Keutgen 2018), which is interpreted to correspond to the base of a long eccentricity cycle. The top of the section exposed at the Kreco quarry can be dated to 68.0 Ma roughly, formerly consisting of the Lixhe 1 – 3 and (part of) the Lanaye Members. This stratigraphic interval of about 22 m would correspond to 1.2 Myr (also corresponding to an average sedimentation rate of almost 2 cm/kyr). Based on Zijlstra's work (1994), Keutgen (2018) confirms the 55 cycles of 20 kyr for the Lixhe 1 – 3 Members via comparison with bioclasts zones. Based on lithology, bivalves and crinoida, the Lixhe 1 Member should not last longer than one 405 kyr long eccentricity cycle (Keutgen 2018). Vijlen and Lixhe 1 Member exposed at the Hallembaye quarry should not encompass more than 1.2 Myr, with average sedimentation rates of 2 cm/kyr and 2.5 cm/kyr – based on Keutgen (2018).

Up to date, a cyclostratigraphic approach based on high-resolution geochemical datasets has not yet been applied on the type-Maastrichtian chalk from the Kreco quarry near Hallembaye. A conceptually similar study however has already been carried out by Engelke et al. (2018) on the upper Campanian to lower Maastrichtian chalk at Kronsmoor, Germany. Presence of 40 kyr obliquity and 405 long-eccentricity cycles was demonstrated in the boreal chalk successions of northwestern Europe, recorded in $CaCO_3$-content (Engelke et al., 2018). Given the close proximity and similarity in setting, the study by Engelke et al. (2018) serves as an ideal proof of concept for using elemental proxies for the application of cyclostratigraphy.

Most recent work on type-Maastrichtian strata uses a chemostratigraphic approach based on carbon isotope geochemistry calibrated with biostratigraphic events, allows for a global correlation of these strata and was able to date the base of the Vijlen Member at Hallembaye at 70.4 Ma (Vellekoop et al., In prep.) – see Chapter 7.4.

The main focus of this master thesis is to attempt to construct an updated astrochronological time model that does not depend on bioclasts or on flint layers (which might not be of primary nor astronomical origin) but rather on the elemental composition of the chalk. Combined with the updated chemostratigraphy by Vellekoop et al. (in prep.), the newly developed astrochronological age model based on a cyclostratigraphy will enable application of an integrated stratigraphic approach in the future and will allow for correlation with other well-constrained Maastrichtian deposits, such as Gubbio, Italy (Voigt et al. 2012; Sinnesael et al. 2016; Sinnesael et al. 2019) and the Stevns-1 core, Denmark (Thibault et al. 2012; Voigt et al. 2012; Vellekoop et al. In prep.)

4. Methodology

4.1. Sampling and Sample Preparation

Sampling of the chalk at the Kreco quarry near Hallembaye has been carried out by members of the Maastrichtian Geoheritage Project in 2018. Taking into account the possible application of cyclostratigraphy, sampling was carried out at a high resolution (i.e., every 5 cm) along the exposed 50 m-thick stratigraphic column. Along with some flints and fossils in some cases, the chalk rock samples were stored in labeled plastic bags.

As the point of interest in this study is the geochemical composition of the chalk, all other types of material or contaminants that are present had to be removed. This way, perturbations during measurements as well as incorrect interpretation of the data, can be avoided. Therefore, the chalk samples were first dried in an oven at 50°C for about two weeks. After subsampling, a cleaning step of the chalk rocks was carried out – by hand or using a scalpel – to remove all potential contaminants such as moss, flint and/or traces of rust.

Figure 18: Sample preparation set-up; chalk samples were powdered using the pestle and mortar and transferred to tightly closed plastic containers.

Once cleaned of all observable contaminants, the subset of chalk samples was powdered using a pestle and mortar and stored in closed plastic containers to avoid contamination. Special attention was paid to avoiding cross-contamination by thoroughly cleaning the pestle and mortar using deionized water and drying. In total 510 samples were dried, subsampled, cleaned, powdered and stored for later analyses.

4.2. Micro X-ray Fluorescence

Ever since their discovery in November 1895 by Wilhelm Conrad Röntgen, “unknown radiation” or “X-rays” have been used in numerous applications ranging from medical X-ray imaging to X-ray spectroscopy (Vincze, 2021). In 1914, Henry Moseley published his findings on characteristic X-ray emission of chemical elements. Now known as Moseley’s law, he discovered that a linear correlation exists between the square root of the emission frequency and the atomic number Z. The discovery of X-rays and Moseley’s law lie at the basis of X-ray Fluorescence (XRF) spectroscopy (Vincze 2021; Uo et al. 2015).

4.2.1. Principles of XRF Spectroscopy

X-rays used in XRF spectroscopy are a type of electromagnetic radiation with short wavelengths (typically ranging from 0.1 to 100 Ångström or 0.1 to 100 keV). Irradiation of matter with X-rays leads to an excitation of the atom as a result of the generation of core electron vacancies. Whenever the incident X-ray energy is higher than the core electron binding energy (or absorption edge), the X-ray photon is able to eject a bound electron by the photoelectric effect. The ejected core electron, often denoted as a photoelectron, is removed from the atom – a phenomenon exploited by X-ray photoelectron spectroscopy (Fig. 19).

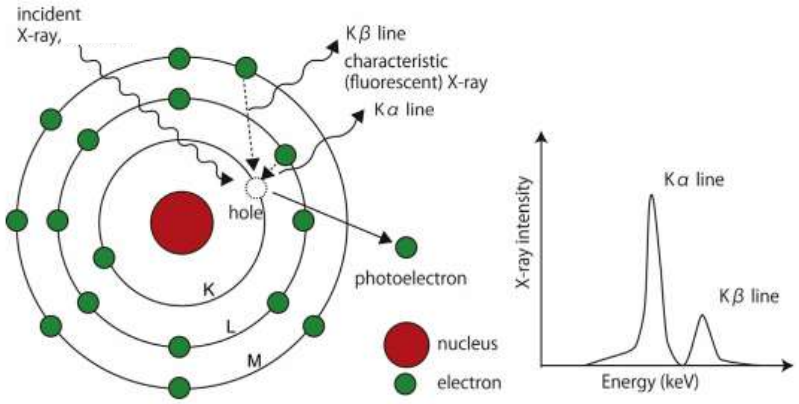

Figure 19: XRF fundamentals (Uo et al. 2015).

Due to the presence of a vacancy, the atom is now in an unstable, excited state which will result in relaxation of the atom via inner-shell electron transitions, via a cascade-type mechanism (=fluorescence). For example, when a K-shell electron is ejected, subsequent relaxation may occur via an inner-shell electron transition from the L-shell to the K-shell. Consequently, a vacancy is created in the L-shell, which will in turn cause further relaxation for example via an inner-shell electron transition from the M-shell. Relaxation leads to the emission of either characteristic electromagnetic radiation or to the emission of an Auger electron (the latter being exploited in Auger Electron Spectroscopy) (Vincze, 2021).

According to the Siegbahn notation, an inner-shell electron transition from the L to the K-shell, giving rise to the emission of characteristic X-rays, is called a K_{α}-transition. Based on known energies of each electronic level for each element, characteristic K, L, … lines can be attributed to specific elements. As a

results of the energy differences between each shell, K-lines have a higher energy compared to L-lines and so on. Hence, the presence of certain elements in a sample can be confirmed and quantified via the detection of their characteristic X-ray intensities at a given energies. XRF spectroscopy is therefore not only a qualitative technique but can also be used for the quantification of the elemental composition of the sample (Vincze, 2021).

Due to the cascade of inner-shell electron transitions, multiple characteristic X-ray lines can be emitted by one excited atom. Also, for light elements (e.g. Si, Ca), K-lines are used for detection and quantification. Heavier elements (such as Pb) however can't be excited via the K-shell because the X-ray source energy is far below the K-absorption edge of those elements. Thus, heavier elements are measured via their characteristic L-lines instead. Depending on the resolution of the detector, this may lead to overlapping characteristic X-ray lines from different elements on the energy/wavelength spectrum and can render the spectrum rather complex. Also, due to their penetrative nature, X-rays not only irradiate the sample surface, but are also able to excite sub-surface atoms. The competition between characteristic X-ray emission and Auger electron emission (with the latter being dominant for lighter elements) leads to an element-specific fluorescent yield. Along with other phenomena, such as a decreased excitation efficiency, lighter elements are often detected with a lower sensitivity. As a consequence, benchtop XRF equipment generally does not measure elements lighter than sodium. Lastly, secondary excitation should also be taken into account when quantifying XRF spectra (Vincze, 2021). When attempting to quantify XRF spectra, deconvolution is often required as is calibration based on standards with a known composition (often via an iterative procedure) to overcome many of the aforementioned phenomena complicating straightforward quantification (Rousseau, 2004).

4.2.2. Micro X-ray Fluorescence

Bench-top micro X-ray fluorescence (µXRF) lab equipment, such as the Bruker Tornado M4, are able to focus the generated X-rays on micro-sized sample surfaces (Bruker, 2015). It allows for a cost-efficient, rapid and straightforward determination of the chemical composition of a sample via non-destructive elemental analysis. This way, the elemental composition of carbonates (chalk) can be determined which is, as already touched upon in Chapter 2.1., key for using chemical elements such as Ca, Ti, Al, etc. as proxies for paleoclimatic and paleoenvironmental changes (de Winter et al., 2017).

4.2.3. Experimental Set-up and Parameters

Tunable micrometer-sized X-ray beams are generated by the 30 W Rhodium anode metal-ceramic X-ray source at 50 kV / 600 µA (Bruker, 2015). Two silicon drift detectors (30 mm^2) are installed and have a resolution of 145 eV (Mn-K_α) at 300 kilocounts per second (Kaskes et al., 2021). Using polycapillary optics, tube X-ray radiation with an initially large solid angle can be focused on spots of 25 µm or 200 µm. Using a custom-made polymer sample holder, a total of 54 powder samples can be placed at once in the vacuum chamber of the Bruker Tornado M4, at near-vacuum conditions of about 20 mbar (de Winter et al., 2017;

Kaskes et al., 2021). Subsampling of the powdered samples was carried out by carefully transferring some powder into small, cylindrical plastic cups (diameter of 1.5 cm, height of 0.7 cm appr.), ensuring the sample surface to be smooth as possible to avoid influence on the measurements (Kaskes et al., 2021). These cups were then stored in the custom-made polymer sample holder, which was then placed in the vacuum chamber of the Tornado M4 (Fig. 20).

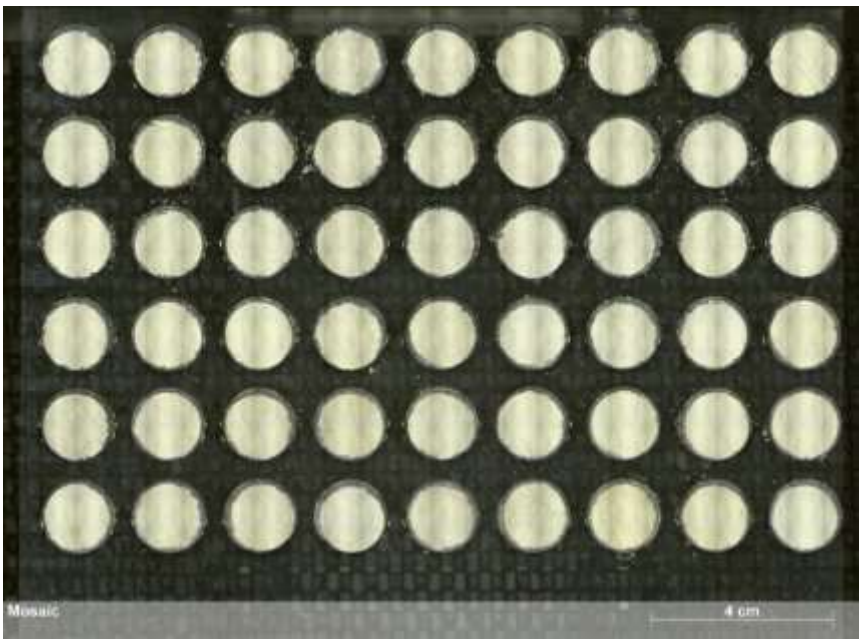

Figure 20: Tornado M4 Mosaic picture of Batch 2, containing 54 powdered chalk samples.

Using 2 optical video microscopes, showing approximately 1 mm² and 10 mm², sample surface imaging is carried out at 100x and 10x respectively. This way, manual selection of x,y,z-coordinates for spot measurement can be carried out effectively based on visual observation of the sample surface, avoiding discrepancies in results due to sample surface inconsistencies. Autofocusing allows for setting the sample height (z-coordinate) correctly. To allow for statistics to be carried out and to get a better approximation of the actual average sample content, 10 point measurements are carried out per sample (de Winter et al., 2017) as indicated on Fig. 21 below. In total, an automated sequence of 540 spot measurements can be carried out when configured this way.

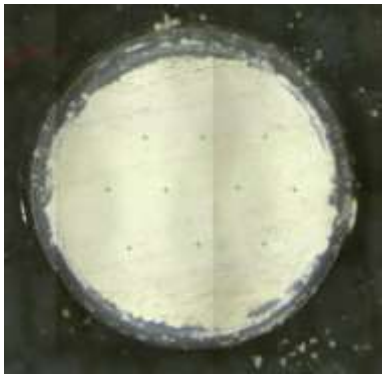

Figure 21: 10 points selected (x,y coordinates) for µXRF measurement

Irradiation of the sample with an integration time of 120 seconds (live time) and energy dispersive detection allows for a simultaneous measurement of all detectable elements. Characteristic fluorescent X-rays are detected using 2 silicon drift detectors. Incoming X-rays induce varying ionization in the detector proportional to their energy, which in turn produces a varying charge. X-ray intensity is accordingly expressed as counts per second per electron volt (cps/eV) (Bruker, 2015).

4.2.4. Data Treatment

4.2.4.1. Spectrum Assignment and Pre-quantification

Typically, detected characteristic X-ray intensities are expressed as normalized counts per second (cps/eV) in function of the energy in keV, as indicated on Fig. 22 (see appendix 11.2 for an example of a completely assigned spectrum using the Bruker Esprit software package). Due to the elastic or coherent (conservation of kinetic energy) and inelastic or incoherent scattering, Rayleigh and Compton peaks respectively are visible on the spectrum as well. Also, the emitted X-ray radiation has a polychromatic component, caused by decelerating radiation causing the so-called "bremsstrahlung", and a superimposed discrete set of characteristic X-ray lines corresponding to the source metal. Together, the polychromatic and discrete components give rise to the characteristic background spectrum for that specific source at those specific parameters. Recording this background spectrum (in absence of any sample) allows to correct the experimental spectra.

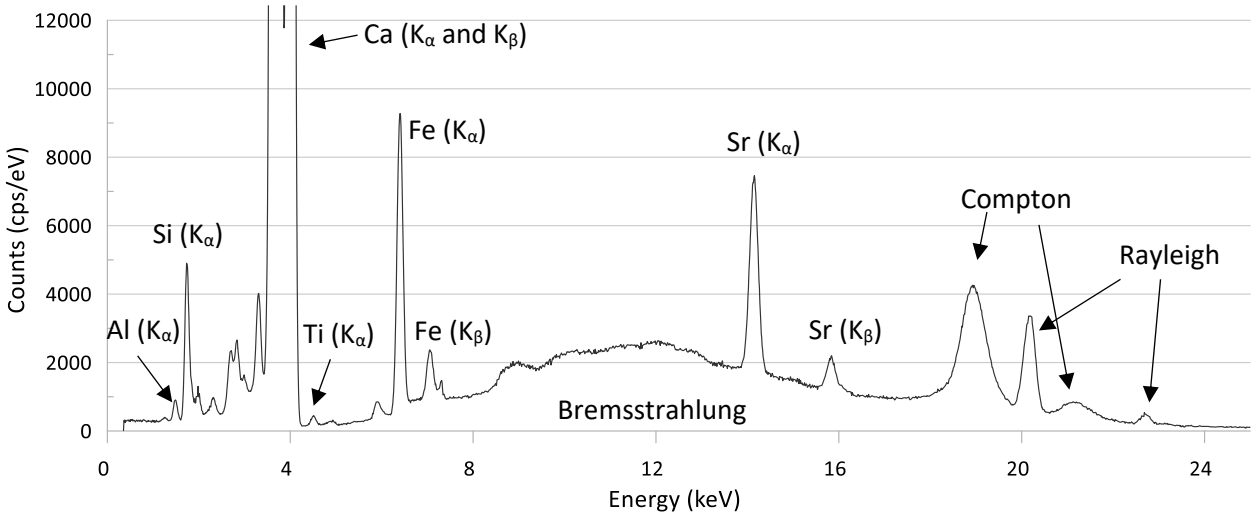

Figure 22: Experimental XRF spectrum of sample HAL18_A_30.85a, with assigned key elements Si, Ca, Fe, Sr and Zr by their K_α-lines as well as Compton and Rayleigh scatter peaks and the bremsstrahlung continuum.

As a first step of the quantification process, all peaks are to be identified and assigned to their respective elements – something which is simplified using the Bruker Esprit software. Visual inspection is required afterwards nonetheless. Translation of the measured intensities emitted by the sample to the composition thereof is described by the Sherman equation. This equation allows to calculate theoretical net, element-specific X-ray intensities from a standard with known composition. Using an iterative procedure, theoretical X-ray intensities are calculated using the Sherman equation and compared with the experimental spectrum until both theoretical and experimental spectra are in agreement (Rousseau,

2004). As described by de Winter et al. (2017), in order to account for matrix-effects, XRF measurements should always be calibrated based on matrix-matched reference material(s). Using a method which is based on repeated spot analysis of the CRM393 limestone standard, the raw spectral data can be transformed to normalized elemental mass concentration (expressed in weight per cent or wt%) values per element (de Winter et al., 2017; Rousseau, 2004). Even more so, assuming a carbonate matrix, oxygen and carbon mass fractions are also calculated based on the Ca signal. This is of added value because in practice, both oxygen and carbon are too light to be measured by XRF.

4.2.4.2. Calibration

Because calculations of element mass fractions were carried out using an iterative procedure that was based on CRM393 only, an additional calibration step is included to further correct the raw data. Calibration of the pre-quantified data is carried out based on the calibration slope values derived from following standard materials: GBW07108, GBW07714, GBW07717, CCH1, CRM513, CRM393, COQ1, SRM1d, CRM512 and ECRM782. Spectra measured for the construction of the calibration slopes was measured using similar experimental conditions (25 µm beam size, 120 seconds real time) to the ones used for measurement of the samples (Table 2). With exception of Na, S, Cl, Rb and Rh, all elements detected in the chalk samples are calibrated prior to further data treatment and outlier determination. It should be mentioned that Vanadium was not included in the most recent update of the µXRF calibration slopes for limestones, therefore a less recent slope value of 0.23 ($R^2 = 1$) was used.

Element	Slope	R^2
C	1.02E+00	0.9947
O	9.97E-01	1.0000
Mg	1.16E+00	0.9964
Al	2.89E+00	0.9977
Si	4.15E-01	0.9976
P	8.40E+01	0.9293
K	9.78E-01	0.9972
Ca	1.01E+00	0.9989
Ti	8.80E-02	0.9986
Cr	1.34E+00	0.9930
Mn	1.51E+00	0.9884
Fe	8.55E-01	0.9962
Ni	1.61E+00	0.9910
Cu	2.10E+00	0.9881
Zn	9.44E-01	0.9945
Sr	1.04E+00	0.9999
Y	1.45E+00	0.9936
Zr	1.87E+00	0.9922
Ba	7.16E-01	0.9953
Pb	4.00E-01	0.9849

Table 2: January 2021 µXRF calibration slope values for 25 µm beam size recorded at 120 s real time, by Pim Kaskes.

4.2.4.3. Outlier Determination and Removal

As mentioned in Chapter 4.2.3., for each sample 10 spot measurements were carried out using a focused 25 µm x-ray beam. If the focused x-ray spot of one (or more) measurements is located near a specific microscopic mineral inclusion, elemental composition values might strongly deviate from the bulk sample matrix. Consequently, upon averaging of the 10 spot measurement datapoints, a strong bias can be introduced if these outliers are not removed. Since spot measurements of certain mineral inclusion do still represent a part of the sample's composition however, robust statistics are needed to identify and remove these outliers to avoid inducing artificial trends or spikes in the final dataset. The term "outlier" in this case is to be interpreted as any value not significantly representing the bulk sample composition based on its position in the median series.

Commonly used statistics using the arithmetic mean as the central tendency indicator assume a normal distribution of data. Additionally, the arithmetic mean and the standard deviation are inherently influenced by the presence of outliers and can be considered to be less robust (Leys et al., 2013). As proposed by Leys *et al.* (2013), using the absolute deviation around the median proves to be more robust for the detection of outliers compared to using the standard deviation around the mean – especially considering the considerable skewness of the data distribution due to the presence of outliers. Using the standard deviation around the mean allows for a selection of the most representative spot measurement datapoints for each sample, neglecting extreme values (Leys et al., 2013).

Using the median, which is less sensitive to the presence of outliers, as the measure of central tendency, the robust scale estimator Median Absolute Deviation (*MAD*) can be calculated (Leys et al., 2013; Rousseeuw and Croux, 1993) (4):

$$MAD = b\, M_i\left(\left|x_i - M_j(x_j)\right|\right) \tag{4}$$

When neglecting the presence of outliers, the distribution of the data is expected to be normal as one would expect when measuring bulk sample composition. Hence, the constant *b* is set to a value of 1.4826 for a correct estimation of the scale (Rousseeuw and Croux, 1993). In a first step, the median of the original 10 spot measurement datapoints $M_j(x_j)$ is subtracted from each observable x_i. In a second step, the absolute values are computed for this new series of 10 datapoints. Finally, the median M_i of this new series is calculated and multiplied by constant *b*, yielding the *MAD*.

To identify outliers, a poorly conservative rejection criterion was determined using an acceptance threshold constant (*ATC*) of 2, according to (5):

$$M_j(x_j) - ATC * MAD < x_i < M_j(x_j) + ATC * MAD \tag{5}$$

The reason for selecting the poorly conservative *ATC* value of 2 compared to the generally advised value of 2.5 is that outlier presence must be minimized as strictly as possible in this dataset with regards to subsequent data analysis. Based on the rejection criterion, any spot measurement data point value x_i not satisfying equation (5) is flagged and removed from the dataset. After outlier identification and removal, the remaining datapoints for each element from the spot measurements are averaged (arithmetic mean) and the standard deviation is determined.

4.2.5. µXRF Methodology Assessment

4.2.5.1. Beam Size

Forty-nine samples were measured twice using identical experimental parameters, including the same (x,y,z) coordinates for spot analysis but with changed beam sizes; 25 µm and 200 µm – the latter being the so-called defocused X-ray beam. As illustrated by Fig. 23, considerable differences can be observed between the 25 µm dataset and the 200 µm dataset. Also, whereas trace element V was not detected using the defocused beam, trace element Ni remained undetected using the 25 µm beam.

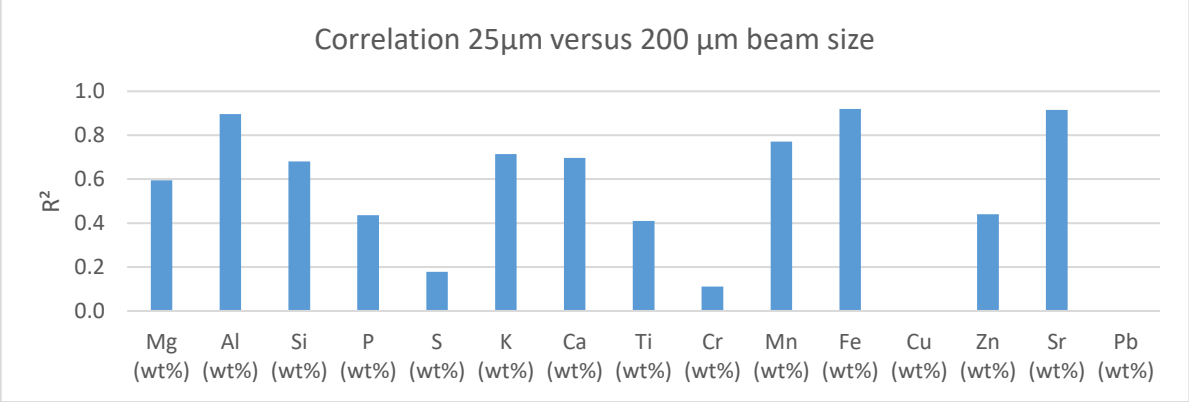

Figure 23: R^2 values between geochemical elements conc. (wt%) measured using X-ray beam size of 25 µm and 200 µm.

Large differences in R^2 values can be observed; elements such as Al, Si, K, Ca, Mn, Fe and Sr are measured quite robust and have R^2 values above 0.6; elements such as S, Cr, Cu and Pb on the other hand show very poor (to no) correlation with R^2 values well below 0.2.

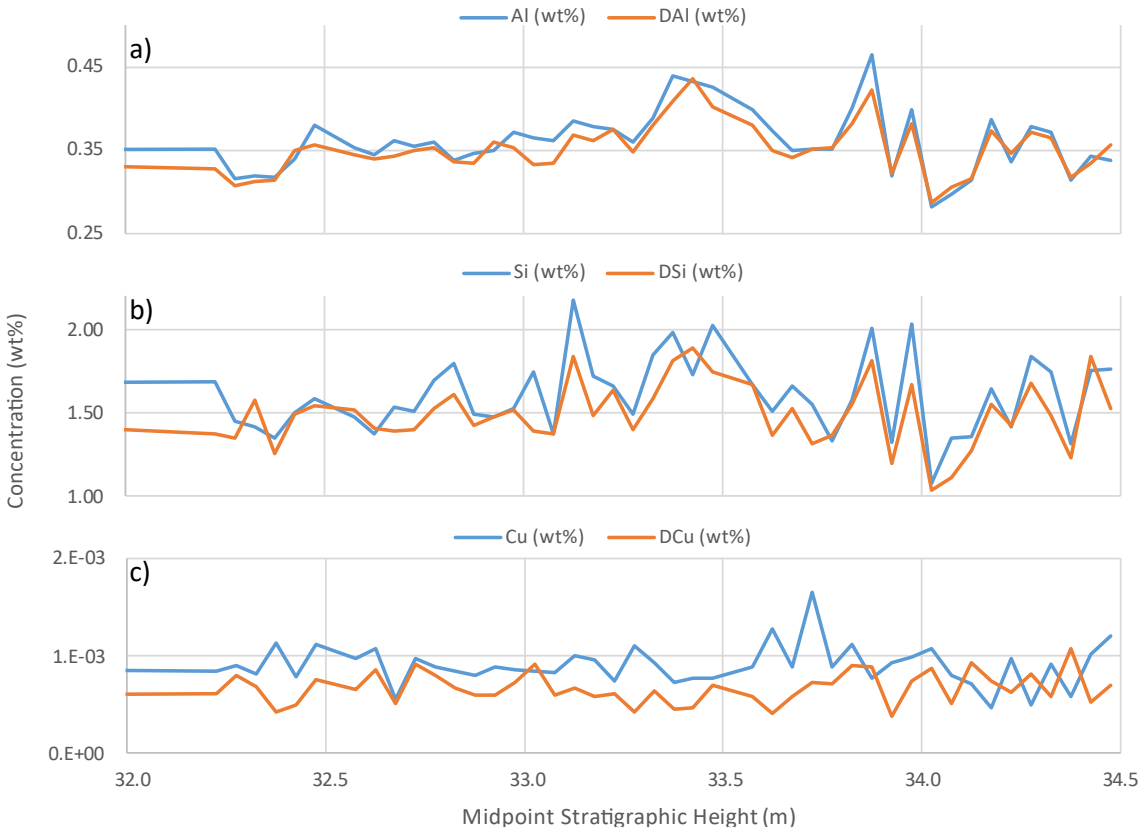

Figure 24a: measured Al values using 25 µm beam size versus measured Al values using 200 µm beam size (DAl), 24b: measured Si values using 25 µm beam size versus measured Si values using 200 µm beam size (DSi), 24c: measured Cu values using 25 µm beam size versus measured Cu values using 200 µm beam size (DCu).

As exemplified by Figures 24a-c, elements such as Al and Si (R^2 = 0.8958, p-value = $1.01E^{-24}$ < 0.05 and R^2 = 0.6812, p-value = $2.99E^{-13}$ < 0.05 respectively) display similar trends. Elements showing poor correlation in Fig. X, such as Cu (R^2 = 0.0032, p-value = 0.70 > 0.05) on the other hand are characterized by large discrepancies between measurements with 25 µm and 200 µm beam sizes (Fig. 24c). Given that µXRF is used to determine bulk concentration of the samples rather than to target specific mineral inclusions, using a 200 µm beam size is preferred. However, since a considerable amount of data was already measured using the 25 µm beam size and available for use, beam size parameters were not changed. The impact on absolute measured values for all elements (and especially trace elements) is considerable, thus consistency is key when selecting beam size parameters.

4.2.5.2. Sample Focusing

54 samples were measured twice using identical experimental parameters, including (x,y,z) coordinates for spot analysis but with different focusing settings; AutoFocus on Each Sample (AFES) and AutoFocus on Each Point (AFEP). According to standard operating procedures, autofocusing is carried out on each sample (at an optical magnification of x100, using AFES). Re-measurement of the samples was carried out after autofocusing (at x100 optical magnification) on each spot (AFEP), changing the z-coordinate of each spot measurement. As illustrated by Fig. 25 considerable differences can be observed between the both datasets.

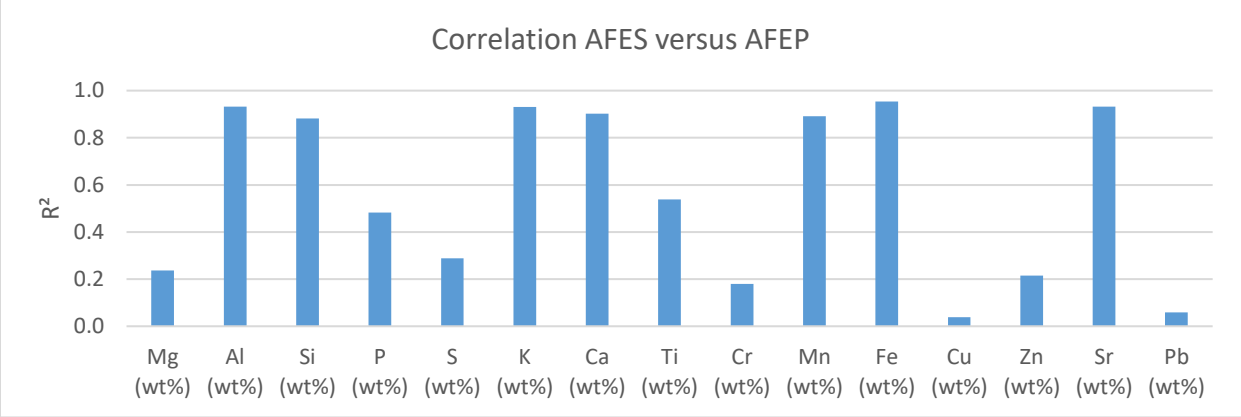

Figure 25: R^2 values between geochemical element concentrations (wt%) measured using autofocus on each sample (AFES) versus autofocus on each point (AFEP).

Large differences in R^2 values can be observed; elements such as Al, Si, K, Ca, Mn, Fe and Sr are measured quite robust and have R^2 values above 0.8; elements such as Cr, Cu and Pb on the other hand show very poor (to none) correlation with R^2 values well below 0.2.

As exemplified by Figures 26a-c, elements such as Al and Si (R^2 = 0.9326, p-value = $4.03E^{-32}$ < 0.05 and R^2 = 0.8813, p-value = $1.01E^{-25}$ < 0.05 respectively) display similar trends. Elements showing poor correlation in Fig. 25, such as Cu (R^2 = 0.0382, p-value = 0.16 > 0.05) on the other hand are characterized by large discrepancies between measurements autofocusing on each sample and autofocusing on each point. As observed for beam size parameters, different focusing parameters also have a considerable impact on absolute measured values. Again, to remain consistent with previous measurements that were made available, the AFES methodology was applied for measuring all samples in this work.

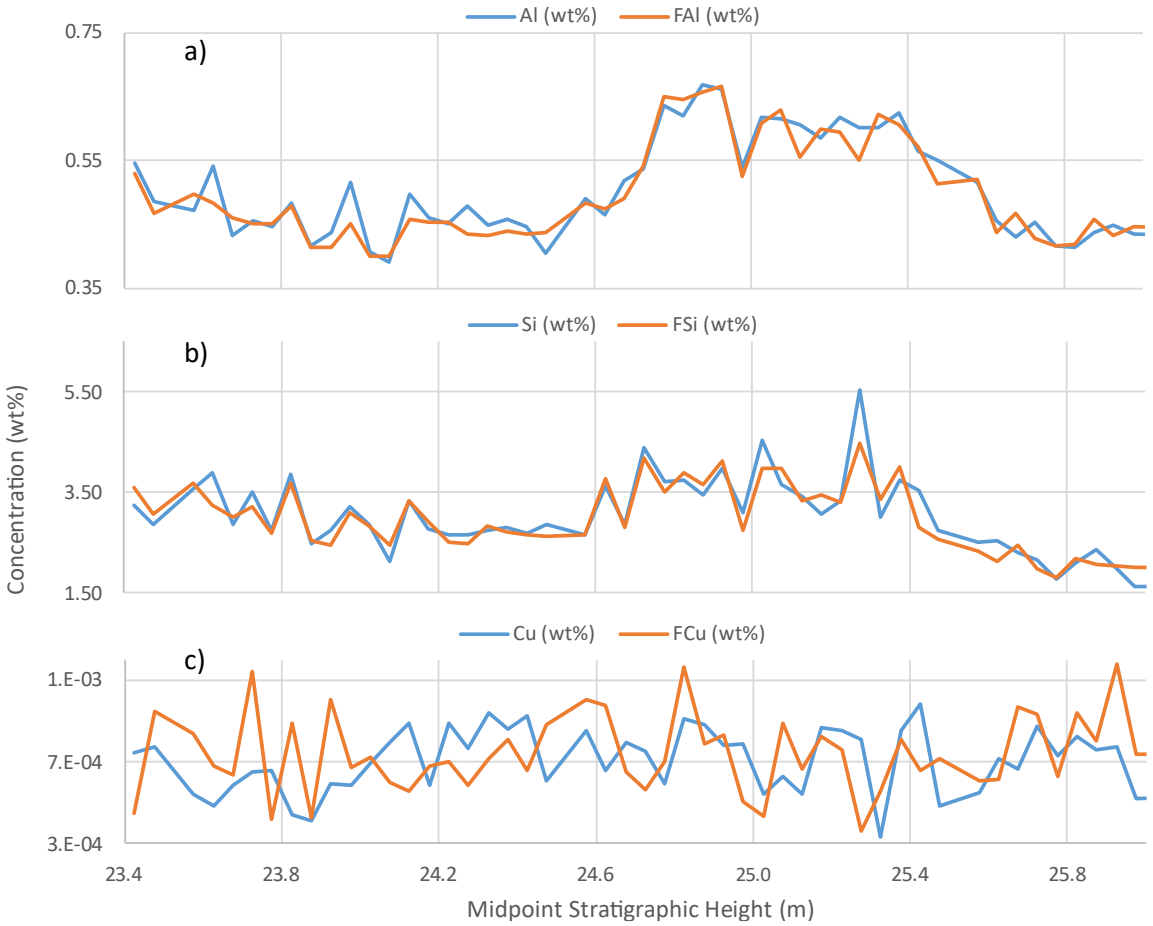

Figure 26a: measured Al values using autofocus on each sample versus measured Al values using autofocus on each point (FAl), 26b: measured Si values using autofocus on each sample versus measured Si values using autofocus on each point (FSi), 26c: measured Cu values using autofocus on each sample versus measured Cu values using autofocus on each point.(FCu).

4.2.5.3. Repeatability and Sample Homogeneity

Potential sample homogeneity and repeatability of the µXRF measurement on Hallembaye chalk samples was assessed using randomly selected sample HAL18_A_30.85. This sample was subsampled 5 times before powdering to yield subsamples "…_30.85a" to "…_30.85e". An analysis of variance (ANOVA) is used to assess both sample homogeneity as well as repeatability.

To test repeatability, samples HAL18_A_30.85a to HAL18_A_30.85e were measured 6 times by the same operator, using the same equipment, using the same parameters on a short period of time. The ANOVA was carried out on mass concentration data for Mg, Al, Si, P, S, K, Ca, Ti, Cr, Mn, Fe, Cu, Zn, Sr and Pb at a significance level of $\alpha = 0.05$. The null hypothesis in both cases is: "there is no significant difference between measurements of sample HAL18_A_30.85". For repeatability, the ANOVA was carried out for each subsample measured during 6 different runs. Table 3 below summarizes the ANOVA results for all subsamples of HAL18_A_30.85.

Repeatability (ANOVA)	F	p-value	F crit
HAL_18_A_30.85a	9.46E-06	1	2.323126
HAL_18_A_30.85b	7.11E-06	1	2.323126
HAL_18_A_30.85c	2.60E-05	1	2.323126
HAL_18_A_30.85d	3.57E-05	1	2.323126
HAL_18_A_30.85e	1.67E-05	1	2.323126

Table 3: ANOVA results for repeatability of µXRF measurement on sample HAL18_A_30.85.

For all subsamples, p-values equal unity (> 0.05) and therefore, the null hypothesis cannot be rejected. This means that there is no significant difference between the consecutive measurements of the subsamples taken from HAL18_A_30.85, which is indicative of good repeatability.

Similarly, for sample homogeneity, the ANOVA was carried out for each run on subsamples "a" to "e". Based on the ANOVA results summarized in table 4 below, it can be concluded that sample HAL18_A_30.85 is statistically homogenous. Even though visual assessment would indicate some differences, these are not statistically significant.

Homogeneity (ANOVA)	F	p-value	F crit
Run 1 (a - e)	9.05E-06	1	2.502656
Run 2 (a - e)	2.32E-05	1	2.502656
Run 3 (a - e)	4.74E-05	1	2.502656
Run 4 (a - e)	5.41E-05	1	2.502656
Run 5 (a - e)	4.52E-05	1	2.502656
Run 6 (a - e)	1.63E-05	1	2.502656

Table 4: ANOVA results for sample HAL18_A_30.85 homogeneity assessment.

4.3. Low-Field Magnetic Susceptibility

Magnetic susceptibility (MS) measurements, carried out at low external magnetic field, allow for a quick analysis of bulk rock samples and are able to generate valuable, large high-resolution datasets. Measuring low-field MS of carbonate rocks often gives insight in the paleoclimatic and/or paleoenvironmental setting of the carbonate environment (da Silva et al., 2013). This is because the MS signal in bulk carbonate samples is often dominated by the presence of paramagnetic components that are supplied as impurities via detrital input, making MS an excellent proxy that – in some cases – can be linked to sea level variations (Ellwood et al. 2000; da Silva et al. 2009) or climate (Stage, 2001). Moreover, in case climatic variations that lead to a change in detrital influx (from aeolian or fluvial sources) leave a primary imprint on the MS signal can be linked to astronomical forcing, MS is an ideal candidate to be used in cyclostratigraphic studies (da Silva et al. 2015; Dinarès-Turell et al. 2018). Ellwood et al. (2000) reported that MS could be used in combination with a cyclostratigraphic approach to distinguish detrital input versus carbonate chemistry in marine rocks.

4.3.1. Origin of the Magnetic Susceptibility Signal

Considering magnetic properties of matter at the (sub)atomic scale, it can easily be imagined that all materials possess some sort of magnetic properties. Whilst some materials inherently carry a permanent magnetization, others will only gain bulk magnetic properties when exposed to an external magnetic field. When exposing a material to a weak, uniform external magnetic field and measuring its response to that applied field, one basically records the bulk, low field magnetic susceptibility of that material (hereafter denoted as MS or χ). The magnetic susceptibility χ (or, in other words the relative permeability $\mu_r - 1$) relates the induced magnetic field M in the material with the external magnetic field H and is a degree of magnetization of that material (IUPAC, 2019) (6):

$$M = \chi H \tag{6}$$

The MS signal not only depends on which magnetic minerals are present in the material, but also the mineral grain size, shape and the orientation thereof (da Silva et al., 2009). Based on bulk magnetic properties and response to an external magnetic field, three types of material magnetism can be distinguished; diamagnetism, paramagnetism and ferromagnetism (Kodama and Hinnov, 2015). Furthermore, diamagnetic, paramagnetic and ferromagnetic minerals contribute differently to the MS signal. Diamagnetic minerals, such as quartz (SiO_2) and calcite ($CaCO_3$), only have paired electron spins and counteract the applied external magnetic field and thus lead to a weak, negative MS signal (Ellwood et al. 2000; da Silva et al. 2013). Materials containing species with free electron spins (e.g. Fe ions in minerals) are either paramagnetic or ferromagnetic depending on non-collective or collective spin behavior respectively. Consequently, paramagnetic minerals (such as clay minerals) show a small, positive response (and thus small positive MS signal) and ferromagnetic minerals a very large, positive response (da Silva et al., 2013). Given the nature and magnitude of their response to the applied external magnetic

field, each mineral will have a unique impact on the eventual MS signal. Ferromagnetic species leave a dominating imprint on the MS signal even when present in low amounts (da Silva et al., 2013; Stage, 1999).

Because the signal recorded via bulk magnetic susceptibility measurements is a composite of all magnetic minerals present in a sample, it can be challenging to decipher the MS signal. Especially when using the MS signal for cyclostratigraphic studies, attributing environmental or climatic processes to the exact source of the cyclostratigraphic signal may not be so straightforward (Kodama and Hinnov, 2015). Regardless, numerous studies by da Silva et al. (2009, 2013, 2015), Ellwood et al. (2000) and Stage (1999, 2001) have proven that, if environmental mechanisms can be related to the nature of the signal, MS measurements are invaluable as a tool for cyclostratigraphic studies. In order to test whether the MS signal is of primary or secondary origin, a positive correlation with geochemical elements such as Al and Ti can be a first indication that the primary signal remained preserved (da Silva et al. 2015).

4.3.2. Experimental Set-up and Parameters

Low field alternating current bulk magnetic susceptibility measurements were carried out at Liège University, Pétrologie sédimentaire, B20 under supervision of Prof. Dr. Anne-Christine da Silva using the MFK2 Kappabridge laboratory instrument (Fig. 27) (Agico, 2018).

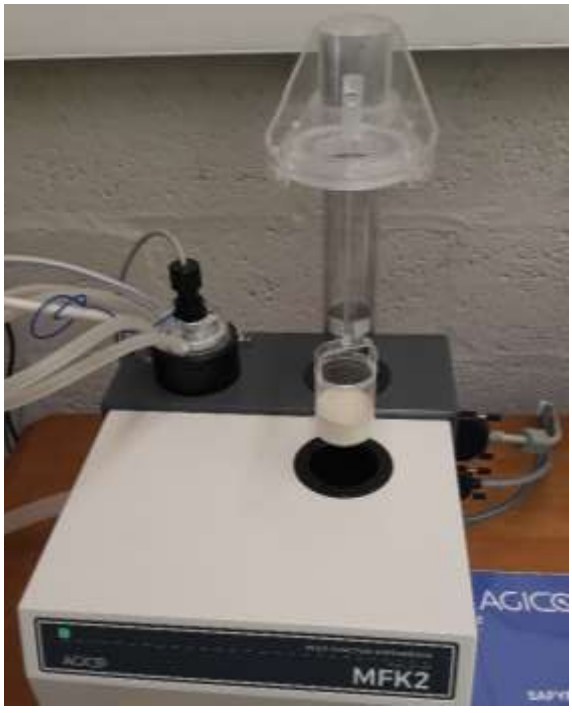

Figure 27: ULiège Kappabridge MFK2 used for MS measurements

After thermal equilibration of the equipment during 10 minutes, a series of 10 empty-coil measurements is carried out automatically using the accompanying software as a start-up routine. Then, the equipment was calibrated (by automatically adjusting the gain setting) based on the magnetic susceptibility

measurement of a manual holder containing a standard. A plastic sample holder with a low magnetic susceptibility is used to contain and transport the sample in the equipment. A holder correction routine is carried out by first measuring the empty holder and subtracting the magnetic susceptibility value from sample MS-values (Agico, 2018). Prior to the measurement, at least 5.00 g of sample was weighed in the designated plastic sample holder using a Sartorius balance (uncertainty in the second decimal place). Per sample, a series of 6 MS measurements were carried out using an automated, software-controlled routine at a frequency of 976 Hz and field of 200 A/m at room temperature. The measured in-phase (real) component of the magnetic susceptibility is normalized to obtain the mass-normalized magnetic susceptibility (expressed in m^3/kg), which represents a volume magnetic susceptibility multiplied by a reference volume of 1 m^3 and divided by the sample mass (Agico, 2018; da Silva et al., 2009).

4.3.3. Data Measurement and Treatment

As magnetic susceptibility measurements are carried out on the bulk powdered sample, extreme outliers due to local sample heterogeneity as observed in µXRF measurements are not expected. For the sake of consistency, similar data treatment for outlier identification and removal as described in Chapter 4.2.4. has been applied on the MS dataset.

Initial trial runs identified a biased MS value for each first measurement of chalk sample compared to subsequent measurements. Therefore, for each sample, the first data point measured in a series of 6 was discarded prior to any outlier identification, removal and averaging and standard deviation determination. See the appendix 11.6 for all raw MS data, data treatment and outlier removal.

4.3.4. Methodology Development

A one-day trial session was organized to finetune the existing MS-measurement methodology on the Hallembaye chalk samples. Open key questions included the required minimum sample mass, number of measurements per sample as well as the sample nature (powdered versus rock).

For this purpose, 37 measurements were carried out on samples arbitrarily selected from different parts of the Hallembaye section. As can be observed on Fig. 28, MS standard deviations remain quite consistently below 11.10^{-11} m^3/kg for samples masses larger than 5.00 g. For powdered samples, masses below 5.00 were tested as well given a large set of powdered samples was readily available, albeit at lower quantities (< 5.00 g). At lower sample masses, it can be expected that the MS signal is proportionally weaker for identical samples and consequently precision is expected to decrease (or standard deviations are expected to be larger). Overall, standard deviations for powdered samples are consistently smaller compared to rock samples with comparable masses.

MS measurements on powdered samples with a mass higher than 5.00 g consistently have a smaller standard deviation (Fig. 28). Also, powdered samples have the added advantage over rock samples that no random, unidentified inclusions can be present in the sample that might strongly affect the

measurement and the eventual MS signal. Therefore, it is advisable to carry out the MS measurements on at least 5.00 g of powdered chalk samples.

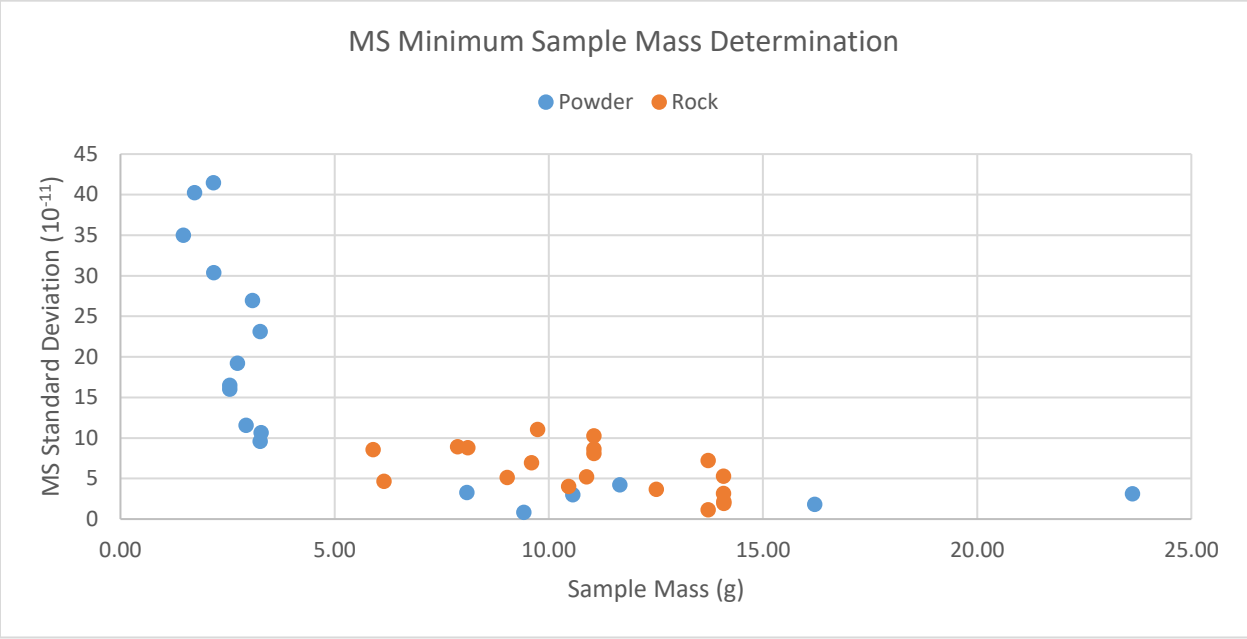

Figure 28: MS standard deviations versus sample mass based on 37 measurements of 10 randomly selected samples.

Potential drift assessment was, amongst others, carried out on powdered chalk sample ENCI19_A_15.25. It can be observed on Fig. 29 that in this case – apart from some apparent increased drift for the last 3 datapoints – the first measurement of a series of 10 often displays deviating values. Similar observations have been made for other samples. Regardless, measured MS-values remain consistent throughout the series of measurements and, given the small sinusoidal fluctuations, a set of 5 datapoints from 6 measurements per sample should result in a representative dataset.

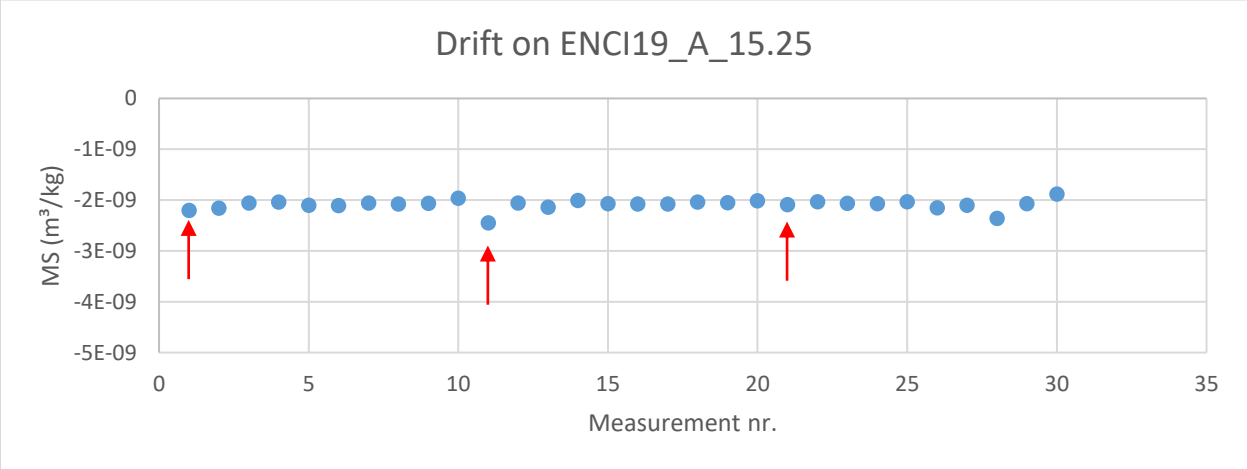

Figure 29: 3 series of 10 consecutive MS measurements of sample ENCI19_A_15.25. Red arrows indicating first measurement of a series of 10.

4.4. Spectral Analysis

Spectral analysis is one the most important tools for hypothesis testing in cyclostratigraphy (Meyers, 2012). A variety of tools are at our disposal via the 'Astrochron' package, useful for the application of astrochronology maintained by Prof. Stephen Meyers (University of Wisconsin-Madison, USA), in the open source software 'R' (R-project) (Chambers, 2021).

4.4.1. Sample Resolution and Nyquist Frequency

Elemental analysis of chalk sampled every 5 cm results in a discrete dataset, which inherently imposes a limit to the highest frequency component that can be extracted from that dataset; the Nyquist frequency, defined by the reciprocal value of 2 times the sampling interval (Weedon, 2003). In the case of a sampling frequency of 0.05 m, the Nyquist frequency equals 10 cycles/m. Lastly, it should be highlighting the importance of consistency during sampling given definition of the Nyquist frequency as well as further numerical analyses, which assume constant time or depth intervals (Weedon, 2003). In case the stratigraphic series contains discrete datapoints with non-constant spacing, a linear interpolation can be carried out to obtain a discrete series that satisfies the Nyquist theorem of uniform sampling (Vaidyanathan, 2001)

4.4.2. Detrending

Prior to time-series analysis, pre-processing of the data series is required to remove undesired (e.g. artificial) trends and other artifacts. Whenever the time-series mean value displays a trend (i.e., a non-stationary series), this trend is to be removed before even attempting any further spectral analysis (Weedon, 2003). The most readily available method of detrending that is available in the Astrochron package is a basic, linear detrending. However, the Si and Ca signals are more complex, with a decreasing trend in the Vijlen (here from 11.75 to 28.00 m) and a slightly increasing trend in the Lixhe 1 (28.00 onwards) (Fig. 30, left). Given this overall non-linear trend (that can also be observed to some degree for other elements), detrending was carried out by subtracting an exponential fit from each signal as demonstrated for Si (Fig. 30) and Ti/Al (Fig. 31).

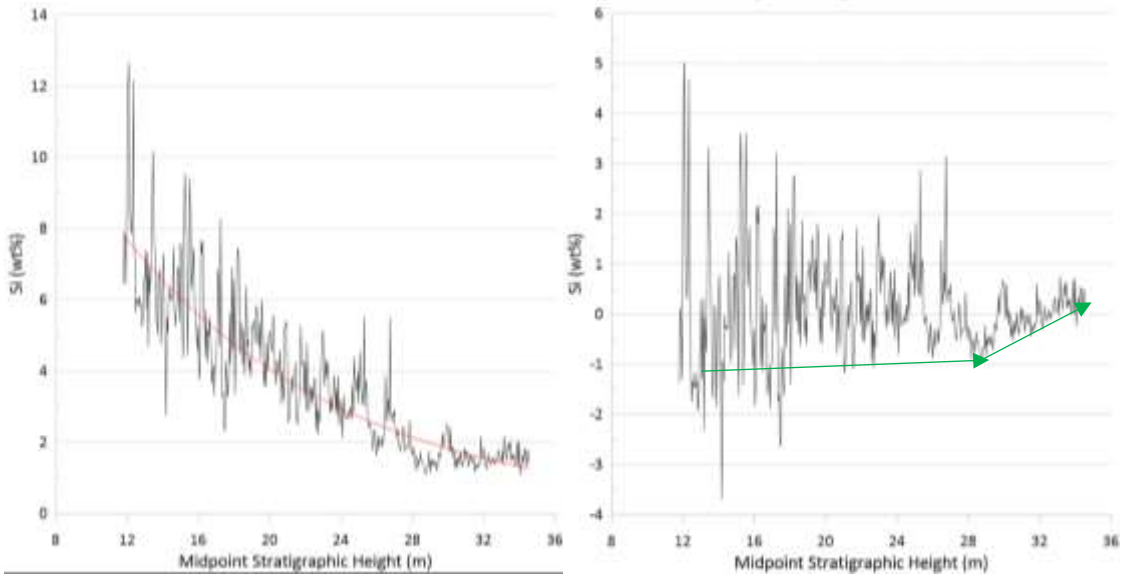

Figure 30: Left: fitting of exponential $y = 20.052e^{-0.08x}$ (red curve). Right: subsequent subtraction to yield the exponentially detrended Si-signal, green arrows: potential new trend due to applied methodology.

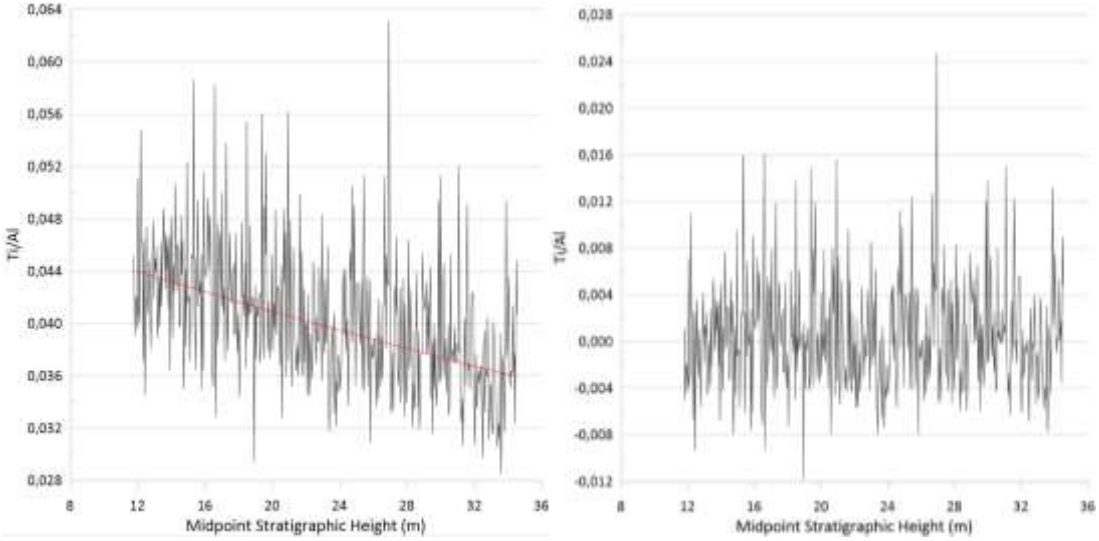

Figure 31: Left: fitting of exponential $y = 0.049e^{-0.009x}$ (red curve). Right: subsequent subtraction to yield the exponentially detrended Ti/Al-signal.

Even though exponential detrending might induce a new trend in the signal as demonstrated using the green arrows on Fig. 30, this method was selected out of many for multiple reasons. Firstly, more complex polynomial functions are avoided, preventing removal of smaller-scale trends that might correspond to longer astronomical cycles (e.g. eccentricity – depending on the record in question). Secondly, since both (quasi) linear (Fig. 31) and non-linear (Fig. 30) trends can be easily approximated, it can be used consistently for all signals in this record. Other options, such as a lowpass bandpass filtering, were considered for detrending the signals but could not be used consistently with the same input parameters (such as cut-off frequency).

4.4.3. Periodogram

Variable quantities may show obvious periodic changes, as well as less obvious ones, so-called hidden periodicities (Schuster, 1898). By going from the spatial domain to the frequency domain (expressed in cycles per m or cycles/m), some of these hidden periodicities may be revealed provided they are of sufficient magnitude to be observed in the frequency domain. The periodogram of a finite time series, obtained by performing a discrete Fourier transformation, forms the basis of spectral estimation and can be considered to be the rawest form of a spectrum (Weedon, 2003). Prior to using more advanced means of calculating spectra, a periodogram offers a quick and easy first view on the power spectral density at specific frequencies in the signal (Percival and Walden, 1993), as is exemplified for Si (Fig. 32).

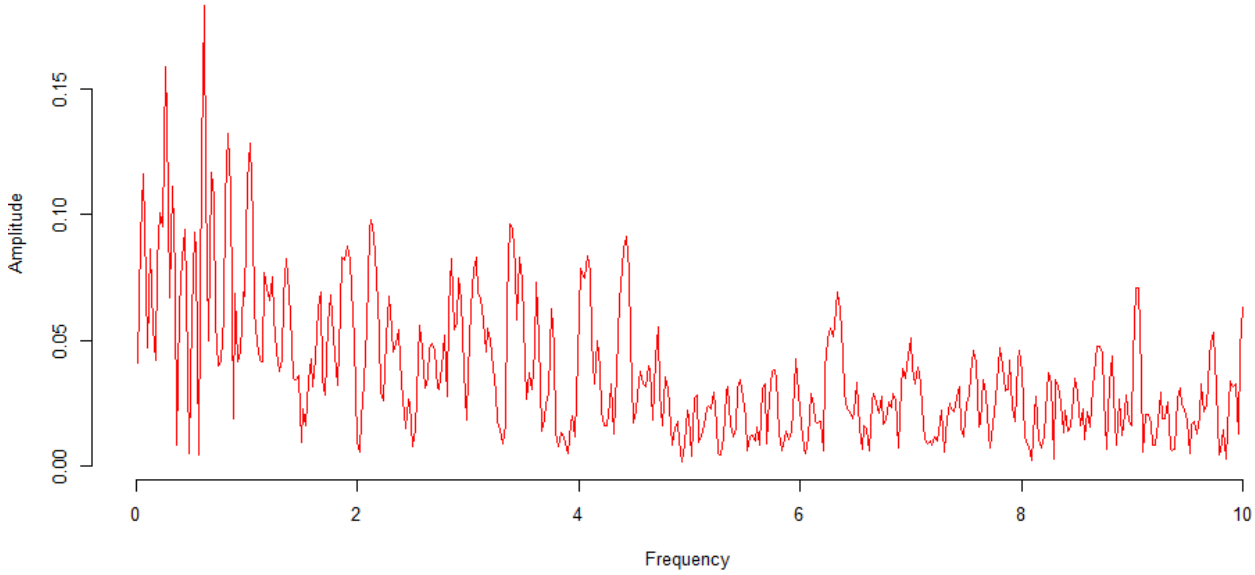

Figure 32: Basic periodogram of Si, with amplitude in function of the frequency

One of the shortcomings of using a basic periodogram is the presence of so-called periodogram leakage, which in essence is caused by the finite nature of the time-series signal. The periodogram leakage introduces a bias that causes spectral power to be estimated incorrectly (Percival and Walden, 1993). More recent methods, such as the Multitaper method (MTM) make use of tapering to account for the finite nature of the time-series (Thomson, 1982).

4.4.4. MTM Power Spectrum

The multitaper (MTM) spectral analysis method was first presented by Thomson in 1982 and is now widely used as a tool for spectral analysis within the field of geosciences (Prieto et al. 2009). Estimation of the power spectral density (or spectral power) is based on the use of a set of orthogonal tapers before carrying out a Fourier transformation of the data series (Prieto et al. 2009). This way, a specific frequency bandwidth contains an optimal power concentration, improving accuracy (or lowering bias e.g. due to periodogram leakage) whilst still keeping sufficient spectral resolution – something that is especially important for the often small, high frequency spectral peaks that are easily masked (Weedon 2003; Meyers 2012).

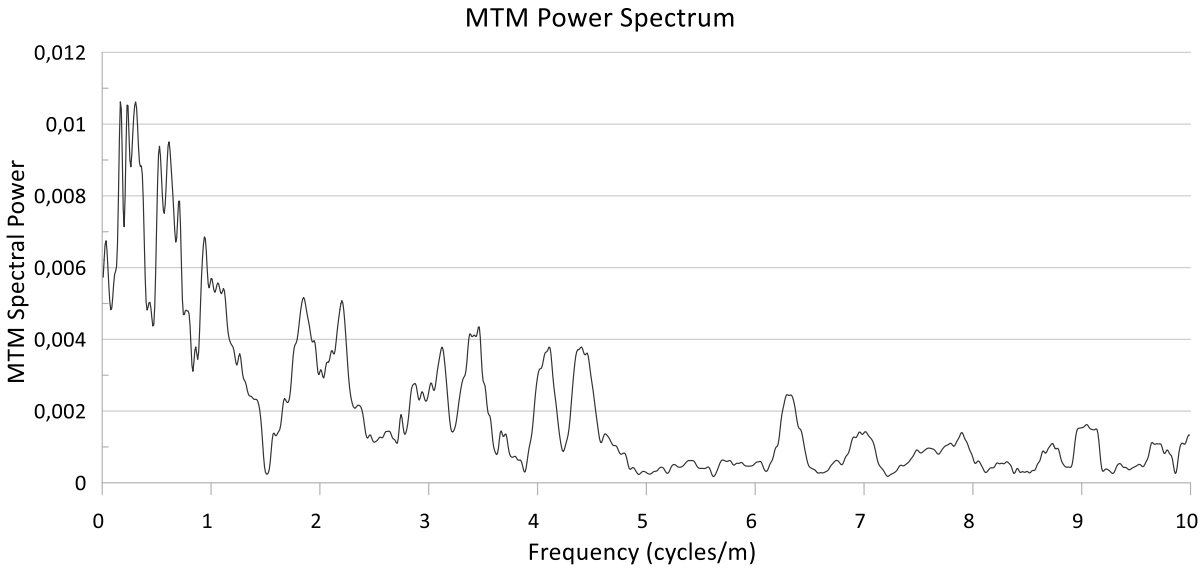

Figure 33: MTM Power Spectrum of exponentially detrended Si

As can be seen on the MTM spectrum for Si on Fig. 33, again spectral power is displayed in function of frequency (cycles/m). High spectral power at a specific frequency is indicative for the presence of a cyclical component in the time-series signal at that given frequency. Investigation of the MTM power spectrum therefore allows identification of (potentially hidden) periodicities. Because the spectral power of the obtained peaks is in essence meaningless, interpretation thereof only becomes valid when the statistical significance is tested first. Many different approaches and techniques are available, but in this work (see Chapter 6) the most commonly used “autoregressive-1” (AR1) will be used (Meyers, 2012). More precisely, the AR1 (95%) confidence levels were added for an estimation of the significance of spectral components. See appendix 11.1 for more details on the script and used parameters for the MTM analysis.

4.4.5. Evolutive Harmonic Analysis

Evolutive Harmonic Analysis (EHA), based on the MTM (Thomson, 1982), is a more advanced tool for power spectral analysis. This time-frequency technique enables identification of temporally changing dominant frequencies throughout the record. This is achieved by, instead of analyzing the spectral power of a complete signal in one step (such as the basic periodogram or MTM power spectrum), following a step-by-step, sliding window Fourier approach (Thomson 1982; Meyers et al. 2001). The sliding window (which has a predefined width, expressed in m) acts as a framework in which MTM harmonic analysis is carried out and, is moved sequentially through the interval (Meyers et al. 2001). As a result, one no longer obtains a 2D-spectrum summarizing spectral power in function of frequency but spatially resolved 3D spectrum instead (see Fig. 34). This is especially useful when encountered with records containing hiatuses or changes in the sedimentation rate that would otherwise lead to complex 2D power spectra that can be easily misinterpreted (Meyers et al. 2001).

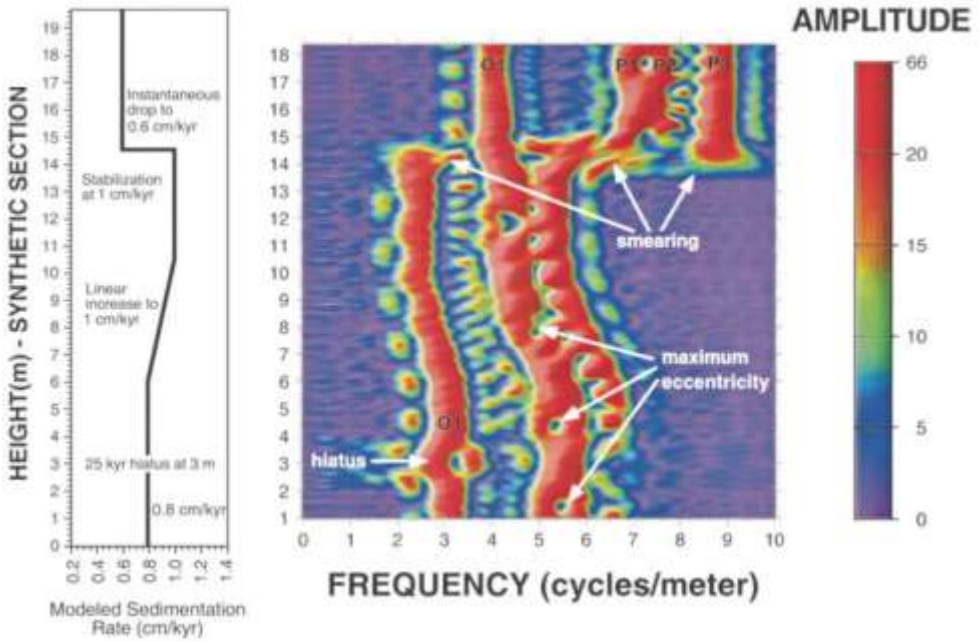

Figure 34: EHA based on a model input of orbitally forced insolation, altered by modifications in sedimentation rate and a hiatus (Meyers et al. 2001).

The application of EHA, as well as construction of the more basic periodogram and MTM power spectrum, provides valuable insight in the data series (spatial domain) by revealing dominant spectral components, and potentially can even reveal indications of hiatuses and/or changes in sedimentation rates (Meyers et al. 2001). Changes in sedimentation rates are exemplified as well in Fig. 34, where an increase in sedimentation rate from 0.8 cm/kyr to 1.0 cm/kyr is matched by a decreasing trend in frequency of the most dominent components (amplitude power in this example). However, as long as knowledge on sedimentation rate (and potential hiatuses) is missing, the data series can not be transformed from the spatial domain to the time domain, which is required when attempting astrochronology to eventually date the record.

4.4.6. Bandpass Filtering

Based on spectral analysis, either MTM power spectrum or EHA results, certain key frequencies – if present – can be separated using band-pass filtering (Weedon, 2003). A significant peak at a given frequency can be used to design a bandpass filter, as illustrated in the example (Fig. 35) below which shows the power spectrum of a sample dataset, with an identified peak around 2.7 cycles/m, and the gain spectrum of the filter.

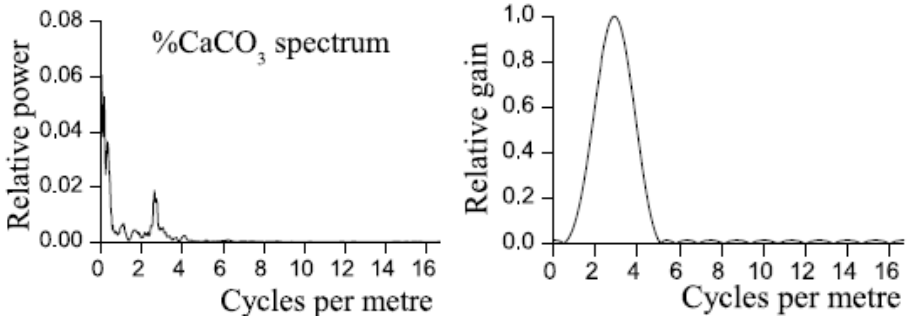

Figure 35: Left: example power spectrum used to design a band-pass filter
Right: gain spectrum of the bandpass filter (Weedon, 2003).

The obtained band-pass filter (e.g. Fig. 36) signal can be used in many ways, for example to identify phase shifts or phase delays in the original dataset (Weedon, 2003). Also, the amplitude modulation of certain cycles can be identified using bandpass filtering (Boulila et al., 2018). Another way of looking at bandpass filtering is their use of isolating a certain frequency-range of the data series – i.e. by extracting a cycle of interest (Dinarès-Turell et al. 2018). This way, if the cycle of interest can be attributed to a specific Milankovitch cycle, the bandpass filter can be of use to count the amount of Milankovitch cycles present in the record. In either case, the designed bandpass filter needs to be broad enough (in terms of frequency) to correctly capture the amplitude modulation of the original data series of interest (Weedon, 2003).

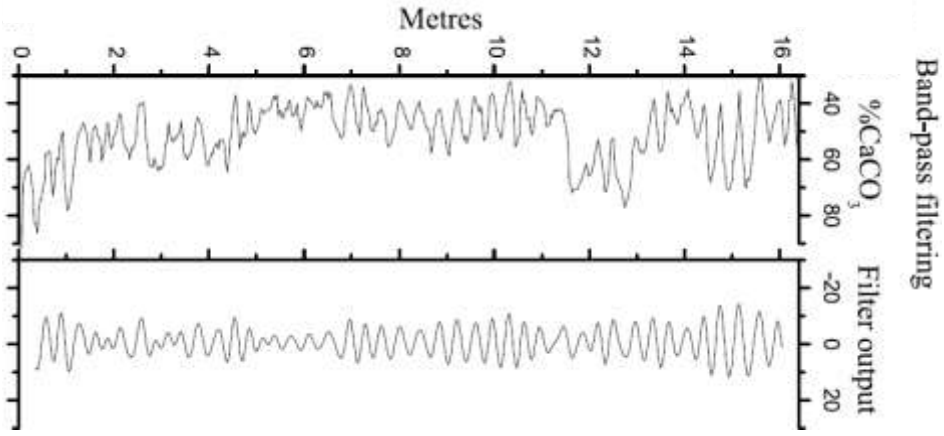

Figure 36: Example of bandpass filter output and the corresponding data series ($CaCO_3$) (Weedon, 2003).

4.4.7. TimeOpt

Astronomical climate forcing is not necessarily translated linearly into the stratigraphic record. Additional presence of potential hiatuses, noise and uncertainties on the length of Earth's astronomical cycles (Chapter 2.3.4.) can further lead to challenges in the application of quantitative astrochronology (Meyers, 2015).

One way of assessing the sedimentation rate for proxy records that are hypothesized to have a precession-eccentricity imprint is by using the 'time scale optimization' or TimeOpt method (Meyers, 2015, 2019). Sedimentation rates are tested as such that the precession (or short eccentricity) amplitude modulation as well as the concentration of power for precession and eccentricity are optimized. By nature, this method can be considered to be 'inverse' by readily assuming presence of Milankovitch cycles in the stratigraphic record (Meyers, 2015). Consequently, this method is able to provide added value once the potential presence of Milankovitch cycles has been indicated by spectral analysis of the spatial-domain signal.

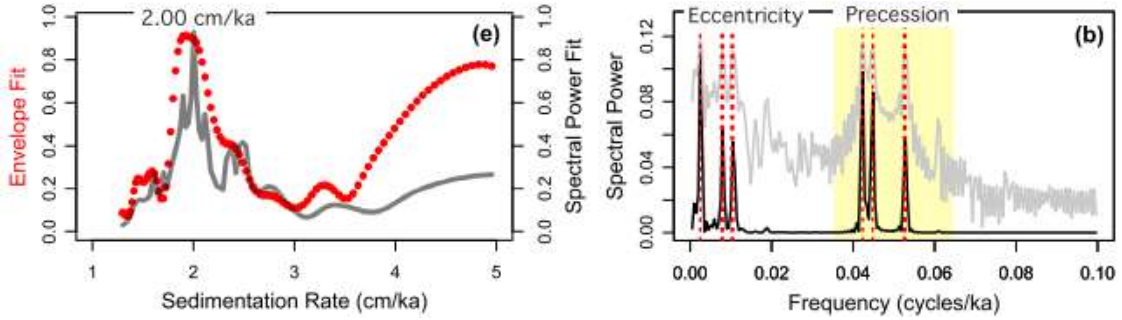

Figure 37: Left: sedimentation rate estimations using TimeOpt. Right: Frequency domain power spectrum with optimized spectral power for eccentricity and precession targets for a sedimentation rate of 2.00 cm/kyr (Meyers, 2015).

Ideally, the eccentricity and precession targets (see Fig. 37) should have a link with theoretical astronomical models (Laskar et al., 2004) as described in Chapter 2.3. The nominal TimeOpt method assumes that the astronomical signal was translated into the record with a constant sedimentation rate (Meyers, 2015). Even though the TimeOpt method is able to test a large set of predetermined sedimentation rates (e.g. 1000) within a given range (e.g. 1.0 cm/kyr to 10 cm/kyr), it will attempt to optimize the spectral power of the targets for the complete record. When changes in sedimentation rate or hiatuses are present, optimization towards a given sedimentation rate and the corresponding target frequencies will be sub-optional and therefore not representative of the complete record.

4.4.8. eTimeOpt

The evolutive implementation of the time scale optimization is available in the Astrochron package as "eTimeOpt" and allows of the evaluation of sedimentation rate changes using a sliding window approach (Meyers, 2015). If sedimentation rates remain relatively stable within the predefined window, this method can spatially resolve sedimentation rates for the stratigraphic record by moving the window step-by-step, each time carrying out a TimeOpt analysis (Meyers, 2019).

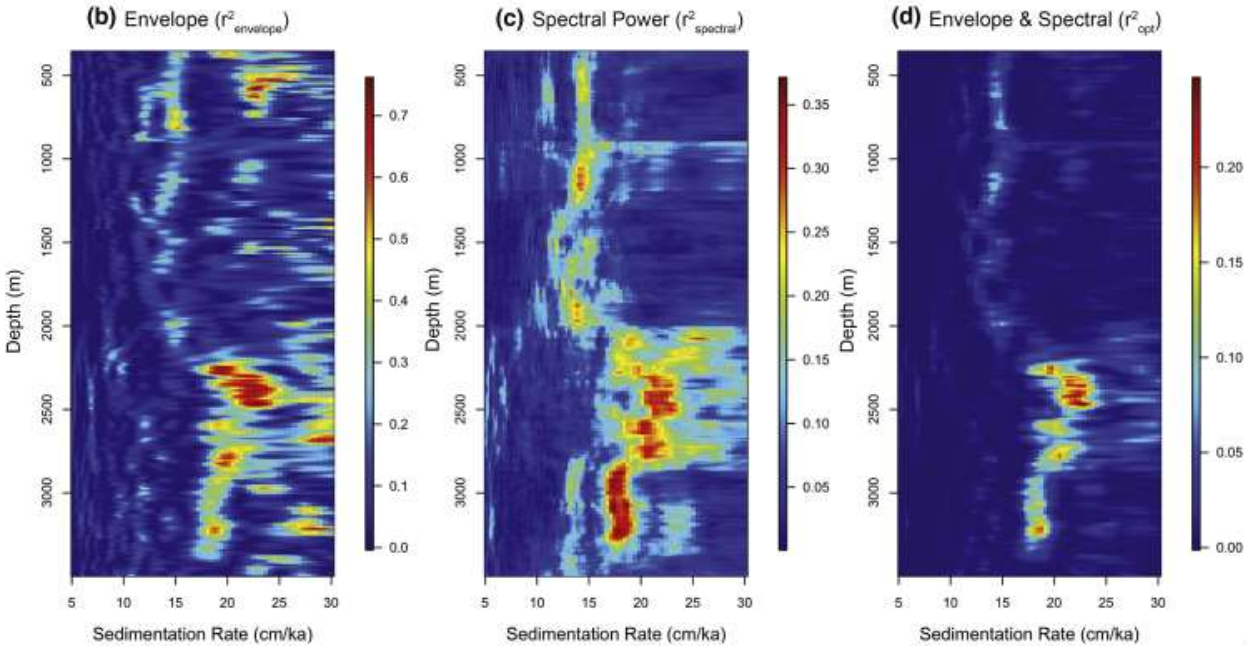

Figure 38: Example of eTimeOpt result by Meyers (2019).

As visualized on Fig. 38, it can be observed that again this method yields a 3D graphical representation where squared Pearson correlation coefficients for amplitude envelope, spectral power fit and a combination of both is obtained for a given range of sedimentation rates along the stratigraphic interval. In this example, sedimentation rates vary roughly between 17 cm/kyr and 23 cm/kyr from a depth of 3500 m to 2100 m (Meyers, 2019).

4.4.9. Tuning of Stratigraphic Series

A stratigraphic series can be converted from the space domain to the time domain by explicitly linking specific depths to age data, or using interpreted sedimentation rates. Tuning of the stratigraphic series is of added value when sufficient age constraints are identified along the interval (either relative or absolute), which can be based on radiometric dating, biostratigraphy, magnetostratigraphy and/or cyclostratigraphy (Hilgen et al. 2010) – the latter yielding in first instance floating astrochronologies (Hinnov, 2018).

5. Results

Most important results obtained by magnetic susceptibility and micro X-ray fluorescence measurements are summarized in this chapter. Because of the differences in nature of geophysical properties compared to the actual elemental composition of a sample (geochemistry), magnetic susceptibility results are treated separately in a first subchapter. In a second subchapter, major and trace elemental composition data of the chalk samples for the complete stratigraphic range from 0 m to 50 m is added to the magnetic susceptibility dataset, providing an overview of the geochemical composition of the chalk and allowing for direct comparison with the magnetic susceptibility. Finally, specific attention is paid to the elemental composition of chalk sampled at a 5 cm-high resolution from 11.75 m to 34.50 m, which are the foundations of subsequent cyclostratigraphic analysis.

5.1. Magnetic Susceptibility

Mass normalized, low field bulk magnetic susceptibility measurements were carried out on 127 chalk samples from the Hallembaye section. Samples collected at a 1 m-low resolution were measured from intervals 0.50 m to 18.50 m and from 22.50 m to 48.50 m. Given sufficient amount of powder was available for samples taken at a 5 cm-high resolution at a stratigraphic height of 18.50 m to 22.45 m, this subset of 81 samples was included.

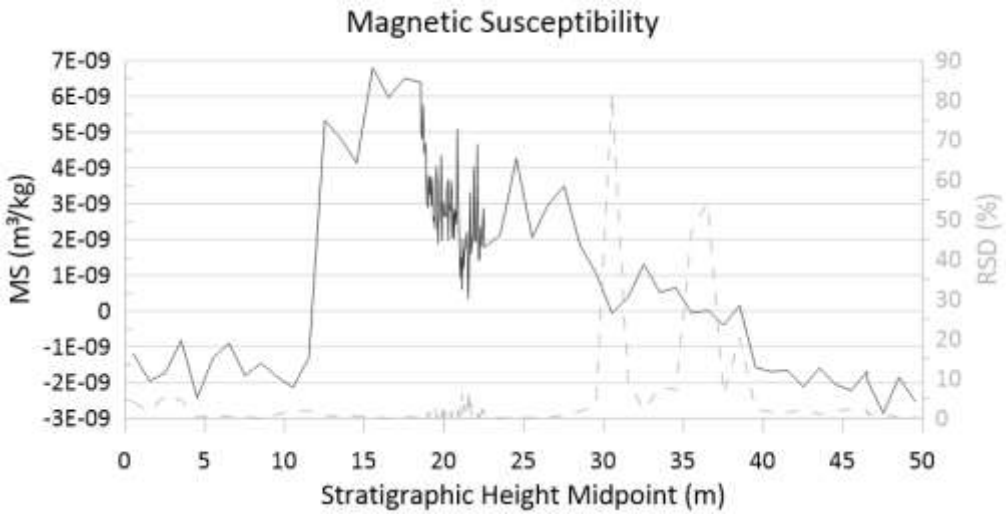

Figure 39: Hallembaye MS (black) and corresponding RSD values (dashed line).

From 0.00 m to 11.50 m, the MS signal remains negative, which corresponds to a dominating contribution of diamagnetic minerals (Fig. 39). From 11.50 m to 38.50 m, a positive MS signal can observed which corresponds to an increasing contribution of either paramagnetic or ferromagnetic minerals. From 38.50 m onwards, MS values remain negative and again correspond to a dominating contribution of diamagnetic minerals.

Relative Standard Deviations (RSD) remain low along the entire interval, except for samples with a corresponding near-zero MS-value. Plotting RSD-values in function of the stratigraphic height (Fig. 39) enables quick identification of samples with near-zero MS-values which are often indicative of transitions in the mineralogical composition of the chalk along the section (given sampling resolution is sufficiently high). The dispersion remains below 10 RSD (%) for absolute MS-values below 5.0 10^{-9} (Fig. 40). Only for a limited amount of samples (4), where the mineralogical composition is as such that MS-values approach 0, high RSD-values of 20 to 84 % can be observed.

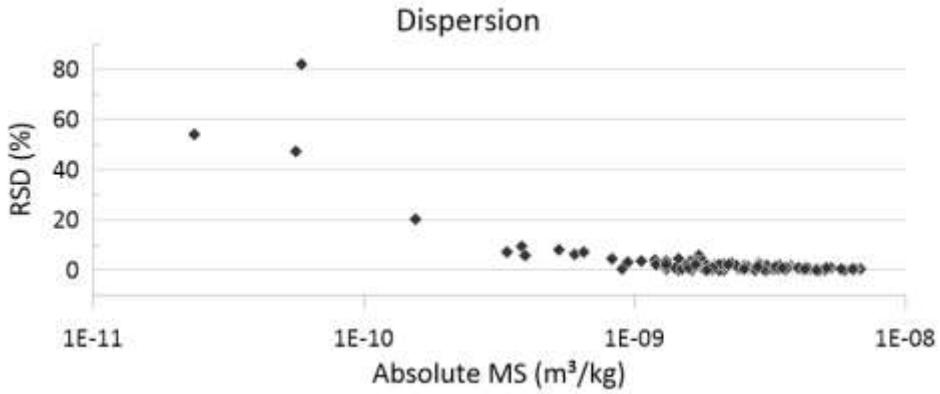

Figure 40: Dispersion of the MS measurements; RSD versus absolute MS values (log-scale).

5.2. Elemental Composition and MS

Major and trace element concentrations were determined for 510 samples via µXRF measurements. Major elements were converted to their corresponding oxides (and carbonate for Ca) of which most relevant ones are plotted on Fig. 41 together with the available MS data.

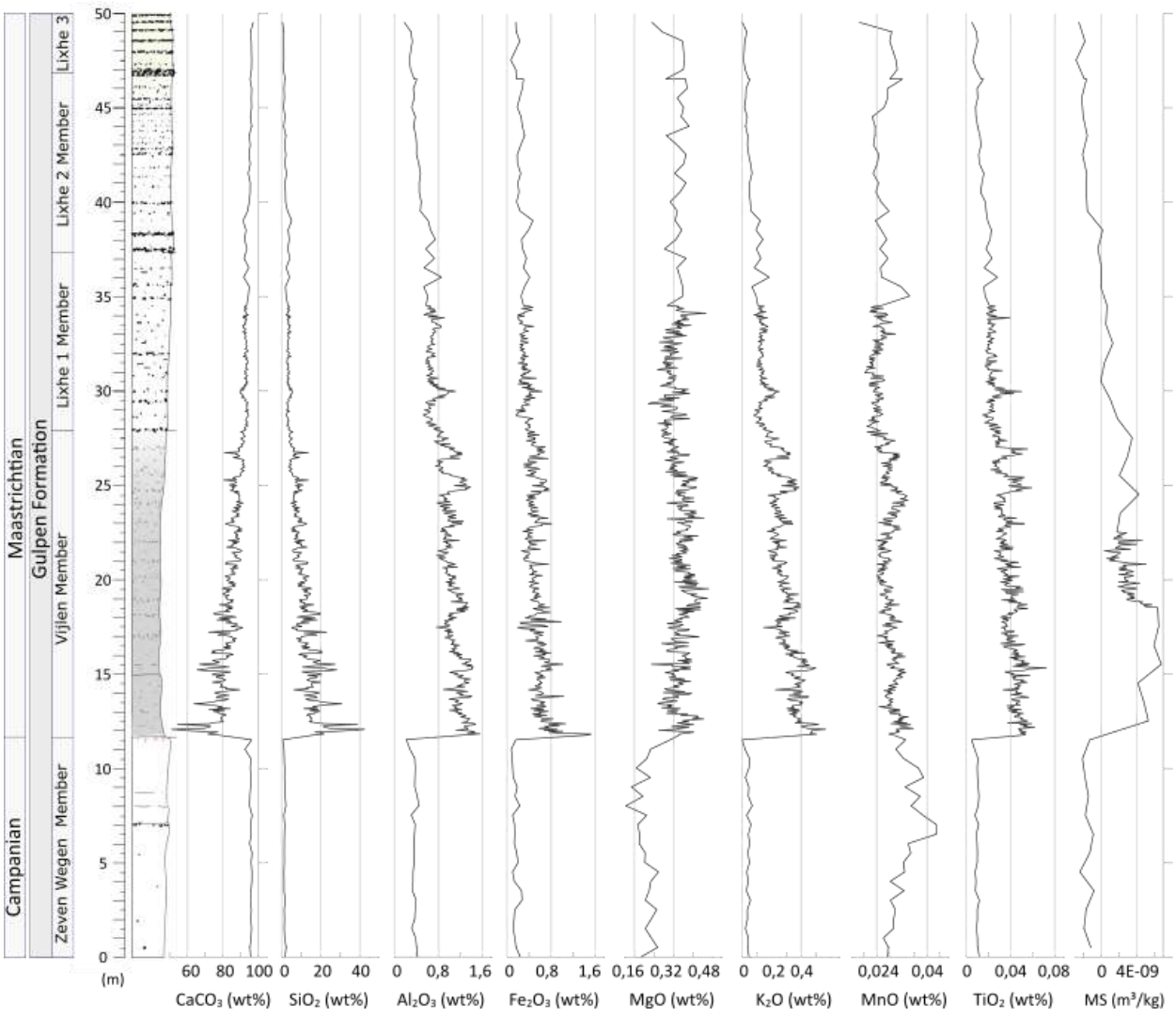

Figure 41: $CaCO_3$, selected oxides and MS complete dataset along the complete stratigraphic height (m) and the lithostratigraphic representation of the Kreco quarry (Vellekoop et al., In prep.).

Based on µXRF measurements, it can be observed that the vast majority of the chalk is composed of calcium carbonate ($CaCO_3$), ranging from 51.01 wt% to 97.23 wt%, averaging at 87.33 wt%. SiO_2 also fluctuate and range from 0.45 wt% to 42.36 wt%, averaging at 8.32 wt% (Table 5).

	Min	Max	Mean
$CaCO_3$ (wt%)	51.01	97.23	87.33
SiO_2 (wt%)	0.45	42.36	8.32
P_2O_5 (wt%)	1.08	6.00	2.08
Al_2O_3 (wt%)	0.18	1.56	0.90
Fe_2O_3 (wt%)	0.07	1.53	0.45
MgO (wt%)	0.13	0.46	0.33
K_2O (wt%)	0.00	0.57	0.23
SO_3 (wt%)	0.10	0.28	0.18
TiO_2 (wt%)	0.00	0.07	0.03
MnO (wt%)	0.02	0.04	0.03

Table 5: Main components of the Hallembaye chalk, expressed as carbonate for Ca and as oxides for all other relevant elements.

Concentrations in $CaCO_3$ vary strongly throughout the section (Fig. 41). Whitish chalk originating from the Zeven Wegen Member has a $CaCO_3$ content averaging at roughly 96 wt%. A sharp decrease in $CaCO_3$ can be observed when crossing the Froidmont Horizon (11.75 m), after which values steadily increase throughout the Vijlen Member. It can also be observed that the chalk/marlstone at the base of the Vijlen Member has a darker, more greyish color which reflects a lower content in $CaCO_3$ compared to the Zeven Wegen Member chalk. In the Lixhe 1 Member the chalk are again lighter in color, which is matched by $CaCO_3$ contents evolving to roughly 93 wt%. Throughout Lixhe 2 and Lixhe 3 Member, $CaCO_3$ contents gradually increase to values of 96 wt% with no observable fluctuations at this resolution (0.50 m). When comparing $CaCO_3$ and SiO_2 concentrations, a mirroring relationship can be observed – a decrease in $CaCO_3$ is matched by an increase in SiO_2 and vice versa.

Comparing geochemical data for SiO_2, terrigenous oxide content (Fe_2O_3, Al_2O_3, K_2O, TiO_2) with the MS signal, similarity of the signals can be observed on Fig. 41. From the base of the section (0.50 m) up to the Froidmont Horizon (11.75 m), flat trends are displayed. Just above the Froidmont Horizon, an increase in SiO_2 and terrigenous oxides content can be observed, as well as an increase of the MS signal towards positive values. These values decrease steadily along the section, with the MS signal dropping below 0 m^3/kg around a stratigraphic height of roughly 35 m.

Both MnO and MgO concentrations remain well below 0.05 wt% and 0.50 wt% respectively, however their stratigraphic variation is different from other oxides. MgO displays an increasing trend at roughly 10 m towards the Froidmont Horizon, after which it fluctuates slightly around an average value of 0.30 wt% for the remainder of the section. MnO on the other hand peaks at a stratigraphic height of 7 m, after which values decrease steadily up to a stratigraphic height of 35 m. Values seem to remain constant for increasing stratigraphic heights up to 45 m, after which an increase can again be observed.

Out of the 510 samples, certain (trace) elements remained undetected in some samples: Cl (508), As (486), Rb (482), Zr (481), Y (355), Ba (106), V (6), K (2) and Cr (1). Following trace elements were detected in each sample: Sr, Cu, Zn and Pb. Finally, elements Na, Rh and Ni remained undetected after outlier removal. Of all trace elements listed in Table 6, Sr is the most abundant, ranging from 417 ppm to 1045 ppm, averaging at 861ppm.

	Min	Max	Mean
Sr (ppm)	417	1045	861
Zn (ppm)	31	53	39
Pb (ppm)	7	16	11
Cu (ppm)	2	17	8
Cr (ppm)	0	23	9
V (ppm)	0	6	2
Ba (ppm)	0	208	48

Table 6: Most relevant trace elements of the Hallembaye chalk, expressed in parts per million.

5.3. Principal Component Analysis

A Principal Component Analysis (PCA) is carried out to reduce data dimensionality and to reveal potential clustering of major elements, trace elements and MS. Given the limited MS dataset, the PCA was carried out on a limited low-resolution dataset containing samples taken every meter from a stratigraphic height ranging from 0.50 m to 49.50 m.

5.3.1. Pearson Correlation Matrix

Prior to carrying out the Principal Component Analysis, correlation of the geochemical elements and the MS signal was verified and summarized via a Pearson correlation matrix. Verification of correlation between at least some of the geochemical elements is required to ensure the PCA is not redundant. Table 7 shows the Pearson correlation matrix, containing Pearson Correlation Coefficients (PCC) for most abundant geochemical elements and MS. Strong positive correlation (> 0.89) between MS and Al, Fe, K, Si and Ti can be observed – indicated in bold on table 7. A strong negative correlation can be observed between Ca and MS, Al, Fe, K, Si and Ti – also indicated in bolt on table 7 below.

PCC	Al	Ba	Ca	Cr	Cu	Fe	K	MS	Mg	Mn	P	Pb	S	Si	Sr	Ti	V
Ba	0.34																
Ca	**-0.84**	-0.26															
Cr	0.70	0.19	-0.78														
Cu	-0.35	-0.11	0.44	-0.36													
Fe	**0.86**	0.24	**-0.86**	0.66	-0.27												
K	**0.97**	0.32	**-0.93**	0.74	-0.41	**0.89**											
MS	**0.92**	0.33	**-0.90**	0.73	-0.41	**0.94**	**0.95**										
Mg	0.27	-0.19	-0.03	0.03	0.33	0.23	0.16	0.11									
Mn	-0.44	-0.02	0.43	-0.22	-0.04	-0.54	-0.44	-0.40	-0.43								
P	0.65	0.44	-0.65	0.62	-0.36	0.59	0.68	0.66	0.06	-0.21							
Pb	-0.45	-0.07	0.56	-0.41	0.28	-0.47	-0.49	-0.47	-0.06	0.46	-0.33						
S	0.61	0.28	-0.54	0.43	0.01	0.52	0.59	0.53	0.37	-0.42	0.47	-0.39					
Si	**0.83**	0.26	**-1.00**	0.78	-0.44	**0.85**	**0.92**	**0.89**	0.01	-0.42	0.65	-0.56	0.53				
Sr	-0.15	-0.01	0.36	-0.32	0.31	-0.23	-0.25	-0.23	-0.11	0.33	-0.44	0.30	0.03	-0.37			
Ti	**0.97**	0.34	**-0.88**	0.72	-0.36	**0.86**	**0.97**	**0.92**	0.26	-0.47	0.66	-0.49	0.67	**0.87**	-0.23		
V	0.64	0.14	-0.47	0.30	-0.13	0.60	0.60	0.55	0.54	-0.57	0.41	-0.16	0.52	0.46	-0.20	0.64	
Zn	-0.34	0.05	0.36	-0.39	0.36	-0.29	-0.35	-0.32	-0.24	0.42	-0.39	0.34	-0.15	-0.36	0.49	-0.34	-0.37

Table 7: Pearson correlation matrix with the PCC for MS and most abundant geochemical elements. PCC > 0.80 in bold.

5.3.2. Scree Plot

The Scree plot graphically summarizes how much of the variance is accounted for by each new Principal Component (PC), denoted as Comp.1 tot Comp.18 on Fig. 42. Or conversely, the cumulative eigenvalue curve (or cumulative variability) indicates how many components should be taken into account in order to account for that certain percentage of variance.

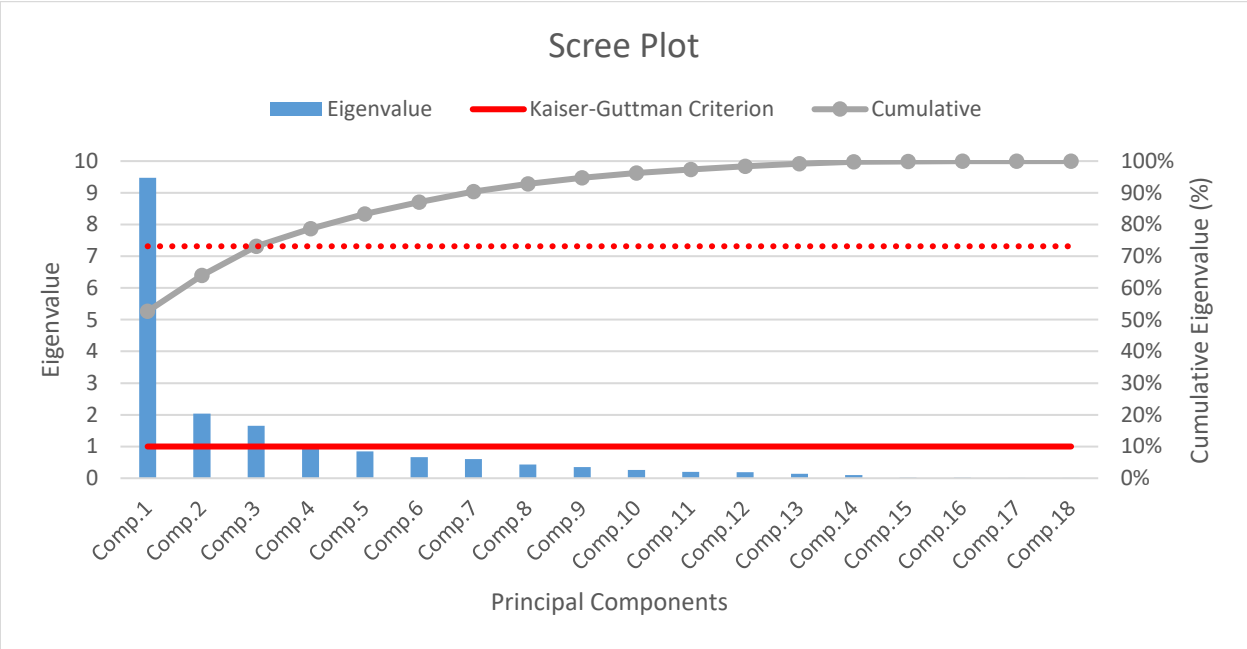

Figure 42: Scree plot, with Eigenvalues, cumulative eigenvalues as well as Kaiser-Guttman Criterion (bold red line) and cumulative variance accounted for by PC1 to PC3 (dotted red line).

Based on the Kaiser-Guttman Criterion, all components with eigenvalues equal to 1 or higher should be taken into account for the PCA. Eigenvalues below 1 on the other hand do not provide more information than the original variable and are of no added value to the PCA (Bro and Smilde 2014; Elskens, 2019). As indicated by the bold red line on Fig. 42, PC1, PC2 and PC3 have eigenvalues greater than one and account for 53%, 11% and 9% of the variability respectively. A 3D-projection of the data on the PC1, PC2 and PC3 axes accounts for 73% of the total variability and 27% represents background noise (see appendix 11.3).

5.3.3. Loading Plot

All low-resolution geochemical data and MS values were transformed towards their z-values for centralization of the data (mean = 0 and standard deviation = 1). Because some of the distributions were considerably skewed, both log-transformation and box-cox transformation for improved normal distribution were assessed but were of no added value. Therefore, raw data was only transformed towards their z-values before calculating the eigenvalues and eigenvectors. Even though 3D PCA Loading plots are available, graphical representation thereof is more complex. Also, since most important information is summarized by PC1 and PC2 (together accounting for 64% of the variance), a 2D PCA Loading plot was constructed (Fig. 43).

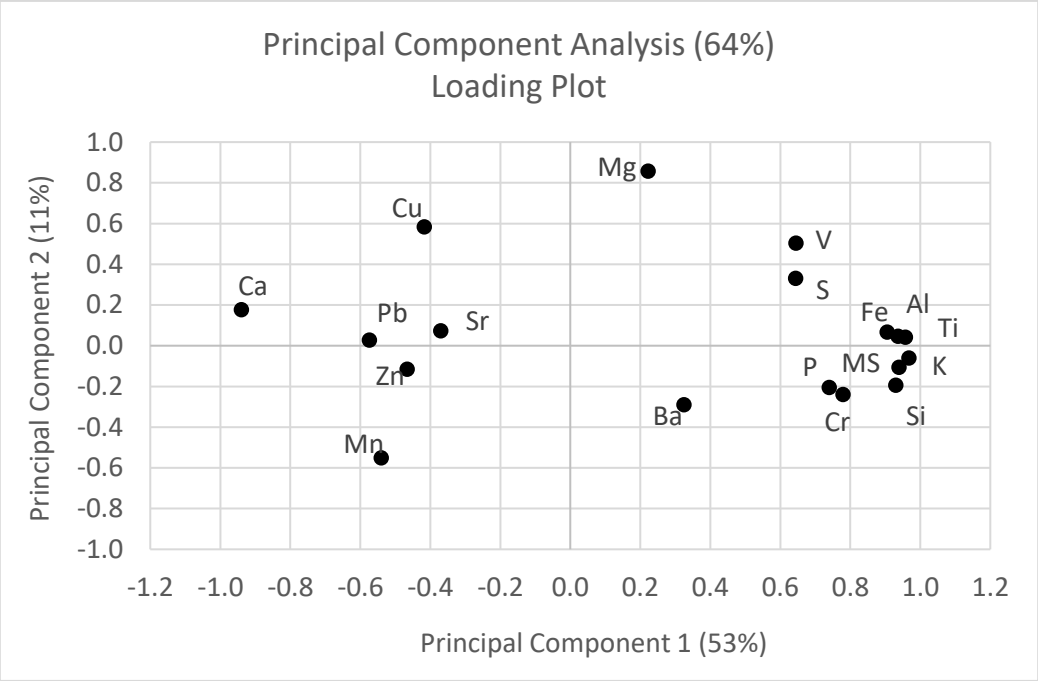

Figure 43: 2D PCA Loading plot based on PC1 and PC2.

Elements [MS, Ti, Al, K, Fe, Si] are clustered together, as are [V,S], [P,Cr] and [Pb, Zn, Sr]. Elements such as Mg, Cu, Ba and Mn do not show any clustering in the 2D PC1-PC2 space. Some of the correlations summarized in the Pearson correlation matrix (Table 7) are elegantly visualized by the 2D PCA Loading plot, such as the strong negative correlation between [Ca] and [MS, Ti, Al, K, Fe, Si].

Summarizing some key observations of the 2D PCA Loading plot in PC1-PC3 space for completeness; clustering of [MS, Ti, Al, K, Fe, Si], [Zn,Sr], [P,Cr] as well as [Pb,Mn]. Finally, shortly summarizing some key observations of the 2D PCA Loading plot in PC2-PC3 space; clustering of [Pb,Al,Ti,Fe], [MS,K], [P,Cr,Si]. See appendix 11.3 for additional graphical representations. A PCA was also carried out on the 5 cm-high resolution dataset (which can be found in the appendix 11.3), ranging from 11.75 m to 34.50 m for all geochemical elements. Observations for the high-resolution geochemical dataset are consistent with what is observed for the low resolution dataset. The correlations revealed by the Pearson correlation matrix and the PCA will often be used in the next chapter (Chapter 5.4), where all high-resolution results are summarized.

5.4. High Resolution Dataset

A large part of the Hallembaye section, ranging from 11.75 m to 34.50 m, has been analyzed at a 5 cm-high resolution using µXRF, with the specific purpose of gaining insight in short-term (10^4 – 10^5 kyr) changes throughout the profile. Also, for a small part of the section (18.45 m – 22.45 m), sufficient powdered chalk sample was available to carry out 5 cm-high-resolution MS measurements. Even though the 5 cm-high resolution MS dataset is not large enough to be used for cyclostratigraphy, it's potential to do so will be addressed briefly before focusing on the extensive high resolution geochemical dataset.

5.4.1. MS and Geochemistry – High Resolution

Table 8 shows the Pearson correlation matrix, PPCs for selected elements Ca and Si, terrigenous elements Al, K and Ti and finally Fe and MS. All p-values for significance are lower than 0.0001 (< 0.05).

PCC	Al	Ca	Fe	K	MS	Si
Ca	-0.55					
Fe	0.64	-0.64				
K	**0.88**	-0.74	0.69			
MS	0.75	-0.65	**0.93**	0.78		
Si	0.53	**-1.00**	0.62	0.72	0.63	
Ti	0.68	-0.54	0.47	0.73	0.56	0.52

Table 8: Pearson correlation matrix for Hallembaye high resolution dataset with the Pearson Correlation Coefficients (PPC) for selected elements and MS (18.45 m – 22.45 m). PCC < 0.80 in bold.

Also at high sample resolution, the MS signal strongly correlates positively with Fe (indicated in bold in Table 8), similar to what was observed for the low-resolution dataset. Furthermore, significant positive correlation is also observed between MS and Al, K, Ti as well as Si. Finally, a significant negative correlation exists between the MS signal and Ca.

Even though MS correlates positively with Si, Fe and the terrigenous elements Al, K and Ti, small differences can be observed when assessing high resolution data (see Fig. 44). In correspondence with the strength of correlation between MS and Fe, it can be observed in Fig. 44 that both undergo similar changes throughout the section. The MS signal gradually decreases from roughly 6 10^{-9} m^3/kg to 2 10^{-9} m^3/kg, albeit with superimposed fluctuations. Similarly, Si, Fe, Ti, Al and K display similar gradual decreasing trend with superimposed fluctuations.

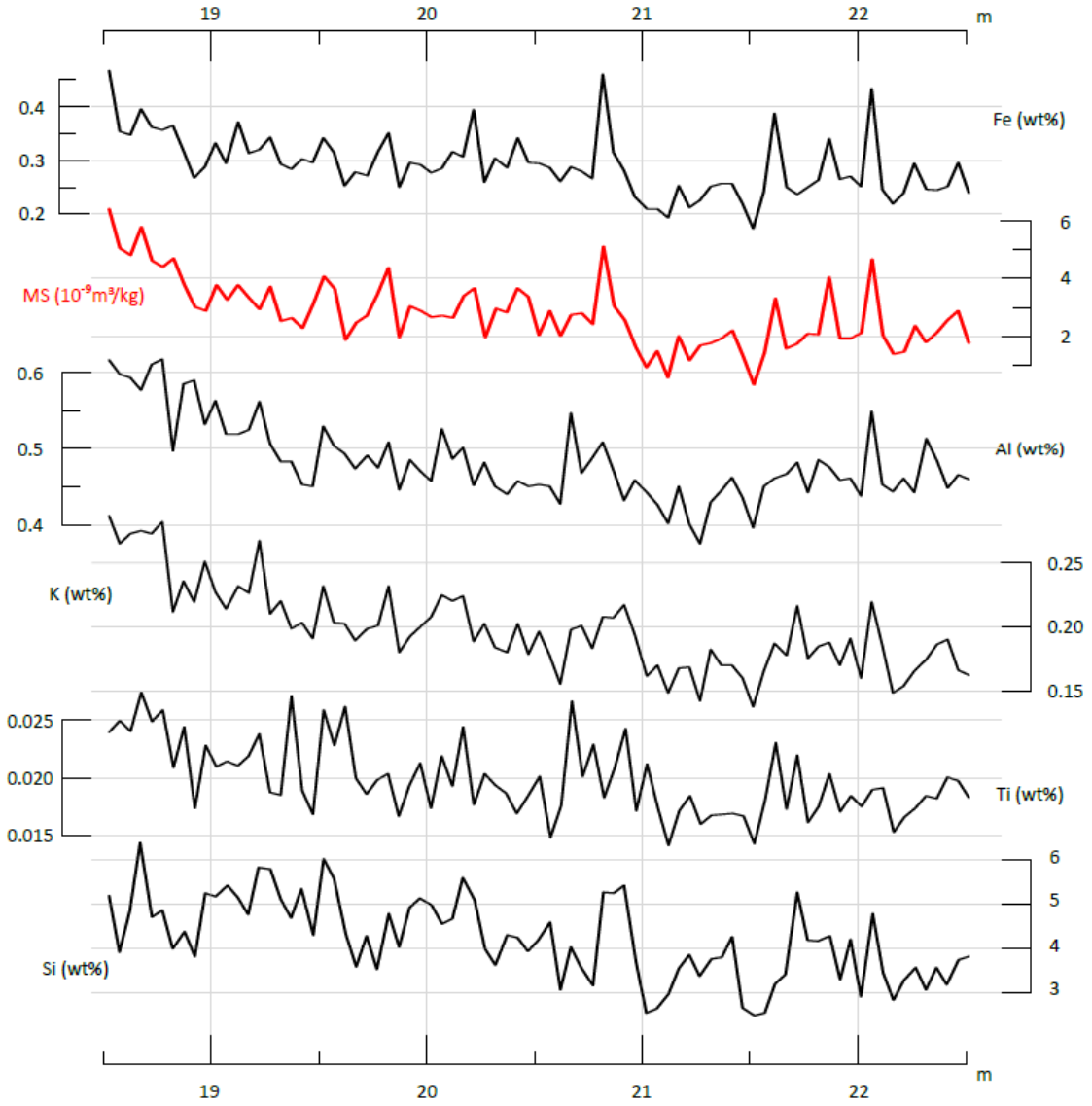

Figure 44: MS (red) and selected element concentrations (black) at 5 cm-high resolution from the 18.50 m to 22.45 m interval.

5.4.2. Elemental Geochemistry – High Resolution

High resolution geochemical elemental data not only provides important insight in the composition of the Vijlen and part of the Lixhe 1 Member chalk, but also forms the backbone of the application of cyclostratigraphy in this master thesis. Therefore, this part of the dataset is treated in more detail, separated from any MS or low-resolution data.

Element	Min	Max	Mean
Al (wt%)	0.27	0.68	0.46
Ba (ppm)	0.00	185.03	43.68
Ca (wt%)	13.06	37.56	31.75
Cr (ppm)	0.24	16.90	8.51
Cu (ppm)	1.81	16.57	7.30
Fe (wt%)	0.11	0.85	0.30
K (wt%)	0.065	0.33	0.18
Mg (wt%)	0.10	0.27	0.19
Mn (wt%)	0.015	0.025	0.019
P (wt%)	0.60	2.18	0.84
Pb (ppm)	4.77	15.13	9.62
S (wt%)	0.044	0.089	0.067
Si (wt%)	1.08	12.66	3.70
Sr (ppm)	579	1017	786
Ti (wt%)	0.009	0.034	0.019
V (ppm)	0.00	5.32	2.29
Zn (ppm)	25.01	46.08	35.12

Table 9 Element geochemistry high resolution data set summary of 11.75 to 34.50 m of selected elements.

Table 9 summarizes the main values of interest of selected elements for the high-resolution interval from 11.75 to 34.50 m (note some trace elements are expressed in ppm rather than wt%). Most notable is the large variation of Ca in this interval, with lowest values (13.06 wt%) found at the Froidmont Horizon (11.75 m), after which it slightly increases (represented by $CaCO_3$ on Fig. 41).

In the following subchapters, focus is put on specific elements that could be of interest for the application of cyclostratigraphy. Whilst concentrations remain important, most attention will be paid to the relative variations within the signals, observed trends and visually observable cycles. It is also for this reason that from this point onwards, elements are treated as such – knowing they provide the same information as their corresponding oxides as far as signal variation is concerned.

5.4.2.1. Bulk Matrix Elements – Silicium and Calcium

When looking at the evolution of Ca and Si along the stratigraphic column at higher resolution (Fig. 45), again a mirror-like relationship is revealed between these two elements. These elements display a significant, strong negative correlation (R^2 = 0.9981, p-value = 0 < 0.05) for the stratigraphic interval ranging from 11.75 m to 34.50 m. Overall, a gradual decrease of the amount of elemental Si can be observed, matched by an increase of elemental Ca. Along the interval of 11.75 m to 34.50 m, Si concentrations vary from 1.08 wt% to 12.66 wt% and Ca concentrations vary from 13.06 wt% to 37.56 wt%. Furthermore, the record can be subdivided based on changes in baseline sloping. From about 12 m to 28 m, a strongly fluctuating Si signal is superimposed on a decreasing trend. From 28 m onwards, a more monotonous Si signal is superimposed on a flat baseline – with the exception of a clear drop in Si-concentrations around 30 m.

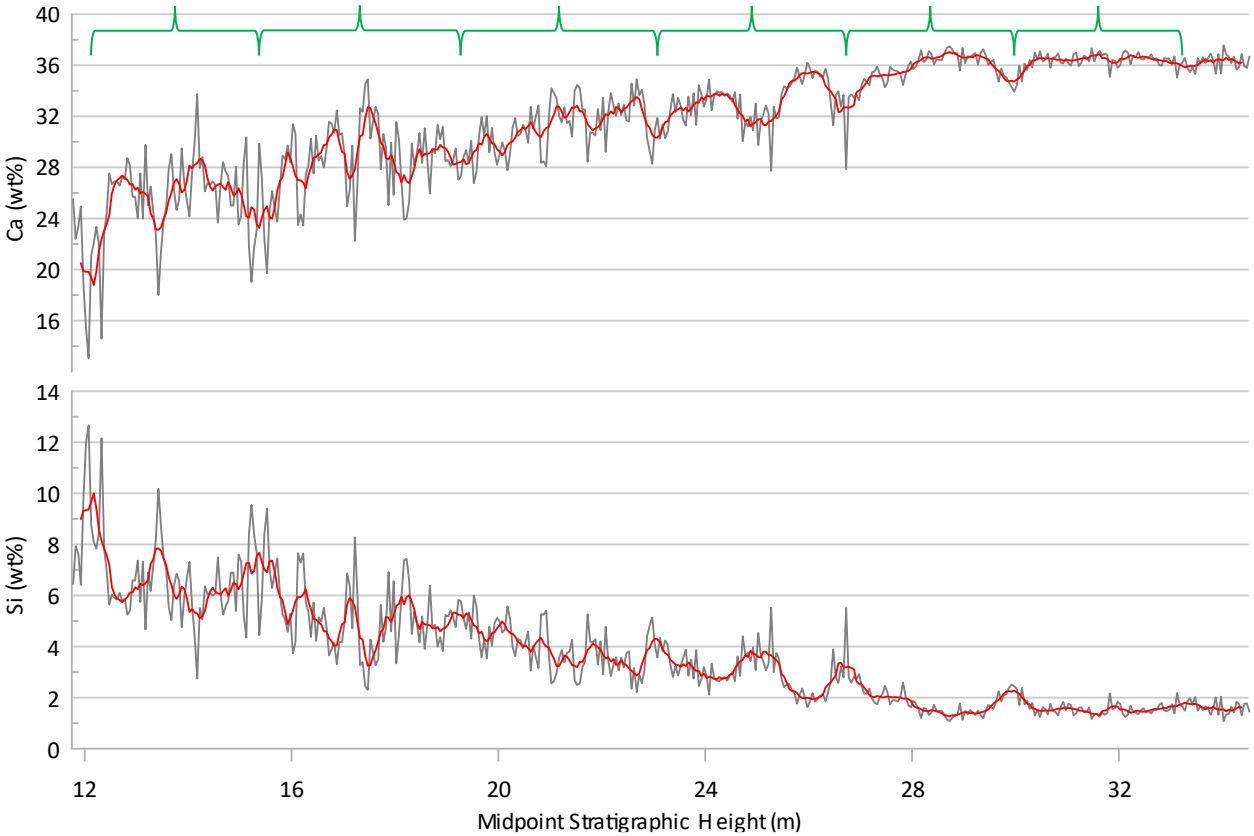

Figure 45: Element concentration graph for Calcium and Silicium (black line) and running averaged over 7 datapoints (red line). Green accolades indicating potential cycles based on visual inspection.

Variations in the fluctuation amplitudes can be used to further subdivide the section; from about 12 to 18 m (larger amplitude variations of 2 wt% to 7 wt%), from 18 m to about 22 m (smaller amplitudes of 0.5 wt% to 2.5 wt%) and from 22 m to 28 m (larger amplitudes of 2.5 wt% to 4 wt%). From 28 m to 34 m only one major peak can be observed in the Ca and Si signals at 30 m height, after which the Ca and Si signals remain seemingly stable. Based on visual observations of the 7 running averaged Ca signal, 6 cycles of 3 to 4 m can identified, arbitrarily located based on local minima in the Ca signal (green accolades on Fig. 45).

5.4.2.2. Magnesium, Strontium and Barium

As described in Chapter 2.1., Mg, Sr and Ba often occur as the positive counter-ion to CO_3^{2-} in the calcite mineral. For this reason, it is worth looking at how the concentrations of these elements evolve from a stratigraphic height of 11.75 m to 34.50 m compared to the Ca signal (Fig. 46).

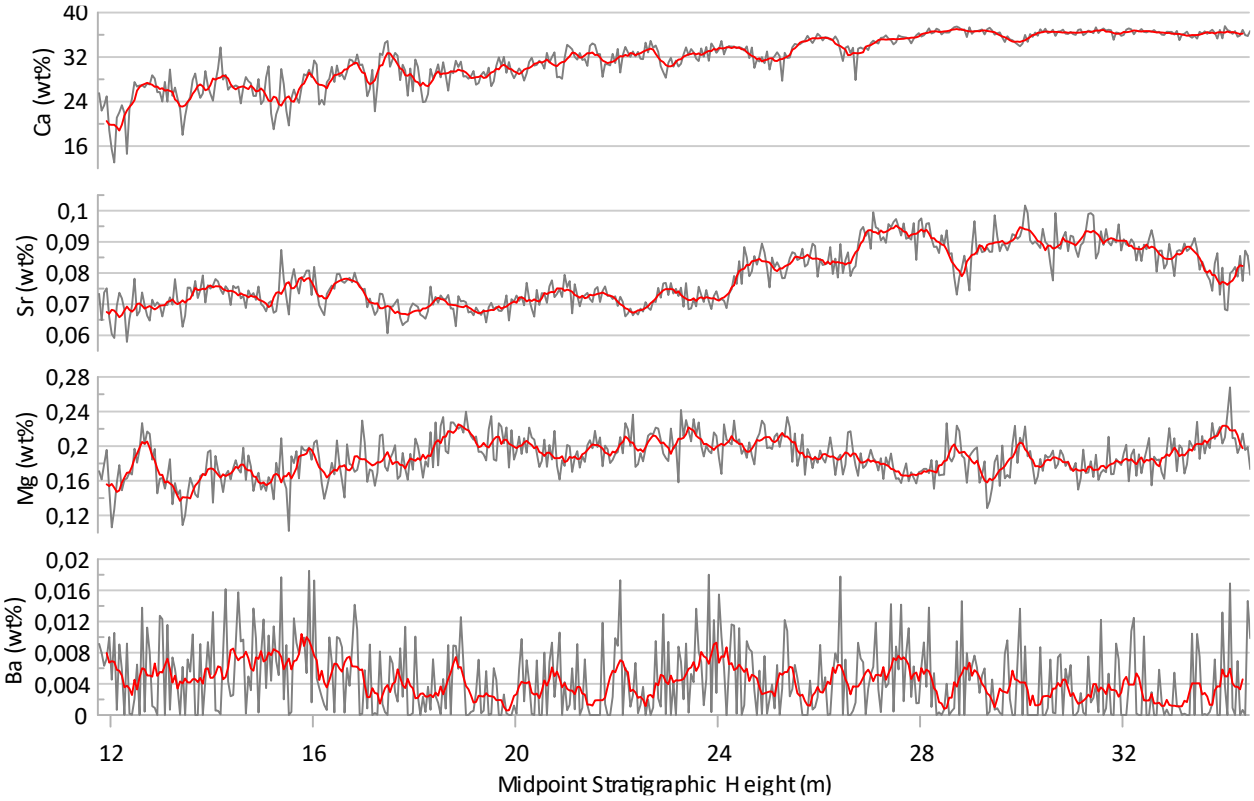

Figure 46: Element concentration graph for Mg, Sr, Ba and Ca (black line) and running averaged over 7 datapoints (red line).

Elemental concentrations for Ba remain well below 0.02 wt% along the complete profile and average at about 0.004 wt% - remaining undetected for about 20 % of all samples in the interval 11.75 m to 34.50 m (91 out of 456 datapoints). Sr concentrations average at about 0.08 wt% throughout the profile, however, at about 24 meter an apparent shift in the Sr baseline occurs towards slightly higher values. Mg is present at higher concentrations, averaging at about 0.19 wt%, and does display a large amount of short-scale fluctuations superimposed on larger-scale fluctuations along the stratigraphic range. Whereas Ba and Mg seem to display some similarities in overall trends and correspondence between signal peak maxima and minima, Sr and Ca display completely different stratigraphic variation.

5.4.2.3. Aluminium, Potassium, Titanium and Iron

Changes in the chalk content can in part be attributed by changes in terrigenous input, exemplified by elements Al, K and Ti of Fig. 47. Additionally, Fe was added as well based on previous observations made via the Pearson Correlation matrix and PCA. Significant correlation between terrigenous elements Al and K ($R^2 = 0.8499$ and p-value = $4.36E^{-189} < 0.05$), Al and Ti ($R^2 = 0.7727$ and p-value = $3.72E^{-148} < 0.05$) and K and Ti ($R^2 = 0.7801$ and p-value = $2.13E^{-151} < 0.05$) is confirmed.

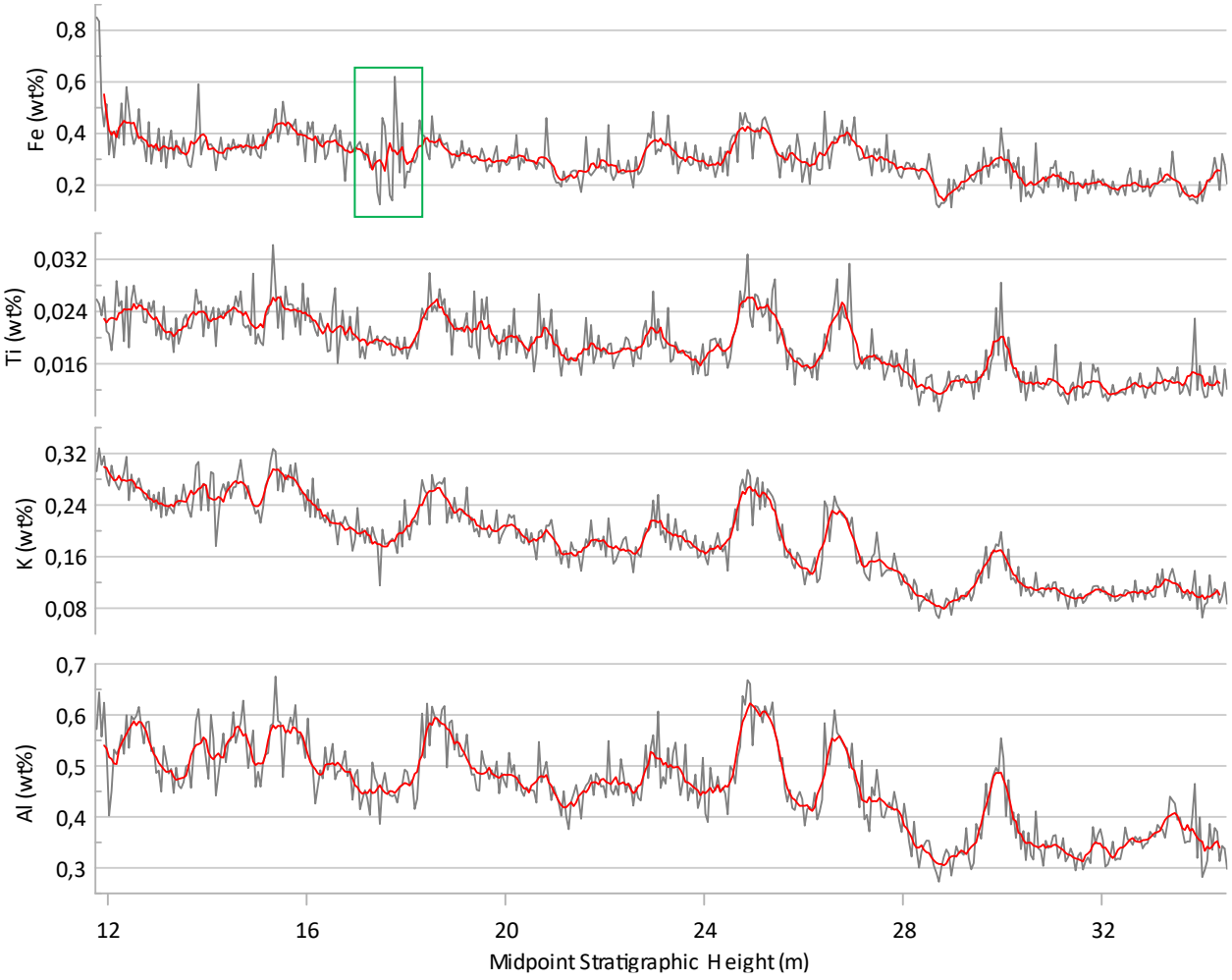

Figure 47: Element concentration graph for Fe, Ti, K and Al (black line) and running averaged over 7 datapoints (red line). Discrepancy in Fe signal compared to other elements marked in green.

Aside from some minor differences observed in the 7 running averages from 11.75 m to 14.00 m, Al, K, Ti and Fe display very similar patterns throughout the high-resolution interval up to 34.50 m. From 17 m to 18 m however, a discrepancy can be observed in the Fe signal, characterized by very strong fluctuations of 0.4 wt%, compared to the terrigenous elements Al, K and Ti (as indicated in green on Fig. 47).

5.4.2.4. Calcium and Potassium

The earlier observed gradual increase in Ca at higher stratigraphic heights can potentially be attributed to a decrease in terrestrial influx. Therefore, it is valuable to assess the evolution of the Ca signal and one of the terrigenous elements, K in this case. A significant negative correlation can be observed between Ca and K (R^2 = 0.7176, p-value = $9.96E^{-127}$ < 0.05). Other elements such as Al and Ti display the same stratigraphic variation as K, however, their correlation with Ca is less strong yet still significant (R^2 = 0.4248, p-value $1.7493E^{-56}$ = < 0.05 and R^2 = 0.4602 , p-value = $9.1886E^{-63}$ < 0.05 respectively).

Figure 48: Element concentration graph for Ca and K (black line), running averaged over 7 datapoints (red line) and phase shifts (green lines).

Moreover, phase shifts can be observed between Ca and K at different heights (see green lines on Fig. 48) at the lower part of the interval (13.5 m to 15.2 m). From about 15.2 m to 18.2 m, K and Ca display similar phase. From 19.2 m onwards, both element signals are out of phase, with maxima in K corresponding to minima in Ca. Similar to what was observed for Si, K and other terrigenous elements (Ti, Al as well as Fe) display a decreasing trend from 11.75 m to roughly 28.00 m (Lixhe Horizon) with superimposed fluctuations. From 28.00 m onwards, the overall baseline of K seems to flatten out and the superimposed fluctuations that are observed are smaller as well (aside from a large peak around 30 m).

6. Cyclostratigraphy

Cyclostratigraphy has the potential to construct age models, using a variety of analytical techniques of high-resolution geochemical datasets. The possibility exists that astronomical forcing of the paleoclimate is recorded differently in specific proxies – or may even be completely absent or erased through processes of diagenesis. Firstly, cyclostratigraphy will be applied based on the calcium carbonate content of the chalk – which can potentially be linked to a preliminary age model by Zijlstra (1994) based on lithological observations. Secondly, the potential climate-induced change in input of terrigenous material is assessed by analyzing the K signal. Lastly, the Ti/Al ratio, believed to be less prone to diagenesis is investigated in analogy with work carried out by Govin et al. (2012) and Engelke et al. (2018). According to Govin et al. (2012) and references therein, Ti/Al can be linked to grain size changes – with Ti being enriched in coarser sediments and Al begin associated to finer material - which can be exploited to distinguish eolian (Al) versus fluvial (Ti) supply (Govin et al., 2012). Given their low concentration in carbonate sediments, terrigenous proxies should in first instance be used to assess fluctuations in provenance (Engelke et al., 2018).

6.1. Silicium and Calcium

Ca and Si are the most abundant elements present in the geochemical record, which is representative of what can be observed in the lithology of the Kreco quarry. As described in Chapter 2.2., changes in the paleoclimate and paleoenvironment might affect bio productivity (calcareous organisms versus siliceous organisms). Provided the change in Ca and Si is due to astronomical forcing of the paleoclimate and the primary signal was not heavily altered by diagenesis, either of these elements is a great candidate for the application of cyclostratigraphy. Additionally, the use of geochemical elements representing the lithology might provide much needed analogy with work carried out primarily by Zijlstra (1994) who made cyclostratigraphic interpretations based on flint layers occurring throughout the chalk. In this chapter, results of a cyclostratigraphic approach are demonstrated on the geochemical elements Si and Ca.

6.1.1. MTM Power Spectrum – Si and Ca

MTM was applied on the exponentially detrended Si and Ca signal, transforming the data from the spatial domain (stratigraphic height, expressed in m) to the frequency domain (expressed in cycles/m) (Fig. 49).

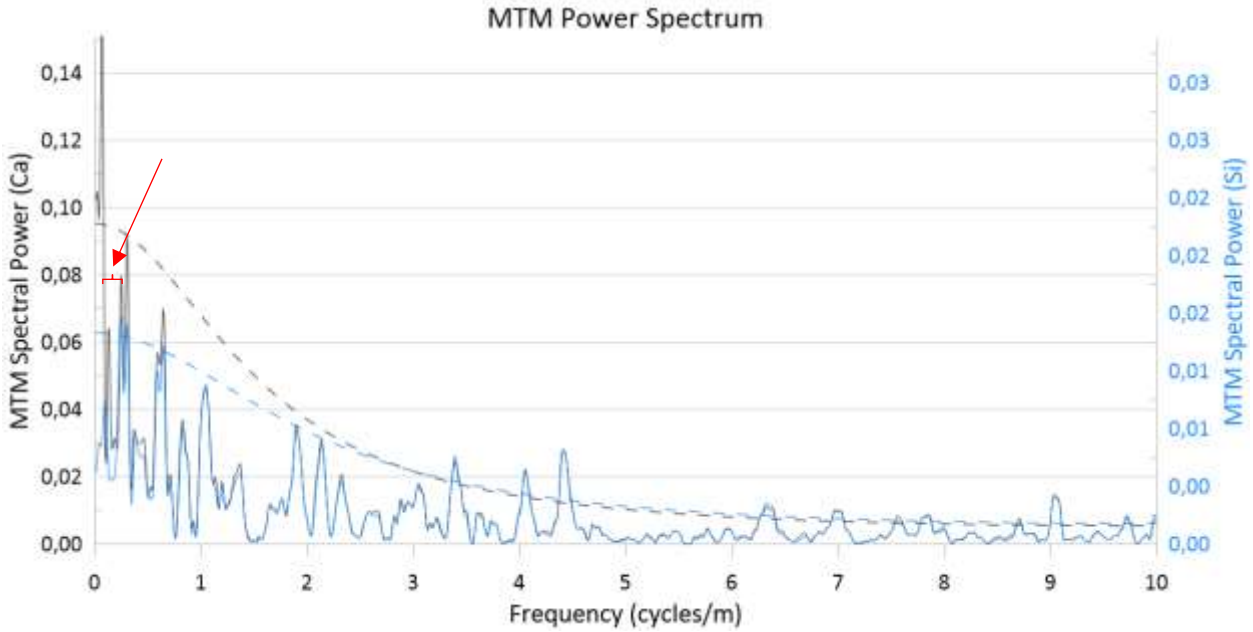

Figure 49: MTM for Ca (black) and Si (blue) and AR1 (95%) confidence levels, red accolade and arrow indicate potential range for small differences in spectral power.

The power spectrum of Si and Ca are very similar (Fig. 49). Especially at higher frequencies (1 to 10 cycles/m) there is a complete overlap of the spectral components (albeit at a lower magnitude for Si due to its lower concentration and thus smaller relative fluctuations in the depth domain signal). At lower frequencies, especially below 1 cycle/m, small relative differences in magnitude arise between the Si and Ca spectral components. Even though the majority of the peaks are of lower significance when looking at the AR1 (95%), they are not necessarily negligible altogether. If for some reason, certain cyclical components have slight changes in frequency, they will consequently occur as a separate peak (e.g. group of peaks from 1.7 to 2.3 cycles/m) and might give rise to lower spectral power and hence appear less important and significant.

As mentioned in Chapter 4.4.2., exponential detrending might introduce new trends that would lead most likely to low-frequency signals corresponding to 6 to 8 m long cycles (or spectral power at frequencies 0.167 to 0.125 cycles/m respectively). Therefore, special care is taken when interpreting low frequency components during spectral analysis.

Given that the MTM power spectra of Si and Ca are (nearly) identical, focus will be put on Si only for the next steps of the spectral analysis as described in following chapters. Si was preferred over Ca because, in absolute terms, a lesser degree of exponential detrending was required for the Si signal.

6.1.2. Evolutive Harmonic Analysis - Silicium

Evolutive Harmonic Analysis based on the MTM of Si was carried out using a window size of 4 m and a step size of 0.05 m, spatially resolving spectral components as illustrated on Fig. 50. High spectral power (amplitude) can be observed at multiple frequencies ranging from 0 to 5 cycles/m as well as around 6.3 cycles/m for the lower part of the interval (14 m to 19 m). At higher stratigraphic heights, spectral power decreases especially for the high-frequency components

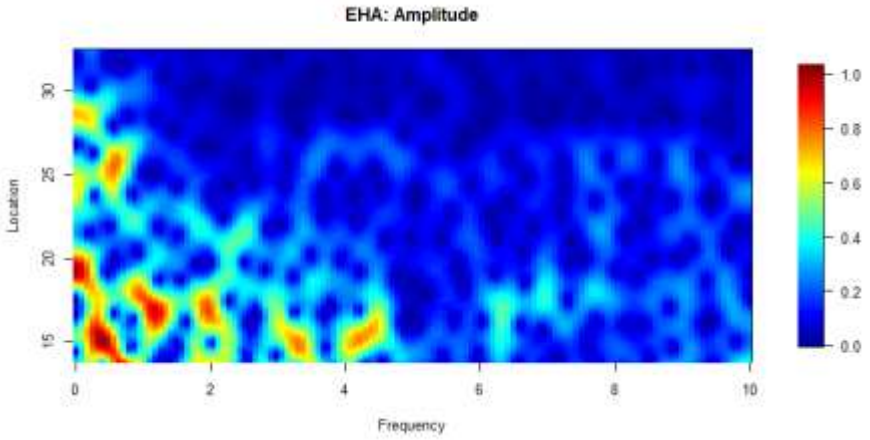

Figure 50: EHA of exponentially detrended Si, revealing spectral power (expressed by the amplitude) in function of frequency (cycles/m) and stratigraphic height (m).

By normalizing the highest spectral component to unity per window, normalized amplitudes are obtained as visualized on Fig. 51. This way, spectral components with lower amplitudes at higher stratigraphic intervals are less impacted by stronger amplitudes at lower stratigraphic intervals. Although conclusions made about spectral power in Fig. 50 are to be kept in mind, this way a more detailed view is obtained about which cyclical components are present in the record at all heights.

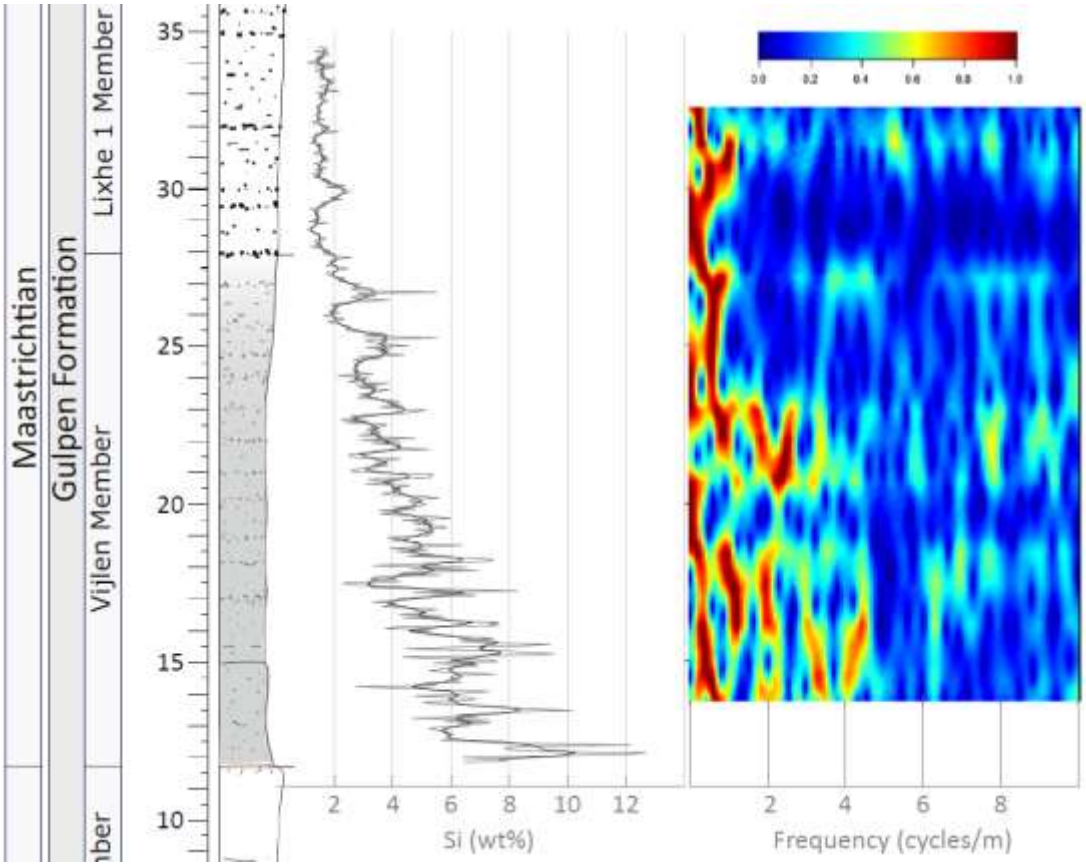

Figure 51: Graphical representation of the Kreco quarry lithostratigraphy (Vellekoop et al., In prep.) with Si (grey, wt%) and 5 running average Si (black, wt%) as well as normalized EHA of Si.

Fluctuations with higher amplitude can be observed in the Si signal on Fig. 51 for the lower part of the interval, ranging from 11.75 m to roughly 23.00 m. From 23.00 m onwards, less fluctuations are observed and their amplitudes are lower compared to the lower part of the interval. The amplitude-normalized EHA on the right of Fig. 51 confirms these visual observations and reveals spectral power (expressed as normalized amplitude) at certain frequencies; around 4 cycles/m, around 2 cycles/m and a low frequency component around 1 cycle/m. At even lower frequency (< 0.5 cycles/m) spectral power is also high, but as mentioned in the previous chapter, this might be due to artificial trends induced during detrending and these should be carefully interpreted. From 23.00 m onwards, only around 0.8 to 1 cycles/m spectral power is high.

To summarize; while the lower part of the interval is characterized by a strongly decreasing amount of Si characterized by high and low frequency cyclicity, the upper part is characterized by a slowly decreasing to stagnating amount of Si characterized only by low-frequency cyclicity. Presence of potential cycles as revealed by spectral power at key frequencies by the EHA and MTM periodogram will be used as the basis for the construction of several bandpass filters as described in the following chapter.

6.1.3. Bandpass Filtering – Silicium

Four bandpass filters were designed based on key frequency ranges revealed by MTM periodogram and EHA (Fig. 52). The low frequency bandpass filter (0.11 – 0.35 cycles/m) highlights large underlying trends in the Si data series, which differ considerably; from 12 m to 21 m, the amplitude is more strongly modulated; the interval from 21 m to 28 m is covered by one cycle with very low amplitude modulation; from 28 m onwards, bandpass filter cycle length again compares to the cycle length observed for the 12 m to 21 m interval, albeit with a slightly lower amplitude modulation.

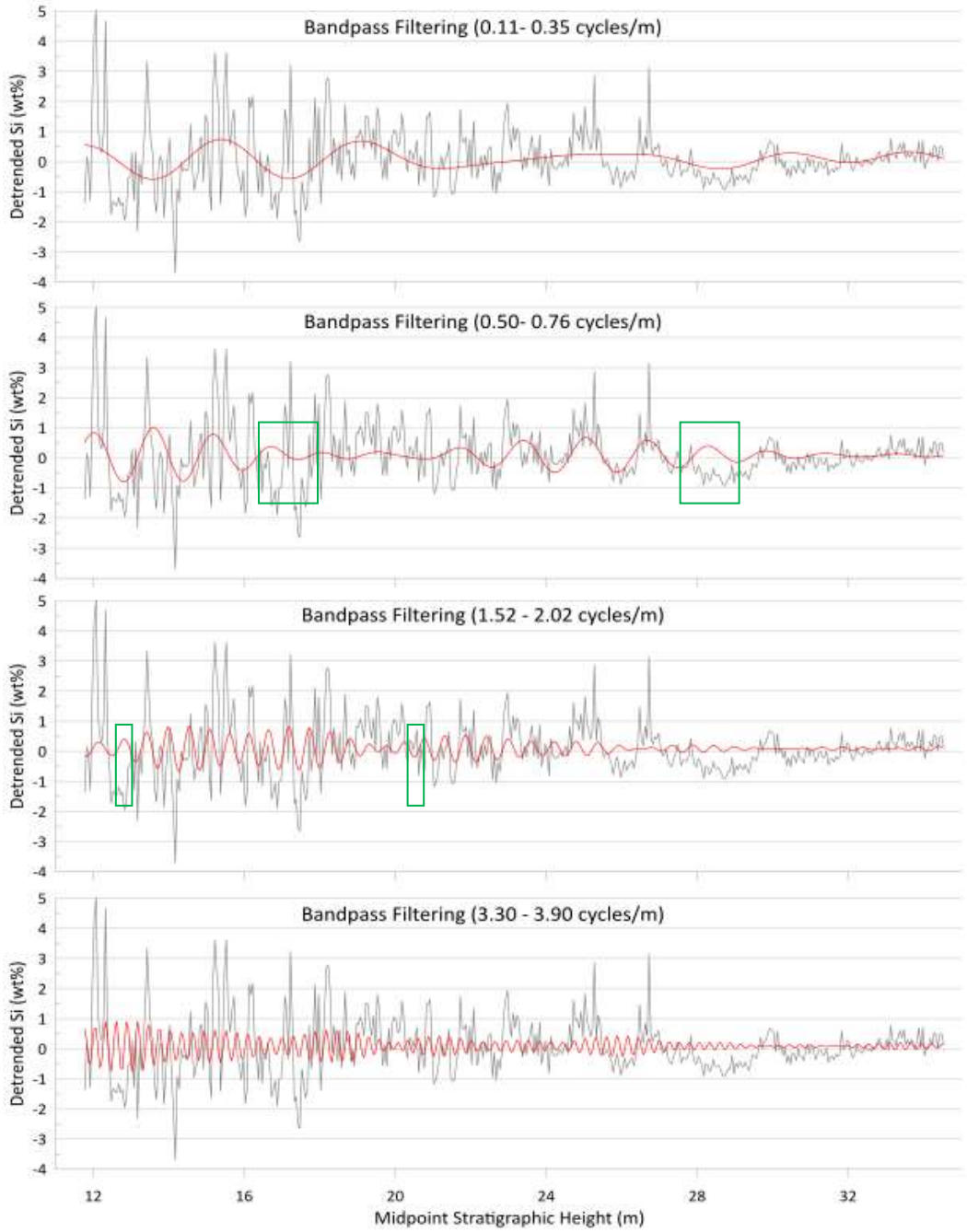

Figure 52: Bandpass filtering based on revealed spectral components of the Si data series, phase shifts indicated in green.

Bandpass filter based on a frequency range of 0.50 – 0.76 cycles/m, matches the overall Si profile well, except for a clear phase shift at 18 m as well as 28 m indicated in green on Fig. 52. Bandpass filter (1.52 – 2.02 cycles/m) overlaps well with the entire Si profile from 11.75 m to 34.50 m, expect for 2 small phase shifts highlighted in green of Fig. 52 around 13 m and 21 m. Lastly, the high frequency bandpass filter matches the overall Si signal quite well.

Based on the bandpass filters at average frequencies 3.6 cycles/m, 1.8 cycles/m and 0.6 cycles/m, period-pair ratio fitting reveals a 6:2:1 relationship in the depth domain respectively, reminding of the precession-obliquity-short eccentricity ratio. However, given the observed phase shifts as well as some stretching of the bandpass filter signal, interpretation of the observed ratios at this point should be made with care.

6.1.4. TimeOpt – Silicium

In order to construct a floating age model based on the Kreco quarry lithology represented by elemental Si and Ca composition, independent estimation of the sedimentation rate is required. Once the average sedimentation rate is determined, the depth domain record can be transformed into a preliminary time domain record.

Even though MTM periodogram peak ratio comparison with Milankovitch cycle ratio-pairs is an option to estimate the length of certain cycles and therefore also the average sedimentation rate, presence of a large amount of peaks in MTM periodogram complicates this process. Implications of using Milankovitch cycle ratio-pairs should also be considered as addressed in Chapter 2.3.5. In addition, EHA revealed changes in dominant cyclicity along the profile which might be indicative of changes in sedimentation rate. Therefore, a nominal TimeOpt is carried out, assuming that Milankovitch cyclicity is present in the record for the estimation of the average sedimentation rate. Assessment of the precession amplitude modulation by the eccentricity is carried out using precession (23.2 kyr and 18.7 kyr) and eccentricity (405 kyr, 125 kyr and 95 kyr) targets. In case of changing sedimentation rates or presence of hiatuses, the nominal TimeOpt is not able to provide a satisfying fit (see Chapter 4.4.7.). However, it might provide preliminary indications what orders of magnitude in sedimentation rate to expect.

Initial testing of the average sedimentation range was carried out for a broad sedimentation range from 1 cm/kyr to 10 cm/kyr, evaluating 1000 sedimentation rates. For full signal recovery, the maximum sedimentation rate was automatically reset to 5.6 cm/kyr when using the aforementioned targets. This value represents a technical limit and is an implication of the used targets. In case eccentricity modulated precession would be present in the record, average sedimentation rates are to be below 5.6 cm/kyr in order for the TimeOpt analysis to function. In a second step, maximum sedimentation rate input parameters were changed to 3.3 cm/kyr based on r^2-values for the envelope and power fit profiles (Fig. 53). Similar orders of magnitude in sedimentation rate(s) were reported by Vellekoop et al (in prep.) for the Vijlen and Lixhe Members, based on the integration of bio- and carbon isotope stratigraphy.

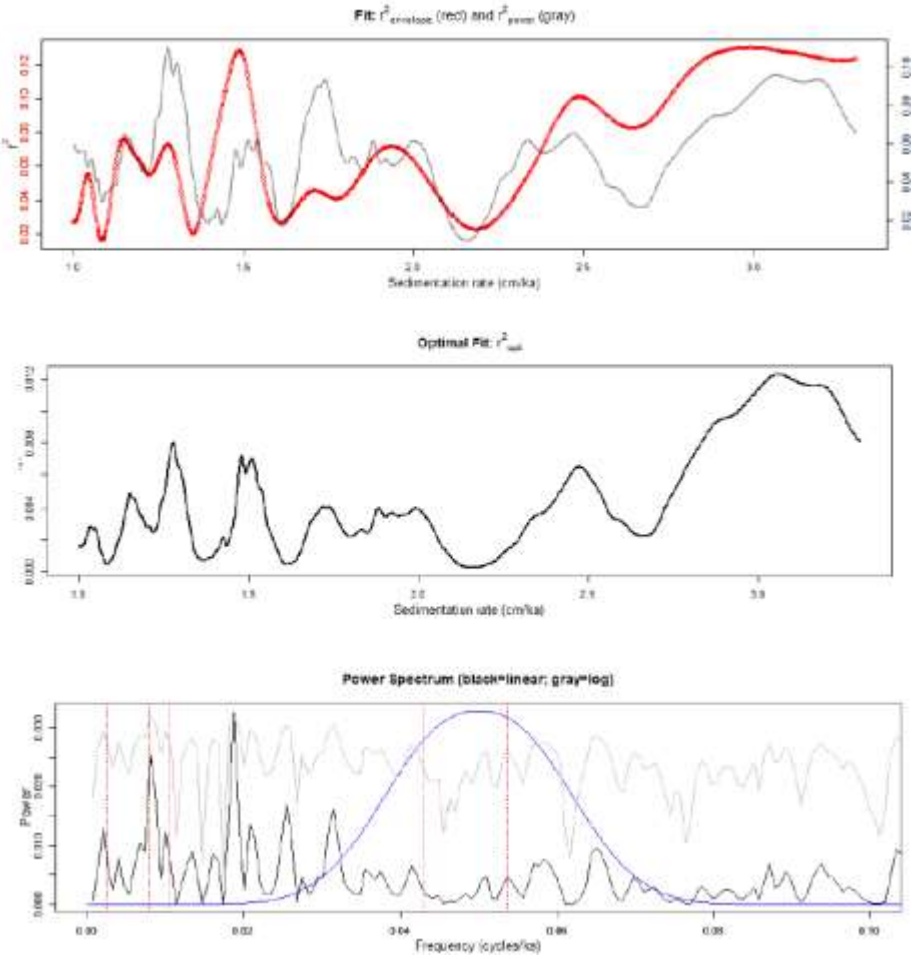

Figure 53: TimeOpt of Si signal. Top: r^2(envelope) and r^2(power) value. Middle: Optimal r^2 of the fit. Bottom: Power spectrum with linear power in function of frequency (cycles/kyr), red lines indicative of precession and eccentricity targets.

TimeOpt results yield maximum r^2-value for spectral power of 0.11 at a sedimentation rate of 1.28 cm/kyr, maximum r^2-value for envelope of 0.13 at a sedimentation rate of 2.98 cm/kyr and finally an optimal r^2-value of only 0.01 at a sedimentation rate of 3.06 cm/kyr. Low r^2-values as well as a sub-optimal fit of the precession and eccentricity targets with the concentration of spectral power in the power spectrum reveal the obtained average sedimentation rate is not representative for the complete record. Alternatively, absence of precession amplitude by modulation in the actual signal might also lead to poor fitting and r^2-values. Similar results are obtained when evaluating short eccentricity amplitude modulation and do not provide any additional insight. When looking closer at the top and middle plot of Fig. 53, r^2-values seem to peak at several sedimentation rates, which could be indicative of changing sedimentation rates throughout the record, which might also explain why TimeOpt is not able to provide an optimal fit. Therefore, an evolutive method of TimeOpt (eTimeOpt) will be applied in the next chapter to assess potential changes in sedimentation rate throughout the record.

6.1.5. eTimeOpt – Silicium

Evolutive TimeOpt of the silicium record is carried out to obtain spatially resolved insight in the sedimentation rate change along the stratigraphic range from 11.75 m to 34.50 m. By using a sliding window, the eTimeOpt is carried out using similar parameters to TimeOpt (Fig. 54). Fitting according to the envelope, illustrated by $r^2_{envelope}$, does not reveal much clear insight in the sedimentation rate. Fitting according to the power, illustrated by r^2_{power}, seems to reveal presence of some significant components from 14 m to 22 m roughly, but remains inconclusive. Assessment of r^2_{opt} in function of stratigraphic height and sedimentation rate does seem to confirm earlier observations made in the r^2_{power} fitting. Careful interpretation seems to indicate that sedimentation rates in this case are about 2.5 cm/kyr at 14 m, after which a slight decrease is observed towards 2.2 cm/kyr at 22 m. Again, from 22 m onward the r^2_{opt} fit does not seem to provide unambiguous sedimentation rate values.

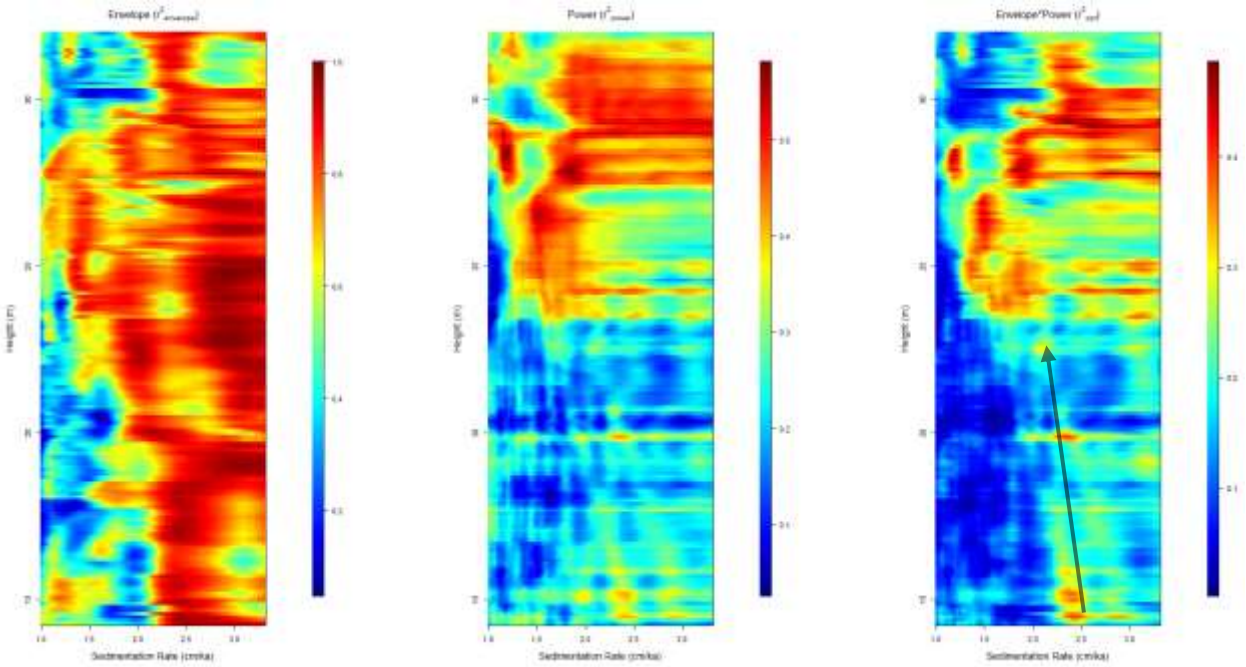

Figure 54: eTimeOpt of Si, left: r²envelope, middle: r²power and right: r²opt (envelope*power). Black arrow indicating observed potential shift in sedimentation rate.

6.2. Terrigenous Input – Potassium

The potassium signal is assessed for its use as a proxy for influx of terrigenous material into the calcium carbonate matrix (da Silva et al., 2012). Based on aforementioned significant correlation between K and the other terrigenous elements Al and Ti and knowing the Ti/Al ratio will be used as a proxy for the composition of terrigenous input, K was preferred so that a larger variety of elements is included in the analysis.

6.2.1. MTM Power Spectrum - Potassium

Using identical parameters as used for the Si and Ca record, the MTM power spectrum for K is displayed below (Fig. 55). The MTM power spectrum of potassium reveals a limited range of elevated spectral power, with most notable all below a frequency of 0.75 cycles/m as well as a statistically significant peaks (according to AR1 95%) around 5.8 and 9.1 cycles/m. The absence of higher frequency components in the MTM power spectrum might mean that either astronomical forcing due to precession, obliquity (and potentially short eccentricity) is not recorded in the potassium signal, or that distortions have altered the signal.

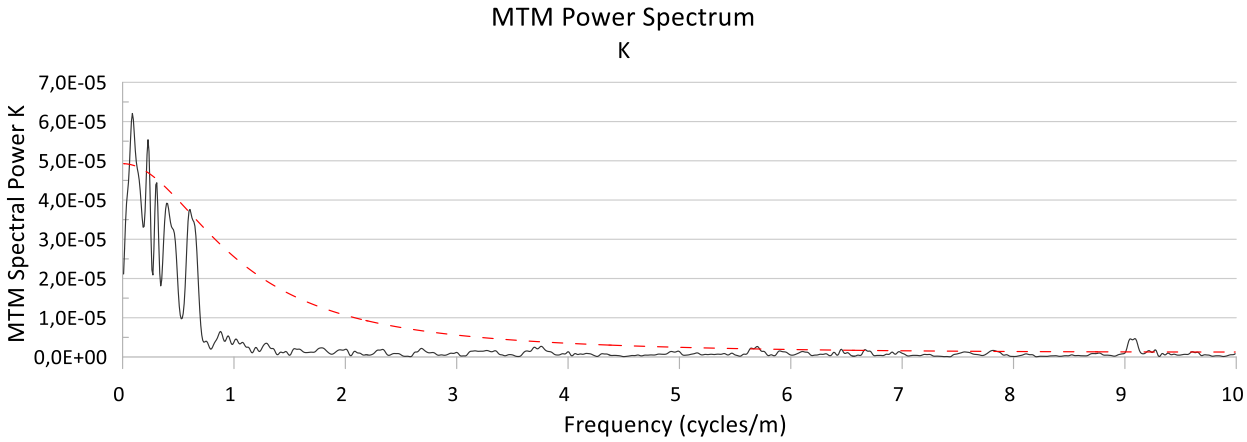

Figure 55: MTM power spectrum for K, red dashed line indicative for AR1 (95%) confidence interval.

6.2.2. Evolutive Harmonic Analysis – Potassium

The EHA of the K signal provides spatially resolved information on the normalized amplitude power for a frequency range from 0 to 5 cycles/m (Fig. 56). The earlier observed low frequency components via the MTM power spectrum are resolved and display strong normalized amplitude power over the complete 14 m to 32 m window. Additionally, a clear shift of the low frequency component to even lower frequencies can be observed from 21.5 m to 27.0 m. This might indicate that the period of the corresponding cycle increases around this stratigraphic height (for example due to a decrease in sedimentation rate). Alternatively, this very low-frequency component might also indicate presence of a new cycle present in the record.

In addition to the low frequency component(s), normalization of MTM spectral power per sliding window reveals additional, high-frequency components in the lower part of the section ranging from 14 m to 24 m. Even though the significance of these signal can be questioned, interestingly enough they are in line with what can be observed from EHA of the Si signal (Chapter 6.1.2.).

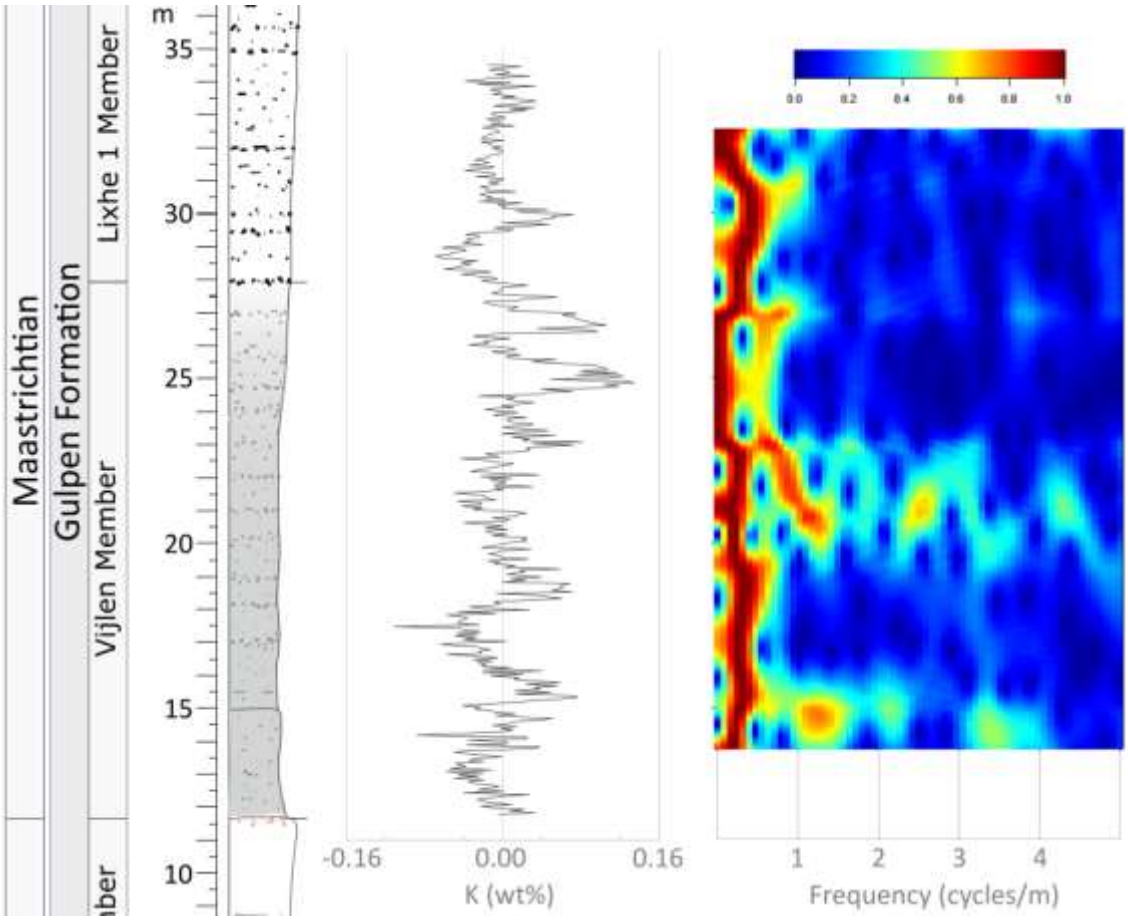

Figure 56: Graphical representation of the Kreco quarry lithostratigraphy (Vellekoop et al., In prep.) with K as well as normalized EHA of K.

6.2.3. Bandpass Filtering – Potassium

Based on identified low-frequency components (MTM power spectrum and EHA) as well as some potential higher-frequency components via EHA of the potassium signal, several bandpass filters were designed to further investigate the K signal. Fig. 57 below displays best fitting bandpass filters, however phase shifts can be observed in most cases (for 0.8 – 1.6 and 0.50 – 0.76 cycles/m filters).

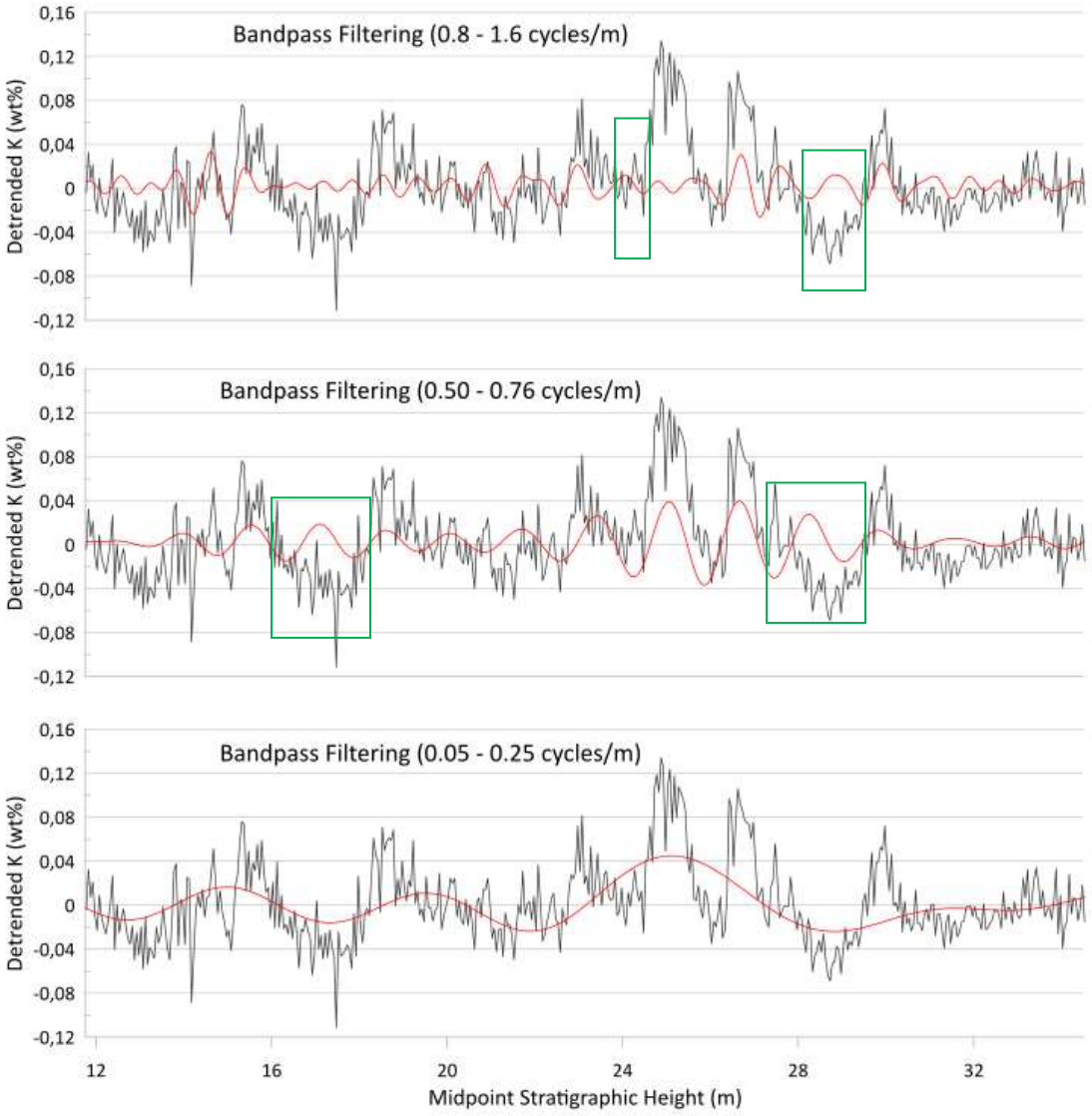

Figure 57: Bandpass filtering based on revealed spectral components of the K data series, noteworthy phase shifts indicated on bandpass filter (0.50 – 0.76 and 0.8 - 1.6cycles/m) output in green.

Given the poor spectral power observed in the MTM power spectrum, as well as bandpass filter outputs not matching optimally with the K signal – with exception of the low frequency (0.05 – 0.25 cycles/m) filter – no further analysis results will be provided and discussed here.

6.3. Terrigenous input – Ti/Al ratio

Similar methodology as described for Si and K in Chapters 6.1. and 6.2. respectively is followed in this chapter, attempting to construct an independent age model based on the Ti/Al ratio. This element ratio is often used as a proxy for changes in the composition of detrital material and is believed to be more resistant to diagenesis (Govin et al., 2012). Therefore, Ti/Al might contain the primary signal of paleoclimate-controlled changes in detrital influx into the carbonate rocks.

6.3.1. MTM Power Spectrum – Ti/Al

MTM power spectra was calculated for Ti/Al ratio and is visualized on the left of Fig. 58 below. The MTM power spectrum is dominated by high spectral power at a range of frequencies. Especially the power of high frequency components is remarkable, which is representative of the fast fluctuations that are observed in the depth domain Ti/Al signal (Fig. 47). Provided that Milankovitch induced climate change is recorded in the Ti/Al signal, an assumed 18.7 kyr precession cycle would correspond to a cycle of 0.187 m periodicity or 5.34 cycles/m periodicity at 1 cm/kyr sedimentation rate.

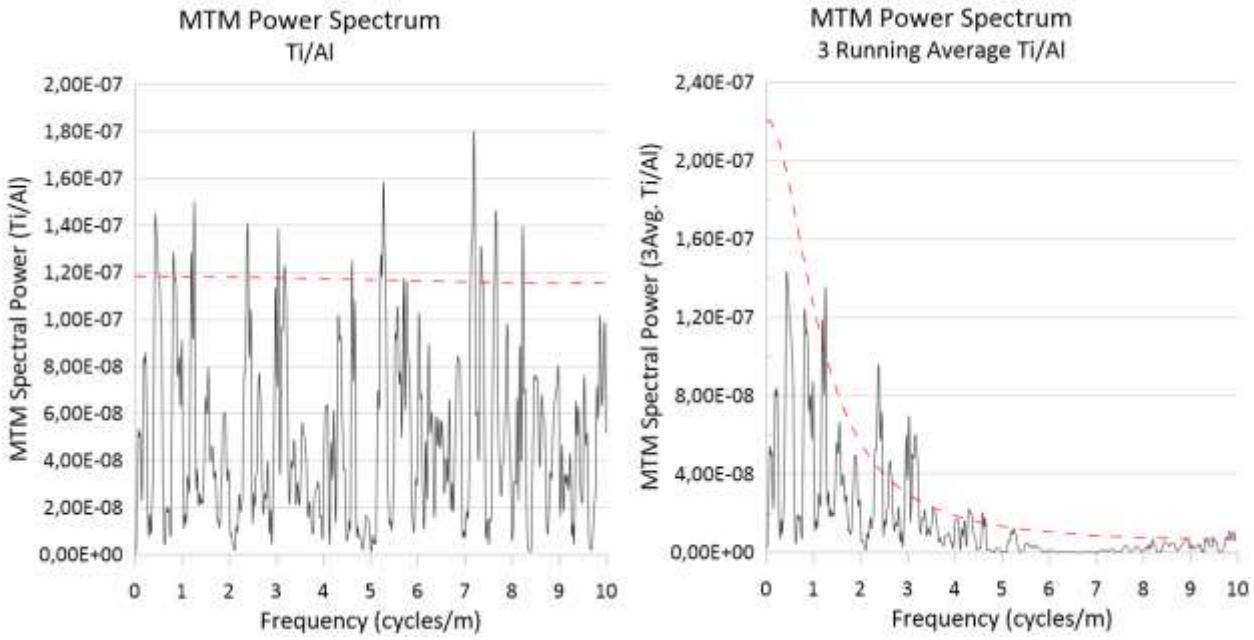

Figure 58: MTM power spectra for Ti/Al and 3 running average Ti/Al, red dashed line indicative for AR1 (95%) confidence interval.

By carrying out a 3-running average of the Ti/Al signal before calculating the MTM power spectrum (Fig. 58, right), most high-frequency components are removed from the MTM power spectrum. If any Milankovitch cyclicity is present in the record, their frequencies should by lower than 5 cycles/m (based on estimated sedimentation rates by Keutgen (2018) and Vellekoop (in prep.). Assuming sedimentation rates to be higher than 1 cm/kyr, no vital information was lost by averaging the Ti/Al signal over 3 datapoints. Conversely, potential short cyclic components may be lost when averaging over 5 or 7 datapoints. From this point onwards, all spectral analyses were carried out on the 3 running averaged Ti/Al signal.

6.3.2. Evolutive Harmonic Analysis – Ti/Al

The EHA of the averaged Ti/Al signal provides spatially resolved information on the normalized amplitude power for a frequency range from 0 to 5 cycles/m (Fig. 59). Three potential cyclic components, number 1 (high frequency), 2 (medium frequency) and 3 (low frequency) are identified using black arrows on Fig. 59.

The high frequency component (3 cycles/m) is present at the lower part of the section that slightly increased in frequency from 14 m to 22 m, after which its frequency seems to decrease to 2.5 cycles/m – as indicated by the black arrows on Fig. 59. Similarly, the second, medium frequency component is present at a frequency of about 1.25 cycles/m at a stratigraphic height of 14 m. Following the black arrows, this cyclic component slightly increased in frequency from 14 m to 22 m, after which its frequency decreases to roughly 1 cycle/m. Lastly, albeit less dominant from 14 m to 17 m, the low frequency component can be identified as well on the normalized EHA of Ti/Al. This component displays similar variation as the 2 aforementioned cyclic components present in the signal.

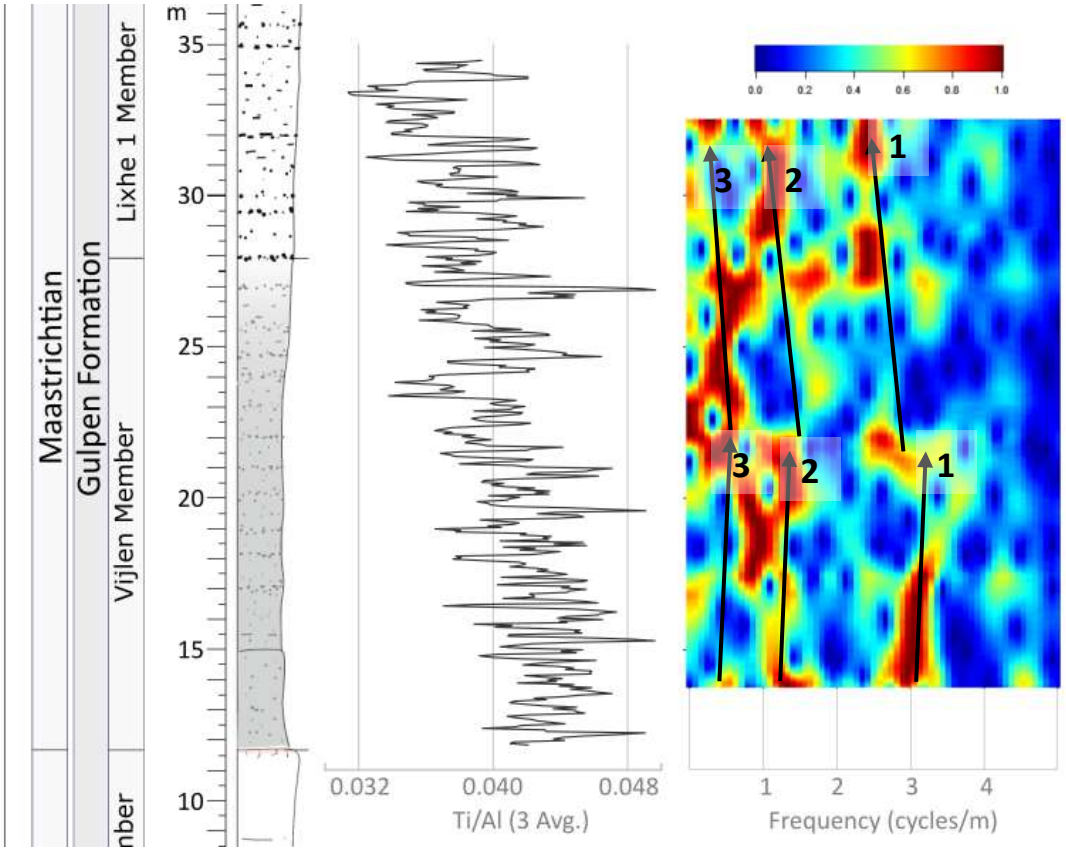

Figure 59: Graphical representation of the Kreco quarry lithostratigraphy (Vellekoop et al., In prep.) with 3-running average Ti/Al as well as normalized EHA of Ti/Al. Full and dashed black arrows indicate potential shift of dominant cycles.

6.3.3. Bandpass Filtering – Ti/Al

Bandpass filters centered around 1.25 cycles/m and appr. 2.5 cycles/m display are in correspondence with observed variations in the detrended Ti/Al signal (Fig. 60). For the bandpass filter taken at a frequency range from 1.05 to 1.45 cycles/m, only one clear discrepancy can be observed near a stratigraphic height of 23 m (marked in green of Fig. 60). For bandpass filter taken at a frequency range from 2.15 to 2.75 cycles/m, even though some smaller phase discrepancies can be observed, again shows a promising overlap with the averaged Ti/Al signal.

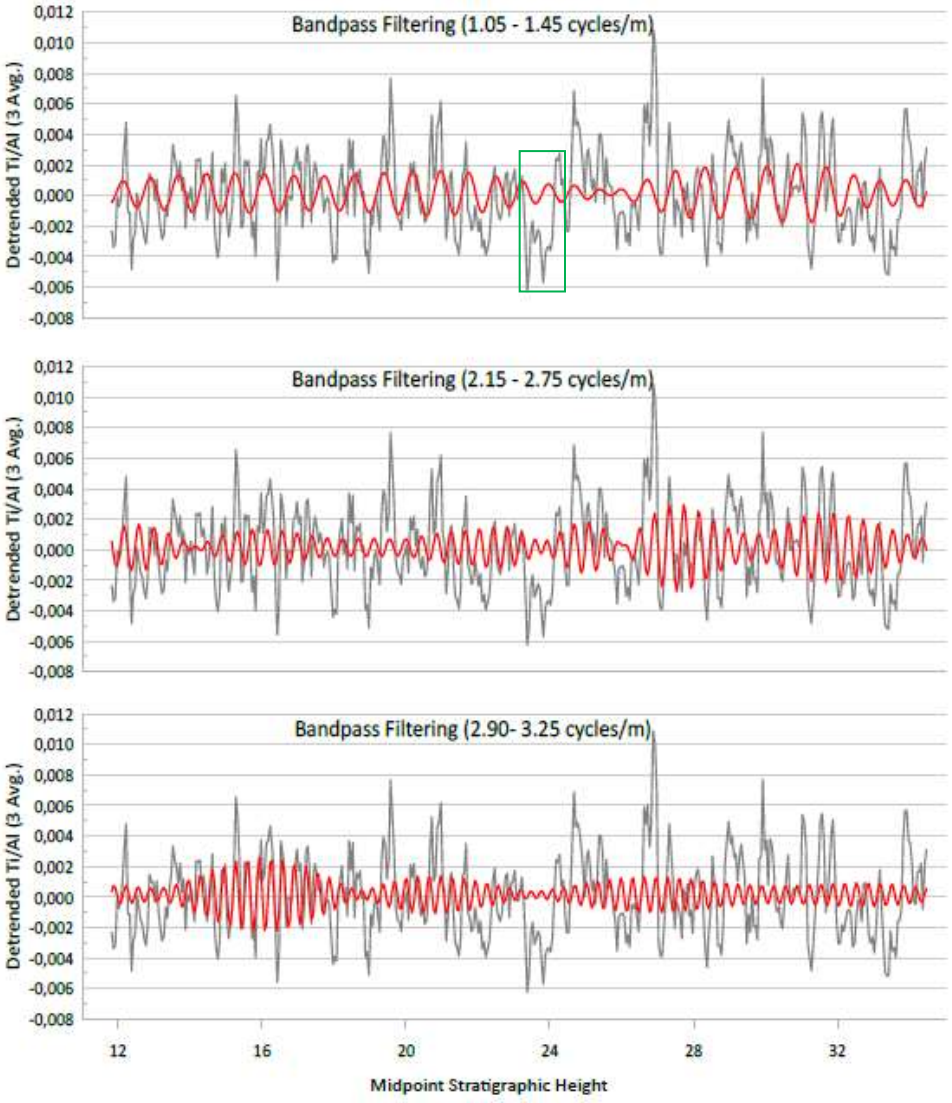

Figure 60: Bandpass filtering based on revealed spectral components of the 3 running averaged Ti/Al data series, phase shifts indicated on bandpass filter (1.05 – 1.45 cycles/m) output in green.

6.3.4. TimeOpt – Ti/Al

EHA and subsequent bandpass filtering revealed a potential for the presence of precession, obliquity and eccentricity cycles. TimeOpt analysis on exponentially detrended Ti/Al ratio was carried out for both precession amplitude and short eccentricity amplitude modulation, using precession periodicity targets set at 23.2 kyr and 18.7 kyr (based on Chapter 2.3.4.) and eccentricity periodicity targets set at 405 kyr, 125 kyr and 95 kyr for 1000 simulated sedimentation rates from 1.0 to 3.3 cm/kyr as a set sedimentation rate.

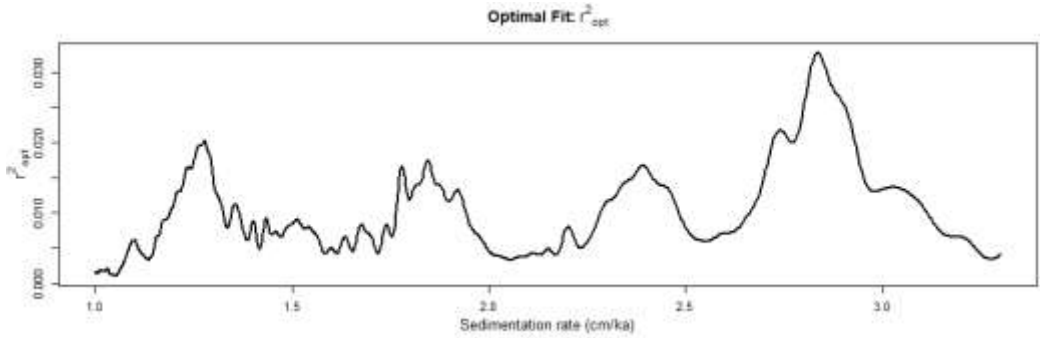

Figure 61: TimeOpt of averaged Ti/Al ratio based on precession amplitude modulation.

For the precession amplitude modulation by eccentricity, an optimal sedimentation rate of 2.83 cm/kyr is computed, however r^2_{opt} does reveal possible lower sedimentation rates of roughly 1.25 cm/kyr, 1.78 cm/kyr and 2.4 cm/kyr to be present as well (Fig. 61). These results are again indicative of either changing sedimentation rates (or presence of hiatuses) or absence of Milankovitch precession and eccentricity cyclicity. TimeOpt carried out on short eccentricity amplitude modulation was also not able to compute one average sedimentation rate whilst still optimizing spectral concentration at the eccentricity targets.

6.3.5. eTimeOpt – Ti/Al

In order to look deeper into the possibility of varying sedimentation rates recorded in the averaged Ti/Al signal, an eTimeOpt was carried out using similar parameters to the TimeOpt. Assessment of the precession amplitude modulation r^2_{opt} reveals sedimentation rates of 1.5 to 1.8 cm/kyr from 14 m to roughly 22 m. From 22 m to 28 m, apparent changes in the record give rise to more uncertainty in sedimentation rate estimations (see Fig. 62). From a stratigraphic height of 28 m (Lixhe 1 Member) onwards, higher sedimentation rates are identified somewhere in the range of 1.8 to 2.3 cm/kyr.

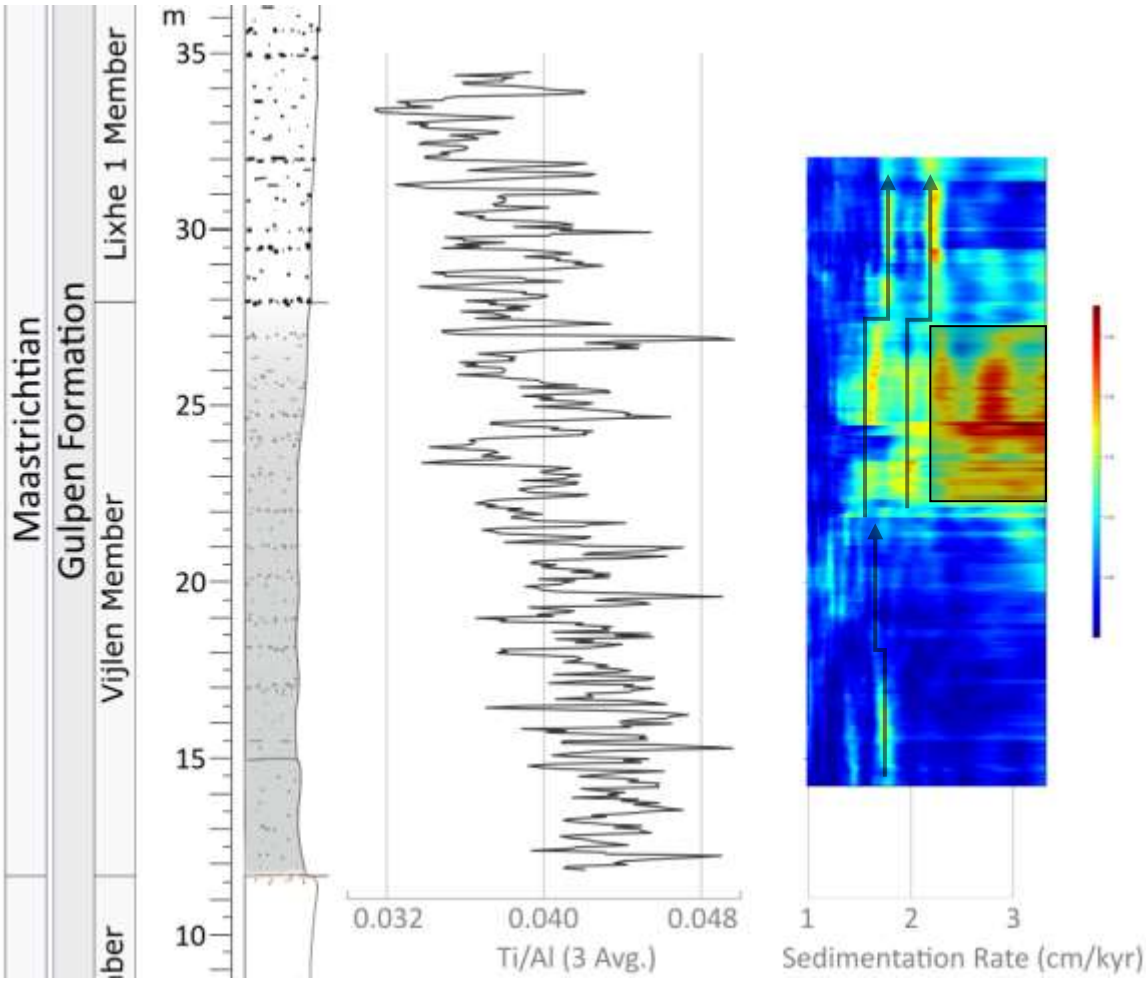

Figure 62: Graphical representation of the Kreco quarry lithostratigraphy (Vellekoop et al., In prep.) with 3-running average Ti/Al as well as eTimeOpt r²opt of Ti/Al. Full black arrows indicate potential shift of sedimentation rates.

Observations from eTimeOpt are in full agreement with what was interpreted in the EHA (Fig. 59). Sedimentation rates are lower towards the bottom of the Vijlen Member and slightly decrease upwards until a stratigraphic height of about 22 m. From 22 m onwards sedimentation rates gradually increase and remain so in the Lixhe Member. Even though analyses based on potential presence of precession and eccentricity prove useful, potential presence of obliquity cyclicity has not yet been exploited.

6.3.6. Obliquity Cycle Counting

Assuming astronomical forcing of the Ti/Al ratio as a paleoclimatic proxy for the change in composition of terrigenous material, and combining insight gained from MTM power spectrum, EHA and bandpass filtering, attribution of obliquity cyclicity has been made possible. Use of the potential obliquity cyclicity allows for an approach complementary to (e)TimeOpt analyses that were based on assumed precession and eccentricity. Taking into account sedimentation rate variations in the Ti/Al record, an average sedimentation rate of 2 cm/kyr over the complete record can be used to link the spectral component at a frequency of 1.25 cycles/m (or 0.8 m periodicity) to 29 obliquity cycles with a duration of roughly 40 kyr as visualized on Fig. 63.

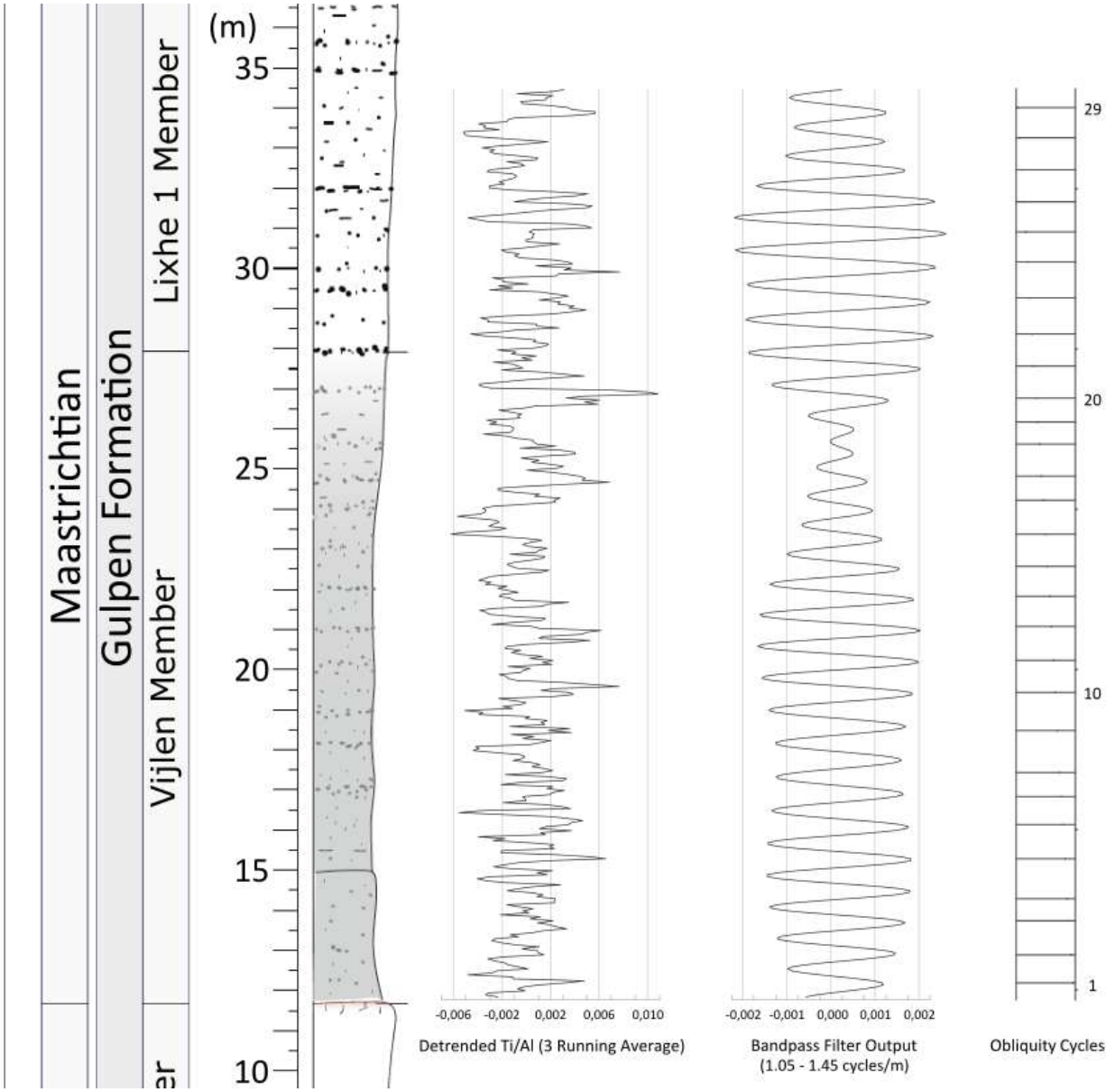

Figure 63: Lithology (Vellekoop et al., In prep.), detrended Ti/Al (3 running average) signal, bandpass filter output for spectral window of 1.05 – 1.45 cycles/m and 29 counted obliquity cycles.

In addition, each local maximum in the Ti/Al signal seems to be comprised of 2 individual components which could be related to precession cyclicity with a duration of approximately 20 kyr. Direct, visual identification of eccentricity cycles is less straightforward even though spectral analysis revealed strong indication of short eccentricity cyclicity (spectral power at a frequency of 0.4 cycles/m, see Fig. 59).

Earlier observed changes throughout the record at stratigraphic heights ranging from 22 m to 28 m (Lixhe Horizon) are reflected as well in the decreased amplitude of the bandpass filter output and could be a source of increased uncertainty of obliquity cycle attribution. The exact mechanisms behind these changes in the record are difficult to unravel based on the available data and could be due to the presence of a hiatus, drastic changes in sedimentation rates or paleoenvironment.

6.3.7. Tuning of Ti/Al record – Astronomical Age Model

Using the identified obliquity cycles as tie points, relative dating of the record and construction of a floating age model was made possible (see script in appendix 11.1) by assigning relative ages to key stratigraphic heights. In this case, obliquity cycle maximum '1' was first set at a relative age of 20 kyr at 12.175 m, obliquity cycle maximum '29' was set at a relative age of 1140 kyr at 34.025 m (see also Fig. 66). Based on the Ti/Al time domain signal and the age model matrix, the stratigraphic series was tuned from the space domain to the time domain. The obtained floating astronomical timescale encompasses an estimated 1120 kyr (Fig. 64).

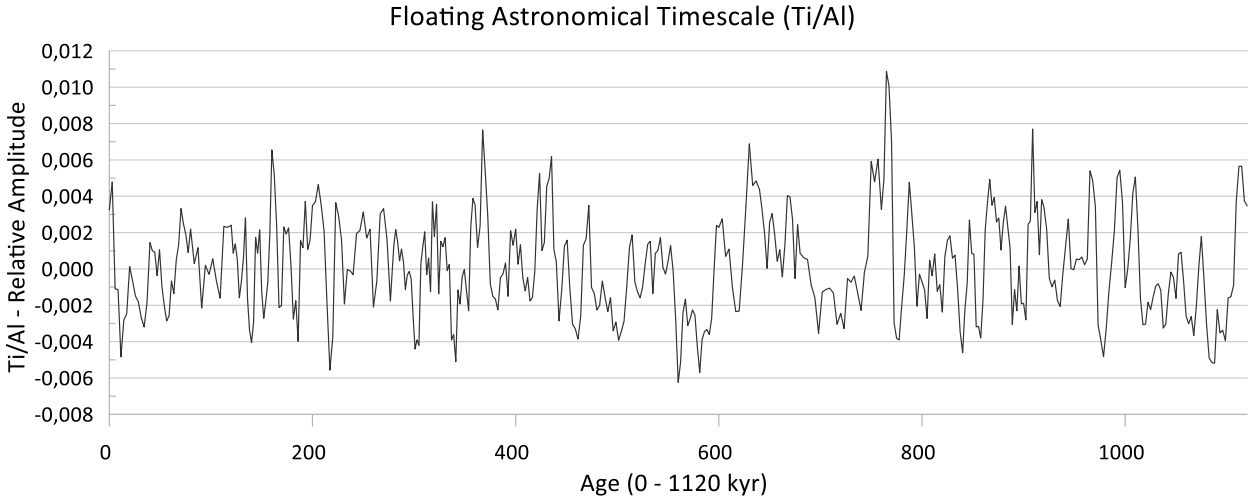

Figure 64: Floating Astronomical Timescale based on tuned Ti/Al record based on identified Milankovitch obliquity cyclicity.

To check the validity of the assumption of Milankovitch obliquity cyclicity to be present, MTM power spectrum of the linearly interpolated tuned stratigraphic series was calculated in analogy with the methodology applied on the depth domain signals. Aside from the expected obliquity spectral component at a frequency of 0.025 cycles/kyr, two more spectral components are revealed at frequencies 0.050 cycles/kyr and 0.008 cycles/kyr corresponding to precession (20 kyr) and short-eccentricity (125 kyr) Milankovitch cycles respectively (Fig. 65).

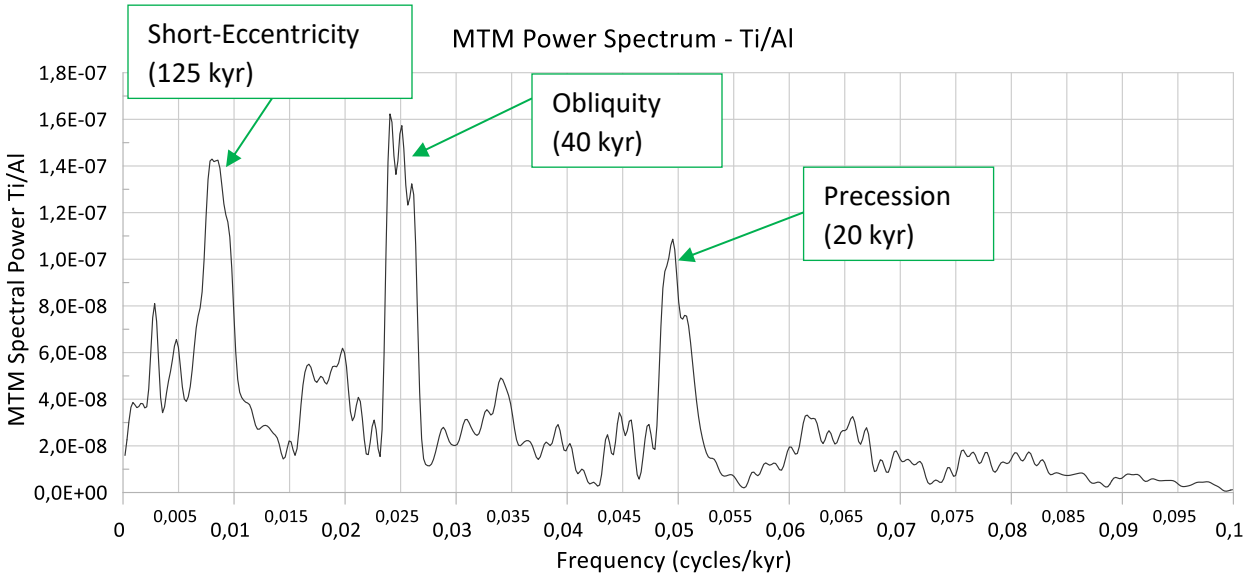

Figure 65: MTM power spectrum of the astronomically tuned Ti/Al series, revealing identified Milankovitch precession, obliquity and short-eccentricity cycles

The well-known 405 kyr eccentricity cycle or “metronome”, introduced in Chapter 2.3.1., was not identified in this time record. This can most probably be attributed to the fact that the tuned stratigraphic series spans only appr. 1120 kyr, which is relatively short to come to a statistically significant number of 405 kyr eccentricity cycles (which might also explain lower overall r^2_{opt} values in the eTimeOpt analysis).

Bandpass filtering of the identified precession, obliquity and eccentricity was carried out on the tuned time series (Fig. 66). The bandpass filter representing Milankovitch precession cycles (0.046 – 0.052 cycles/kyr frequency) is in good agreement with the tuned Ti/Al signal. Similarly, the bandpass filter representing short-eccentricity (0.006 – 0.012 cycles/kyr frequency) overlaps well with longer periodicity trends in the Ti/Al signal.

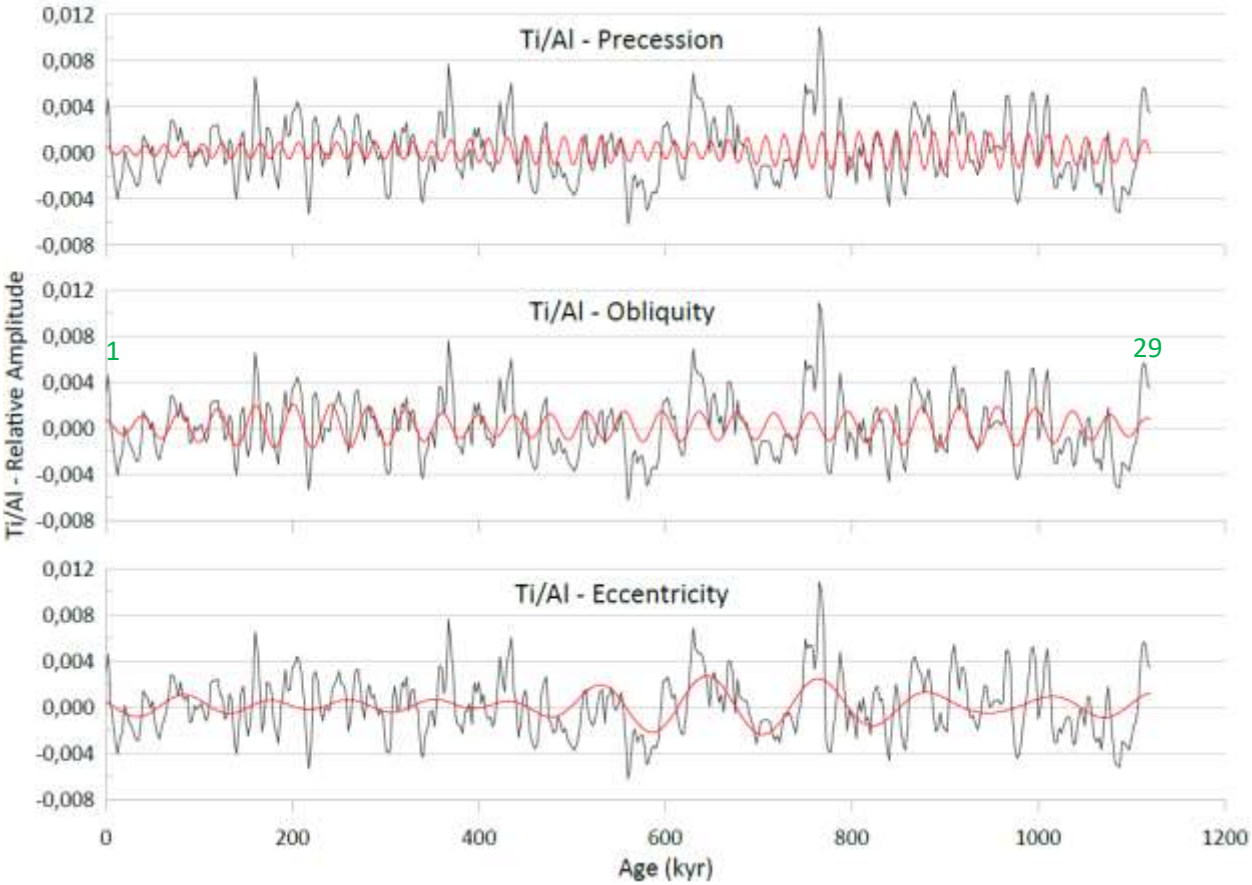

Figure 66: Tuned Ti/Al time series record with superimposed precession, obliquity and eccentricity bandpass filter output (red). Counted obliquity cycles '1' and '29' indicated in green.

7. Discussion

First, the $CaCO_3$ and SiO_2 concentrations, their relationship with the occurrence of flints and potential for cyclostratigraphy will be discussed. Secondly, the use of cyclostratigraphy on the Ti/Al proxy for the construction of a new age model for the type-Maastrichtian near Hallembaye is elaborated. Finally, its implications and relevance is touched upon before anchoring the new astrochronological timescale based on a newly proposed chemostratigraphic framework for the type-Maastrichtian.

7.1. $CaCO_3$ and SiO_2, Flint Occurrence and Milankovitch Cyclicity

The Kreco quarry near Hallembaye has a distinct lithology where flints/cherts are scattered throughout the chalk rocks either as nodules or as true flint bands. The main component of the chalk is confirmed to be $CaCO_3$ using µXRF elemental analysis. $CaCO_3$ concentrations stay well above 90% in the Zeven Wegen Member (Fig. 41), then drop drastically to values of about 50% at the Froidmont Horizon, alluding to a drastic change in the depositional environment. A combination of several mechanisms, such as decreased carbonate production, increased influx of detrital material could be behind this – see Chapter 7.4. A gradual recovery of the $CaCO_3$ concentration is observed throughout the Vijlen and Lixhe 1 – 3 Members, where whitish chalk contains about 97% $CaCO_3$. This high purity reflects unequivocally a minor input of detrital material.

High concentrations in $CaCO_3$ correspond to a depositional environment favoring carbonate production whilst limiting detrital input. Especially for the interval from 11.75 m from 34.50 m, which was sampled at a 5 cm-high resolution, the relationship between the lithology and geochemical composition is of interest. This interval spans a transition from greyish chalk with some rare flint bands and flint nodules, to a whitish chalk with more distinct flint nodules and layers – which was also the reason for this cyclostratigraphic study.

The logged occurrence of flints was translated to numerical values (Fig. 67) to allow for a visualization and subsequent discussion. Arbitrary values representing flint probabilities were attributed to observed individual flint nodules (0.10), possible flint band (0.50), faint flint band (0.66), flint band of individual nodules (0.75) and clear flint band (1.00). The overlaid, detrended Si signal allows for visual comparison between the flint probabilities. These probabilities are also a measure of how certain a potential correlation can be made with the Si signal. The lower the flint probability, the lower the certainty of those flints to be situated at a specific stratigraphic height. For example, individual flint nodules (0.10) are more scattered throughout the chalk and consequently do not occur strictly at one given stratigraphic height. Clear flint bands (1.00) on the other hand are described at a higher precision with regards to their stratigraphic location. Therefore, conclusions based on their appearance and overlap with the Si signal should be made carefully, especially when flint probabilities are lower. Even more so, there seems to be a slight offset; most of the observed flints occur about 10 cm higher along the stratigraphy compared to local maxima in the Si signal (green arrows, Fig. 67).

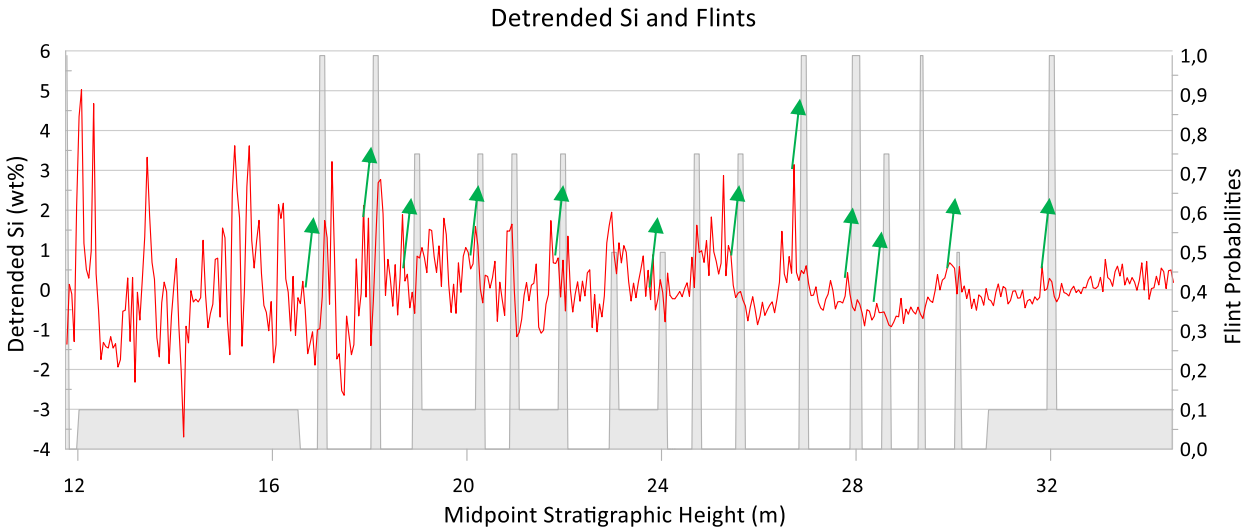

Figure 67: Flint probabilities (0 to 1) in grey and detrended Si (wt%) in red, green arrows indicating potential offset.

Even though it remains hard to relate the visually observed individual flint nodules (0.10 probability) to the Si concentration, the possible, faint and clear flint bands on the other hand seem to correspond well with an increased concentration in Si (and consequently SiO_2). This implies flints are formed only when SiO_2 concentrations in the bulk chalk ($CaCO_3$) are high enough and that, even after the diagenetic process which unequivocally causes a depletion of SiO_2 out of the chalk matrix upon flint formation, SiO_2 concentrations remain sufficiently high.

A potential hypothesis could be that increasing SiO_2 concentrations reach a threshold concentration – either prior to or during diagenesis – after which subsequent diagenetic processes cause a depletion of the SiO_2, hence leading to observed flints at higher stratigraphic heights than local SiO_2 maxima. These observations and hypothesis would confirm Zijlstra's view on flint nodule formation in the Lixhe and Lanaye members of the upper Gulpen Formation (Zijlstra 1994; Jagt and Jagt-Yazykova 2012). Zijlstra hypothesized that dissolution of biogenic silica (opal) during late diagenesis and subsequent concentration thereof at sites of relatively high concentrations of early diagenetic authigenic silica led to flint nodule formation. Hence, a proportionality between the concentration of flints and the concentration of early-diagenetic silica was assumed – controlled by astronomically forced paleoclimate (Zijlstra, 1994). However, during diagenesis, (vertical) migration of dissolved silica is possible in the sediment (Jurkowska and Świerczewska-Gładysz, 2020). This may very well explain why increased flint probabilities are observed 10 cm higher along the stratigraphic column compared to local maxima in the silica signal (Fig. 67) and might provide an alternative hypothesis to which mechanism is determining eventual flint occurrence.

Both hypotheses, or a combination thereof, might explain the relationship between Si concentrations in chalk and the occurrence of flints. However, a definitive link between chalk geochemistry and the flint occurrence can only be made on a preliminary basis for the Vijlen and part of the Lixhe 1 Members. The reason for this is that flints occur not often and regular enough (compared to Lixhe 2 – 3 and Lanaye Members) to establish a statistically significant relationship with the Si signal. In any case, the most probable hypothesis, which is in agreement with Zijlstra (1994), is that increased amounts of silica (in

chalk) are related to flint occurrence. The exact mechanism that drives this relationship however cannot be confirmed based on the data available in this work. Lastly, given rhythmically paced flint cycles occur more regularly at higher stratigraphic intervals (e.g. Lixhe 2 and 3 Members), these would provide a stronger basis for comparison with the Si signal and to further test hypotheses formulated by Zijlstra (1994).

Si concentrations reflect visual observations in lithology, but spectral and time series analyses of the Si signal revealed no clear link between Si concentrations and Milankovitch cyclicity (Chapter 6). EHA revealed presence of cyclic components with a 6:2:1 ratio in the Vijlen Member (12 m up to 23 m) – reminding us of the precession-obliquity-short-eccentricity ratio. Yet, these cannot be linked to specific Milankovitch cycles based on the sedimentation rates provided by corresponding (e)TimeOpt analyses. When assuming average sedimentation rates of 2 cm/kyr (based on Ti/Al ratio analyses), the revealed cyclic components in the Si signal (of the Vijlen Member, 12 m to 23 m) would encompass 13.9 kyr, 27.8 kyr and 83.3 kyr respectively. These timescales do not correspond to known astronomical solutions as introduced in Chapter 2.3. For the upper part of the Vijlen Member as well as the lower part of the Lixhe 1 Member, insufficient spectral power was present in the record (Fig. 51).

Even though astronomical forcing might have affected Si supply or the diagenetic processes that formed the flint layers, this does imply that a primary signal of astronomical nature was recorded. Also, given the diagenetic origin of flints, it is very probably that any primary signal – if present at all at any point in time – was distorted or erased. Consequently, the occurrence of flints cannot be directly related to astronomically forced changes of Si concentrations in the Vijlen and part of the Lixhe 1 Members. For this interval of the type-Maastrichtian, Zijlstra's hypothesis of Milankovitch precession-paced flint bands cannot be confirmed. However, given the potential link between lithology and elemental composition of the chalk, as well as the Milankovitch-like pair-ratios that were observed, it can be understood why one would carry out preliminary attempts at cyclostratigraphy using rhythmically paced flint bands.

7.2. Terrigenous Input and Milankovitch Cyclicity

7.2.1. Concentration of Terrigenous Material

Changes in input of terrigenous material into the Maastrichtian carbonate factory were observed in type-Maastrichtian chalk of the Vijlen Member and part of the Lixhe 1 Member, represented firstly by variations in concentration of terrigenous elements such as Al, K and Ti. At the lower part of the section (from 11.75 m up to 19 m roughly) clear differences (e.g. phase shifts) can be observed between trends displayed by terrigenous elements such as Al, K and Ti on one hand, and Si and Ca on the other hand. At higher stratigraphic heights from 19 m up to 34.50 m, no distinct phase shifts were observed and trends in terrigenous elements and Si and Ca are very similar. This could be indicative of changes in depositional environment, such as a lower eustatic sea level in the early Maastrichtian linked to higher concentrations of detrital material in carbonate rocks, followed by a rise in sea level (Engelke et al., 2018; Voigt and Schönfeld, 2010) yielding the pure chalk of the Lixhe Members at the Kreco quarry.

Spectral analysis carried on the K signal revealed presence of low-frequency cyclic components (< 1 cycles/m) mainly, with most significant spectral power concentrated around a frequency of 0.25 cycles/m (or a periodicity of 4 m per cycle). Assuming an average sedimentation rate of 2 cm/kyr, this would correspond to a 200 kyr cyclicity – about half the length of a long-eccentricity cycle of 405 kyr – similar to what was observed for Si and Ca signals (Fig. 45). However, as introduced in Chapter 2.3.5., this is far from sufficient to conclude that variations in concentration of terrigenous influx are astronomically forced (Waltham, 2015). Therefore, the hypothesized drastic changes in the depositional environment cannot be confirmed to be of astronomically forced origin. Likewise, it cannot be confirmed that these changes reflect a cyclic variation of the paleoclimate rather than diagenetic processes.

The significant correlation between MS and terrigenous elements, Si and especially Fe at high resolution indicate that a link exists between detrital input (e.g. clays, quartz minerals) and the MS signal for the type-Maastrichtian chalk exposed at the Kreco quarry. Especially the strong similarity between the MS signal and the Fe signal is unsurprising, given Fe-containing minerals are often the main carriers of the MS signal (da Silva et al., 2012). However, investigating whether the MS signal is of primary nature or not (ruling diagenesis and/or re-magnetization) is required when trying to link the MS signal to paleoclimatic or paleoenvironmental changes (da Silva et al., 2009; Ellwood and Crick, 2000). Only when the primary nature of the MS signal is established can its potential as a proxy related to changes in terrigenous input be tested in a cyclostratigraphic approach.

7.2.2. Composition of Terrigenous Material

Assessment of changes in the depositional setting was carried out alternatively by evaluating variations in the composition of terrigenous material rather than looking at changes in the concentration of terrigenous material, in this case the Ti/Al ratio which is insensitive to diagenesis (Westphal et al. 2010). This element ratio reflects non-carbonate fractions (e.g. clay minerals) with variations in Al and Ti content that reflect the source material (Westphal et al. 2010). The Vijlen Member and part of the Lixhe 1 Member display a steadily decreasing trend in Ti/Al, with distinct rhythmic superimposed fluctuations. While it may remain hard to pinpoint the exact driver of the negative trend observed in Ti/Al, it could represent a gradually changing nature of terrigenous influx (Engelke et al., 2018). In the upper Campanian – lower Maastrichtian chalk succession of Kronsmoor (Northern Germany), reflecting a similar sedimentary and paleogeographic setting, obliquity paced cyclicity in Ti/Al was interpreted to reflect astronomically forced changes in the amount of either aeolian supply or the provenance thereof (Engelke et al., 2018). Even though direct stratigraphic correlation between the Hallembaye section and the Kronsmoor section (upper Campanian – lower Maastrichtian) has not yet been carried out, the similarity in paleogeographic setting suggest that a similar mechanism could be at play in the Hallembaye record.

Regardless, the superimposed cyclic variation of Ti/Al reflects Milankovitch cyclicity. Identification of at least 3 Milankovitch cycles (20 kyr precession, 40 kyr obliquity and 125 kyr short-eccentricity) was carried out using a complementary analysis based on precession-eccentricity and an independent analysis based on obliquity. Astronomical tuning of the time-domain record using identified obliquity cycles confirmed the presence of both precession and short-eccentricity cycles – which is statistically important when considering the required amount of Milankovitch pair-ratios as discussed by Waltham (2015). Identification of 3 Milankovitch cycles confirms astronomical forcing of the paleoclimate, leading to observable changes in the detrital cycle (Fig. 1). Relevance of this observation is twofold; firstly, it provides insight in the local depositional setting of the type-Maastrichtian chalk of the Gulpen Formation and secondly, indicates astronomical forcing of the paleoclimate during the Maastrichtian.

Whereas the amount of terrigenous material (reflected by K) did not provide insight, the provenance (or amount of aeolian dust) is sensitive to cyclic changes in the paleoenvironment. For the Kreco quarry, where diagenesis potentially affected the record as discussed in Chapter 7.1, identification of Milankovitch cyclicity recorded by diagenesis insensitive proxy enables construction of an astronomical age model. Where other geochemical proxies (e.g. $CaCO_3$-content) may be affected by diagenesis, Ti/Al has the potential to serve as a powerful tool for cyclostratigraphy applied on Campanian-Maastrichtian chalk successions.

7.3. A New Astronomical Age Model

A new astronomical age model is proposed for the Vijlen Member and part of the Lixhe 1 Member, ranging from 11.75 m to 34.50 m (Gulpen Formation, Kreco quarry near Hallembaye). Based on spectral analysis and tuning of the Ti/Al record based on the identified obliquity cycles, the interval of 22.75 m, encompasses about 1.12 Myr – deposited with an average sedimentation rate of ~2 cm/kyr. This average sedimentation rate is in line with those reported by Felder (1996), who estimated early Maastrichtian sedimentation rates for the type-Maastrichtian to be between 1.33 cm/kyr to 2.4 cm/kyr – back then based on lithostratigraphic units and biostratigraphy (Felder, 1996). The lower part of the Vijlen Member has relatively lower sedimentation rates of about 1.8 cm/kyr, decreasing even further to 1.5 cm/kyr at a stratigraphic height of 22 m. From this point onwards, sedimentation rates seem to increase again to yield higher values in the Lixhe 1 Member of 1.8 cm/kyr to 2.3 cm/kyr. These variations lie completely in line with the estimated rates by Felder (1996).

The sedimentation rates reconstructed here are in stark contrast with the reported 5 cm/kyr sedimentation rates for the upper Gulpen (Lixhe Member) at CBR-Lixhe and ENCI by Felder et al. (2003). However, as already stated by Felder in 1996, the observed differences in sediment thickness observed in the different type-Maastrichtian localities due to changes in the depositional environment explain why such differences could exist between the Kreco quarry and ENCI. The CBR-Lixhe quarry however is located nearly back to back to the Kreco quarry, which would imply a drastic change in sedimentation rates on a local scale. This suggests that the sedimentation rates reported by Felder et al. (2003) based mainly on bioclasts as well as $\delta^{18}O$ (which could have been impacted by diagenesis) are overestimated (Felder 1996; Voigt and Schönfeld 2010).

Based on work of Felder, Zijlstra and others, Keutgen reported an initial age model (using long eccentricity cycles mainly) for the type-Maastrichtian chalk exposed at the Kreco (formerly known as CPL SA-Haccourt) quarry that was based mainly on bioclasts (e.g. bivalves) as well as on the rhythmically-paced flint layers (Keutgen 2018). Even though no absolute constraints were mentioned for the specific interval starting from the Froidmont Horizon to the Lixhe 1 Member, long eccentricity Milankovitch cycles indicate that the Vijlen and Lixhe 1 Member exposed at the Kreco quarry should not encompass more than 1.2 Myr (Keutgen 2018). Being the similar to those reported by Keutgen (2018), sedimentation rates for the Vijlen Member are slightly lower (1.8 cm/kyr) compared to Lixhe 1 (up to 2.3 cm/kyr) for the interval investigated. Given the investigated interval encompasses at least 1.12 Myr (with the upper part of Lixhe 1 not included), the total duration proposed by Keutgen (2018) is most probably too short. However, this can only be confirmed once the complete Lixhe 1 Member has been included in the astronomical age model. This is especially true when looking at the slightly lower observed sedimentation rates compared to those reported by Keutgen (2018), which might indicate even more discrepancies in his age model. Lastly, based on the chemostratigraphy by Vellekoop (in prep.), the base of the Vijlen Member at Kreco is dated at 70.4 Ma, not at ~69.7 Ma as Keutgen proposed. Exact comparison of identified Milankovitch in this work with those proposed by Keutgen remains hard, especially due to the way correlation was made between potential Milankovitch cycles and assumed correspondence in bioclast composition.

7.4. Implications and Relevance

Even though this master thesis focused on the type-Maastrichtian chalk succession of the Gulpen Formation exposed at the Kreco quarry, insight in some of the driving mechanisms of paleoclimate and paleoenvironment is of relevance to other Upper Cretaceous chalk deposits as well. Firstly, the Kreco quarry represents a small piece of a larger puzzle that is unraveling the Late Cretaceous climate. Secondly, applied methodologies and use of diagenetic-robust proxies that enable the construction of a new independent age model for type-Maastrichtian chalk are potentially applicable to similar sections that originated in the Cretaceous Chalk Sea. Lastly, the difference in depositional environment between the Gulpen Formation (Hallembaye) and other more investigated sections near Kronsmoor, Germany (Engelke et al., 2018; Voigt and Schönfeld, 2010), Gubbio - Italy (Voigt et al. 2012; Sinnesael et al. 2016; Sinnesael et al. 2019)), Zumaia, Spain (Batenburg et al., 2014; ten Kate and Sprenger, 1993) and the Stevns-1 core, Denmark (Thibault et al. 2012; Voigt et al. 2012; Surlyk et al. 2013)(Fig. 68) may reveal insights in which mechanisms are of local or continental scale. Conversely, use of an integrated stratigraphic approach, exploiting the newly developed age model for part of the Gulpen Formation, may allow for correlation of the Hallembaye section with aforementioned sections which evidently is of high value to refine existing Maastrichtian chronologies (Batenburg et al., 2014).

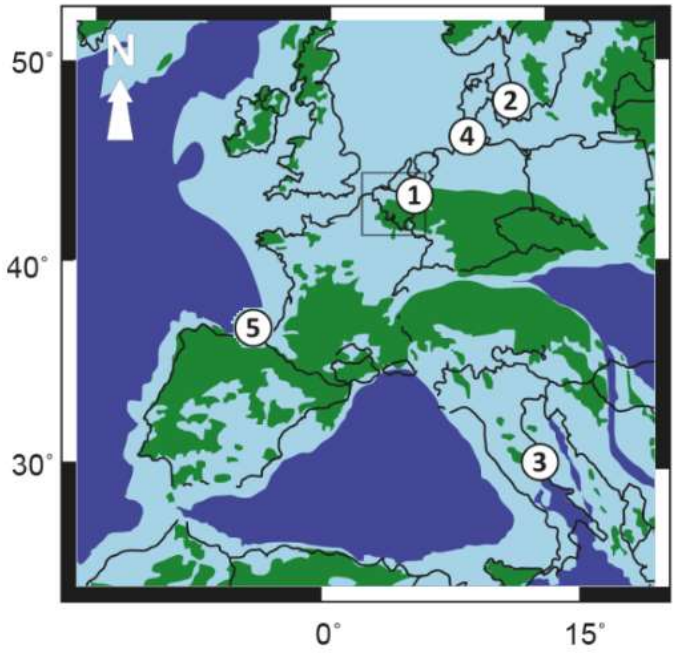

Figure 68: Paleogeographical map of Europe, with (1) Hallembaye, (2) Stevns-1, (3) Gubbio, (4) Kronsmoor and (5) Zumaia, adapted from Vellekoop et al. (In prep.).

7.4.1. Kronsmoor – northern Germany

Situated in the northern part of Germany, the Kronsmoor section contains a complete, continuous succession of upper Campanian – lower Maastrichtian white chalk, deposited in Cretaceous Chalk Sea (North Sea Basin) (Engelke et al., 2018; Voigt and Schönfeld, 2010). Even though this section is not precisely age-equivalent to the Gulpen Formation, its setting provides the basis for discussing the impact of the paleoclimate and depositional setting on carbonate deposits.

The paleoenvironment of the Kronsmoor Formation was believed to be a tectonically stable carbonate platform at water depths ranging from 50 – 200 m (Voigt and Schönfeld, 2010). These pure chalk deposits (with $CaCO_3$ concentrations ranging from 85% to ~100%) recorded both long-eccentricity (405 kyr) and short-eccentricity (100 kyr) Milankovitch cycles in for example $CaCO_3$ and $\delta^{13}C$, which were already used to correlate local sections (Voigt and Schönfeld, 2010). In addition, reduced carbonate content due to an increase in terrigenous material is believed to be related to changes in the detrital cycle due to a series of sea-level falls during the Campanian-Maastrichtian (Voigt and Schönfeld, 2010). Amongst others, fluctuations in aeolian supply and astronomically forced dust input strongly influenced the carbon cycle during the late Cretaceous Chalk Sea near Kronsmoor (Engelke et al., 2018).

Compared to the Hallembaye record, the Kronsmoor Formation was deposited at slightly higher latitudes, further from the Mid-European Island (see Fig. 12 and Fig. 68), where the Chalk Sea was believed to be deeper (Engelke et al., 2018; Voigt and Schönfeld, 2010). The Gulpen Formation which was deposited at lower latitudes, near the Mid-European Island in a channel system situated at a topographic high (Felder 1983; Felder 1997). Whereas the Kronsmoor Formation is characterized by relatively stable sedimentation rates of 2.4 cm/kyr (Engelke et al., 2018; Voigt and Schönfeld, 2010), the Gulpen Formation is characterized by a large hiatus across the Campanian-Maastrichtian boundary interval, and most probably varying, slightly lower sedimentation rates averaging at 2 cm/kyr.

Given the similarities in paleoclimate yet slight differences in depositional setting, correlation between both Formations cannot be carried out at this point because the studied age-equivalent interval to the Gulpen Formation is not enclosed at Kronsmoor (Engelke et al., 2018). Consequently, it can be understood why it is possible that observed Milankovitch cyclicity as reported by Voigt and Schönfeld (2010) and Engelke et al. (2018) for the Kronsmoor Formation based on $CaCO_3$ content was not possible for the Gulpen Formation. However, presented evidence of astronomical forcing of the paleoclimate, recorded by the Ti/Al proxy in the type-Maastrichtian chalk of the Gulpen Formation reveals similarities with those made on chalk of the Kronsmoor Formation (Engelke et al., 2018). For both Formations, astronomically driven changes of the paleoclimate and paleoenvironment were recorded as a primary signal by the Ti/Al proxy (Engelke et al., 2018). Regardless of the slight differences between both Formations, this indicates that the Milankovitch-induced, changing Late Cretaceous paleoclimate leads to variations in aeolian supply (or provenance of terrigenous material, or a combination of both) not only on a local scale, but also on a larger (> 500km) scale.

7.4.2. Zumaia – northwest Spain

At Zumaia, rhythmic successions of hemipelagic limestone and marl are exposed and already provided evidence for astronomical forcing based on $CaCO_3$ as well as MS (ten Kate and Sprenger, 1993) and reflectance analysis and MS (Batenburg et al., 2014). Rather than the pelagic carbonates of some other sections discussed here (e.g. Chapter 7.4.1 and Chapter 7.4.3), these carbonates reach significantly lower concentrations of $CaCO_3$ compared to the type-Maastrichtian chalk – averaging at about 40% for the Maastrichtian part of Zumaia (ten Kate and Sprenger, 1993). These differences can easily be attributed to a difference in depositional environment; at Zumaia, the Basque-Cantabric Basin was a deep intra-plate trough from the Campanian to the Eocene (Batenburg et al., 2014), deposited at paleodepths of 1000-3000 m. Even more so, at Zumaia turbidites are present in the section as well (Batenburg et al., 2014), which is in contrast with the Gulpen Formation.

Cyclic variations in lithology display indications of eccentricity-modulated precession and the 405 kyr metronome allowed for astronomical calibration of the Zumaia section (Batenburg et al., 2014). The 405 kyr metronome was not identified in the type-Maastrichtian exposed near Hallembaye, which can be attributed to the limited interval spanning only 1.12 Myr.

7.4.3. Gubbio – central Italy

Near Gubbio, Umbria, another Campanian-Maastrichtian succession is exposed, consisting of pink micritic limestone (i.e. similar to type-Maastrichtian chalk) which are believed to have originated from continuous deposition in the Umbria-Marche pelagic paleo-basin (Sinnesael et al., 2016; Voigt et al., 2012). Quite similarly to the Kronsmoor Formation, a terrigenous component of aeolian origin is also present in the carbonate succession (Sinnesael et al. 2016 and references therein).

Again, this deep marine basin setting (paleodepths > 200 m) (Sinnesael et al., 2016) is in stark contrast with the one of the type-Maastrichtian section exposed near Hallembaye, were discontinuous deposition has been reported (Felder 1997; Vellekoop et al. In prep.). However, given the expected aeolian origin of the terrigenous components of the micritic limestone near Gubbio, which also reflects astronomically forced changes of the paleoclimate (Sinnesael et al., 2018, 2016), it would be of high interest to also investigate the Ti/Al signal of this section next to the already investigated MS signal. Alternatively, if the primary origin of the MS signal recorded in the type-Maastrichtian chalk of the Hallembaye section is confirmed, its potential as a proxy for changes in terrigenous input can be further investigated – similar to work carried out by Sinnesael et al. (2016). This way, the implications of late Cretaceous astronomically forced climate change on terrigenous influx into a variety of carbonate environments can be better constrained and understood. This would in turn provide valuable insight in which processes are mechanisms are of local scale, and which are of continental scale.

7.4.4. Stevns-1 core, eastern Denmark

One of the largest, complete Campanian-Maastrichtian chalk successions was obtained in 2005 via core drilling near Stevns Klint in eastern Denmark (Voigt et al. 2012; Thibault et al. 2012), which is situated about 300 km north of Kronsmoor and roughly 700 km north of Hallembaye. These white chalks with intercalated marl intervals, deposited in the Danish Basin during the late Cretaceous, have provided a wealth of insight with regards to chemostratigraphy ($\delta^{13}C$) and biostratigraphy. Via $\delta^{13}C$ events this section was correlated to ODP Hole 762C, which in combination with biostratigraphy, magnetostratigraphy and cyclostratigraphy was astronomically calibrated (Thibault 2012; Vellekoop et al. In prep.). By relating the $\delta^{13}C$-based chemostratigraphy for the Maastrichtian type area by Vellekoop et al. (in prep.) with newly developed astronomical age model for the Vijlen Member and Lixhe 1 Member of the Gulpen Formation, global correlation with type-Maastrichtian succession is made available (Vellekoop et al., In prep.).

7.4.5. Gubbio, Stevns-1 and Hallembaye – Anchoring the Astronomical Timescale

Correlation was carried out by Vellekoop (in prep.) between type-Maastrichtian (Hallembaye and ENCI), Gubbio and Stevns-1 core based on $\delta^{13}C$ chemostratigraphy mainly. This way the Froidmont Horizon, which represents the base of the Vijlen Member at the Kreco quarry, was dated to 70.4 Ma (Vellekoop et al., In prep.). The investigated interval, encompassing about 1.12 Myr, (Fig. 69, red) provides an initial astronomically tuned age model that can later be expanded – allowing for additional anchoring. This way, the age model can be improved to further complete the correlation between the type-Maastrichtian and other sections around the world such as Gubbio and the Stevns-1 core, using an integrated stratigraphic approach.

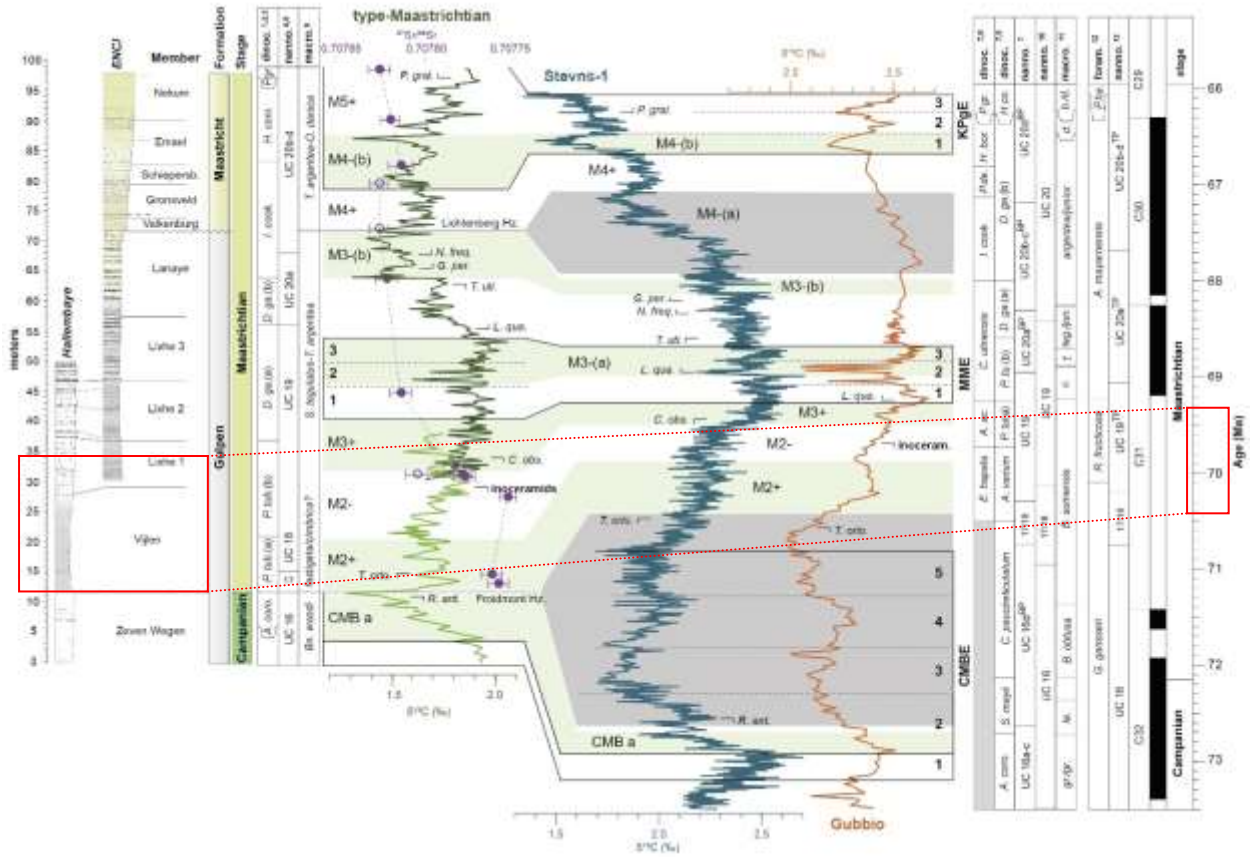

Figure 69: Correlation of upper Campanian–Maastrichtian $\delta^{13}C$ record of the type Maastrichtian to Stevns-1 and Gubbio, adopted from (Vellekoop et al., In prep.). Situated in red is the astronomically tuned interval of the lower part of the Gulpen Formation.

Based on the chemostratigraphical correlation between type-Maastrichtian (Hallembaye/ENCI), the Stevns-1 core and Gubbio, anchoring of the floating astronomical age model for the lower Gulpen Formation was achieved. The astronomically tuned Ti/Al signal, based on observed obliquity cycles, is compared to the bandpass filter applied for frequencies corresponding to short-eccentricity Milankovitch cycle and to the astronomical solutions for short-eccentricity by Laskar et al. (2011) (Fig. 67). The tuned series (based on obliquity cycles) matches well with the bandpass filter and astronomical solution for short-eccentricity (Laskar et al., 2011). Even though 2 small discrepancies (blue boxes) can be observed between the eccentricity band pass filter and the La2011 astronomical solution, this is only of minor concern given the good agreement between the tuned Ti/Al record and the La2011 solution. As can be observed on Fig. 70 (red accolades), 405 kyr metronome may be present in the record but cannot be statistically confirmed due to the limited time it encompasses. Once the dataset is expanded to ~45 m for the Hallembaye section, 405 kyr long-eccentricity cycles may become visible. If so, the astrochronological timescale can be updated and will allow for a correlation of the type-Maastrichtian with other age-equivalent sections around the globe.

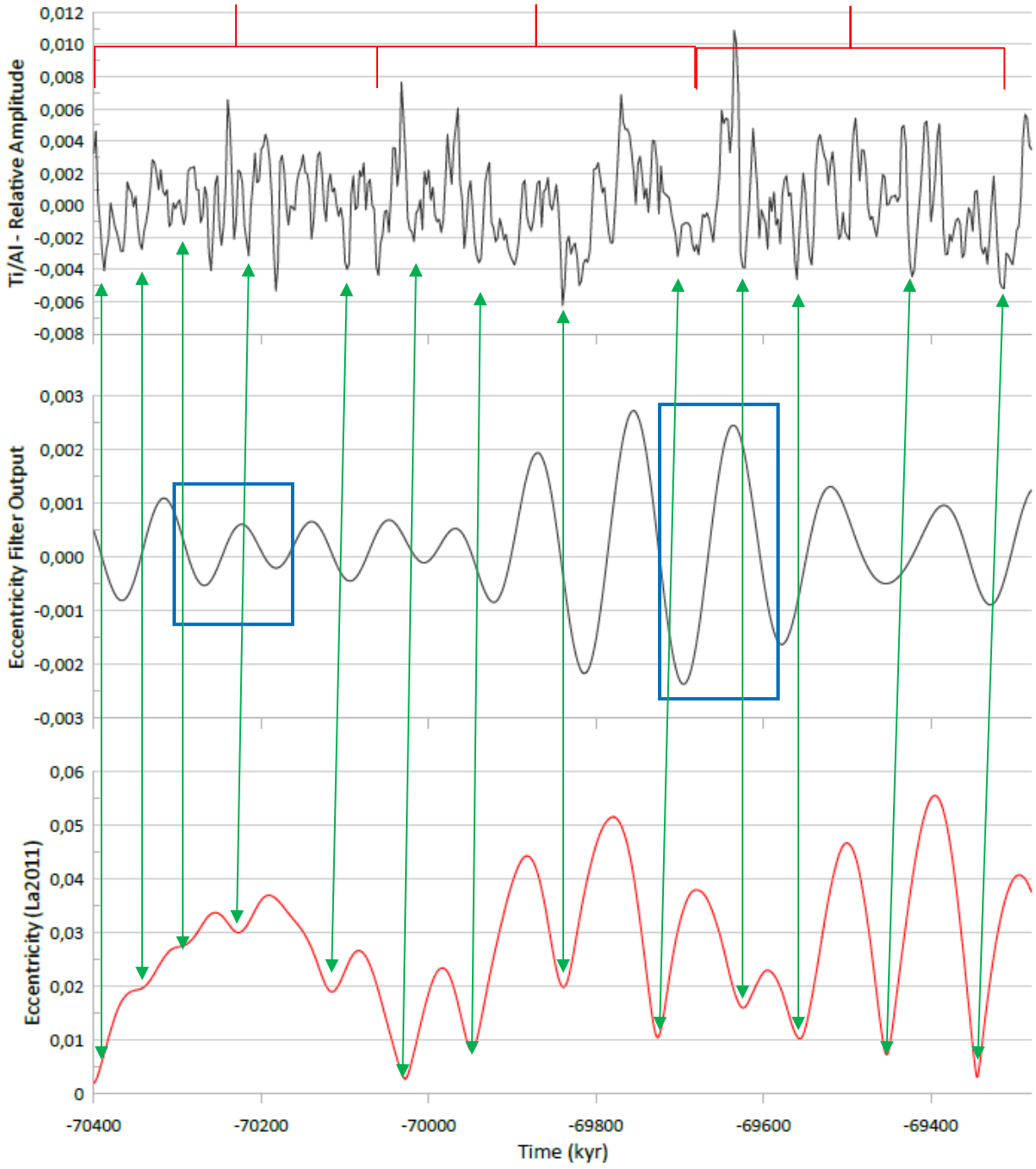

Figure 70: Astronomical solution by Laskar et al. (2011) in red, bandpass output for short-eccentricity as well as astronomically tuned Ti/Al record, Green arrows indicate potential correlation, blue boxes indicate minor discrepancies between bandpass filter output and the astronomical solution La2011, red accolades reveal potential 405 kyr cycles.

8. Conclusions

Multiple dimension with regards to scientific research have been addressed in this master thesis. Insightful learnings were obtained from µXRF methodological assessment and MS methodological finetuning. Analysis of MS and elemental composition of type-Maastrichtian chalk was carried out on depth domain, time domain and frequency domain signals. This way, insight in the paleoclimate and paleoenvironment was obtained and an anchored astronomical timescale was developed for the Vijlen Member and part of the Lixhe 1 Member.

8.1. Methodological Assessments

Micro X-ray fluorescence methodology was briefly assessed by evaluating the impact of beam-size parameters (25 µm versus 200 µm) and sample focusing. In both cases, it can be concluded that consistency is key given the impact of changing µXRF measurement parameters. For future projects aiming at determining bulk elemental composition, it is advised to utilize a defocused X-ray beam to decrease the chance of analyzing just a specific mineral that is not representative of the bulk sample composition. Focusing the X-ray beam on each sample or on each spot has an impact as well, with better accuracy and precision to be expected when focusing on each sample – this however needs to be verified using CRM's. However, focusing on each spot requires a larger amount of time, thus a trade-off should be made. Using a randomly selected sample, HAL18_A_30.85, potential heterogeneity and µXRF repeatability was briefly evaluated as well. In both cases, no statistically significant differences were recorded. Thus, it can be concluded that sample HAL18_A_30.85 can be considered to be homogeneous and that the measurement thereof was precise and repeatable.

Using a 25 µm X-ray beam to analyze one small (powdered and subsampled) rock taken from a huge quarry sounds completely ridiculous. But it works. Micro X-ray fluorescence spectroscopy is able to provide insight in the elemental composition of the type-Maastrichtian chalk in a fast and cost-efficient way. Even more so, it provides insight in changes of the detrital cycle due to astronomical forcing of the paleoclimate (Fig. 1).

Magnetic susceptibility measurement methodology was finetuned for application on type-Maastrichtian chalk. Results obtained from 127 measured chalk samples are in line with all detrital geochemical elements and indicates that MS could serve as a proxy for detrital input of terrigenous material. Even though the primary origin of the MS signal is to be verified, potential lies in the use of MS for cyclostratigraphic applications. This is especially true because MS has already proved to be linked to changes in the detrital input (similar to Ti/Al) into carbonate deposits of the Upper Cretaceous exposed at for example Gubbio (Sinnesael et al., 2016) and Zumaia (Batenburg et al., 2014).

8.2. Type-Maastrichtian Chalk Geochemistry

The extensive geochemical dataset obtained via elemental analysis using micro-X-ray fluorescence provided a wealth of insight in the composition of the type-Maastrichtian chalk and served as the basis for a cyclostratigraphic study attempting to unravel the Late Cretaceous. Elements such as Mg, Sr and Ba that are known to replace Ca in the calcite mineral lattice, display variations in concentrations and have trends different to those of Ca. Links were also established between elements such Si, P and Cr as well as Pb, Al, Ti and Fe (PCA), which might again indicate much potential remains hidden in this dataset.

Therefore, this elements (or ratios thereof) hold potential for further investigation of the type-Maastrichtian chalk geochemistry and could reveal additional insight in the type-Maastrichtian chalk exposed at the Kreco quarry, which in turn could prove useful when attempting to better understand the local Late Cretaceous environment – see Chapter 9 on outlook and recommendations.

Concentrations in $CaCO_3$ and SiO_2 reflect visual observations made based on lithology; pure white chalk contains high amounts of $CaCO_3$, grey chalk contains a substantial amount of Si and other terrigenous elements. A potential link exists between Si concentrations and the occurrence of flint bands, but further investigation in the Lixhe 1 – 3 Members is required to confirm the formulated hypotheses. Furthermore, the transition from the Vijlen Member to the Lixhe 1 Member is characterized by a change in trend of the Ca and Si concentration signal (see appendix 11.4).

Terrigenous elements Al, K and Ti as well as Si, Fe (and the MS signal) displayed similar trends (and positively correlate), which confirms their link with input of detrital materials such as clay minerals from aeolian and/or fluvial origin after being weather and eroded from the land. The Ti/Al recorded primary signals induced via astronomical forcing of the paleoclimate. It reflects changes in composition of detrital material, the provenance thereof or a combination of both (Engelke et al., 2018; Govin et al., 2012). Given changes in detrital cycle seem to be of a continental scale and independent of the setting, use of this proxy at other sections may provide a robust and consistent assessment of astronomically forced changes in the depositional environment.

8.3. Cyclostratigraphy and Anchored Astronomical Timescale

A new, independent astronomical age model for the Vijlen Member and part of the Lixhe 1 Member type-Maastrichtian chalk exposed at the Kreco quarry near Hallembaye was developed. Concentration of $CaCO_3$ (or flint occurrence) as well as the amount of terrigenous elements did not provide insight in potential astronomical forcing of the paleoclimate. Most probably, early diagenetic processes such as flint formation distorted the these primary signal recorded in the type-Maastrichtian chalk. Consequently, preliminary age models based on flint occurrence (Zijlstra 1994; Keutgen 2018) remain questionable. Even though a combination of rhythmically-paced flint cycles, insight in lithology and defined biozones offer preliminary insight in the age of the succession, several arguments have been proposed that indicate these preliminary insights remain but an approximation of the reality as it is at the moment.

As an alternative, the diagenesis-resistant Ti/Al ratio as proxy for terrigenous input (Westphal et al. 2010) was used in a similar cyclostratigraphic approach. Even though small differences in sedimentation rates were recorded when comparing Vijlen Member and part of the Lixhe 1 Member, an average sedimentation rate of about 2 cm/kyr offered enough consistency for preliminary visual identification of obliquity cycles (see Fig. 51). Milankovitch obliquity cycles were further identified and confirmed in the record using spectral and time series analyses. Furthermore, additional analyses revealed the presence of precession and short-eccentricity cyclicity as well (Fig. 65). Identification of 3 Milankovitch cycles provide sufficient confidence of astronomical forcing, as proposed by Waltham (2015). Even more so, a potential 4^{th} cycle – the 405 kyr metronome – may be present as well, but cannot be confirmed at this point (see Fig. 70).

For the interval ranging from a stratigraphic height of 11.75 m to 34.50 m at the Kreco quarry, an independent floating astronomical timescale was constructed encompassing ~1.12 Myr based on identified obliquity Milankovitch cycles (Fig. 64). Compared to other sections mentioned in Chapter 7.4, the type-Maastrichtian record at the Kreco quarry is incomplete. Most probably, this is due to changes in eustatic sea level which led to a decrease in sedimentation or even erosion at the Campanian-Maastrichtian boundary (Vellekoop et al., In prep.). These observations imply that, compared to e.g. the Kronsmoor formation which was deposited in a 50 m – 200 m Chalk Sea (Engelke et al. 2018), the depositional setting of the type-Maastrichtian was slightly different and sea water levels are estimated to be slightly lower.

Based on astronomically tuned records such as Gubbio (Voigt et al. 2012; Sinnesael et al. 2016; Sinnesael et al. 2019) and the Stevns-1 core (Voigt et al. 2012; Thibault et al. 2012) correlation based on chemostratigraphy for the type-Maastrichtian (Kreco/ENCI) was carried out by Vellekoop et al. (in prep.). This framework allowed for anchoring of the floating astronomical timescale to the onset of the Vijlen Member at 70.4 Ma. The investigated interval was deposited from 70.40 Ma to roughly 69.25 Ma in the Late Cretaceous Chalk Sea. Comparison of the tuned Ti/Al record with the La2011 astronomical eccentricity solution reveals a large similarity, further reinforcing previous conclusions made.

Finally, it can be concluded that the preliminary age models by Zijlstra, Felder and Keutgen (and others) for the type-Maastrichtian provided a good initial foundation. However, the newly developed astrochronological time scale which is based on cyclostratigraphy (this work), biostratigraphy and chemostratigraphy and correlation with Gubbio and Stevns-1 (Vellekoop et al., In prep.) provides an improved age model for the type-Maastrichtian Gulpen Formation enclosed at the Kreco quarry. This new timescale will be extended and will therefore become better for correlation with other Upper Cretaceous sections. This way, more insight will be obtained on regional versus continental or even global variations.

9. Outlook and Recommendations

From a methodological point of view, it is recommended to maintain consistency of measurement parameters. However, if at any point changes would be made to the existing standard operating procedures, use of a larger micro X-ray beam size for the determination of bulk elemental composition is recommended. Further methodological assessment might further increase confidence that can be put in data. For example, it might be of added value to assess sample homogeneity on a larger selection of samples using µXRF or MS. In addition, it would be very interesting to assess homogeneity of the exposed lithostratigraphy at Kreco and other quarries.

Much potential may remain hidden in the extensive geochemical dataset that was gathered for this research given focus was put on elements such as Si and Ca as well as terrigenous elements such as K, Ti and Al. Other elements and/or element ratios included in this dataset are readily available for analysis and might provide even more insight in the type-Maastrichtian geochemistry. For example, so-called paleoproductivity proxies may reflect changes in the bio-productivity due to variations in the paleoclimate (Brumsack, 2006). Given the strong indication of astronomical forcing of the paleoclimate, so-called paleoproductivity proxies might have recorded the primary, astronomically forced signal. Several proxies can be utilized as a measure for the paleoproductivity, such as P/Al (general marine productivity), Sr/Al (carbonate bioproductivity) (Engelke et al., 2018) as well as Sr/Ca (coccolithophorids productivity) (Engelke et al., 2018; Waite et al., 2008) and Excess Si_{xs} (biogenic silica) (Brumsack, 2006). Aside from Ti/Al as a proxy for terrigenous input into the carbonate, several other proxies based on geochemical elemental ratios have been proposed. Si/Al ratio serves as a proxy of aeolian dust input, Mg/Al as a sensitive dust proxy (Schnetger et al., 2000) and K/Al was already used as a proxy for illite content (Hofer et al., 2013). The amount of terrigenous matter in biogenic sediments can be estimated based on Ti elemental concentrations (Murray et al., 2000), based on the formula %terrigenous = (Ti_{sample}/Ti_{shale}) * 100, with the European average Ti_{shale} value 4010 ppm (Engelke et al., 2018). Given the overall similarities between Kronsmoor chalk as characterized by Engelke et al (2018), Ti/Al, Mg/Al and K/Al would serve as ideal proxies for terrigenous input to the Hallembaye chalk.

In order to further constrain potential uncertainties, the anchored astronomical timescale should be expanded – both vertically for the complete section exposed at the Kreco quarry as well as laterally. In case vertical expansion of the Gulpen Formation age model is carried out (e.g. up to a stratigraphic height of ~45 m), potential presence of the 405 kyr long-eccentricity cycle or “metronome” should be investigated. Lateral expansions would imply correlation with other sections of the type-Maastrichtian in the vicinity of Maastricht as well as other age-equivalent sections such as Gubbio, Zumaia and the Stevns-1 core. This would not only be of added value to the community, but will no doubt provide insight in the Late Cretaceous climate, environment and depositional setting.

With perspective to further cyclostratigraphic studies on type-Maastrichtian chalk, it has been demonstrated that sampling resolution of 5 cm is of high value, but not an absolute requirement. Provided no drastic changes in sedimentation rates are expected, a sampling resolution of 10 cm should be sufficient. The shortest interpreted astronomical cycle (~20 kyr precession cycle) has a thickness of roughly 40 cm at an average sedimentation rate of 2 cm/kyr. Only if sedimentation rates were to decrease to values of 1 cm/kyr or below, the precession cycle (< ~20 cm thick) cannot be determined at a sample resolution of 10 cm (Nyquist theorem) (Vaidyanathan, 2001; Weedon, 2003).

10. References

Agico, 2018. Agico MFK2 User Manual.

Anderskouv, K., Surlyk, F., 2011. Upper Cretaceous chalk facies and depositional history recorded in the Mona-1 core, Mona Ridge, Danish North Sea. Geol. Surv. Den. Greenl. GEUS Bull. 25, 1–60. https://doi.org/10.34194/geusb.v25.4731

Batenburg, S.J., Gale, A.S., Sprovieri, M., Hilgen, F.J., Thibault, N., Boussaha, M., Orue-Etxebarria, X., 2014. An astronomical time scale for the Maastrichtian based on the Zumaia and Sopelana sections (Basque country, northern Spain). J. Geol. Soc. 171, 165–180. https://doi.org/10.1144/jgs2013-015

Berger, A., Loutre, M.F., 1992. Astronomical solutions for paleoclimate studies over the last 3 million years. Earth Planet. Sci. Lett. 111, 369–382.

Boggs, S., 2006. Principles of Sedimentology and Stratigraphy, Fourth Edition. ed. Pearson Education, Inc.

Boulila, S., Vahlenkamp, M., De Vleeschouwer, D., Laskar, J., Yamamoto, Y., Pälike, H., Kirtland Turner, S., Sexton, P.F., Westerhold, T., Röhl, U., 2018. Towards a robust and consistent middle Eocene astronomical timescale. Earth Planet. Sci. Lett. 486, 94–107. https://doi.org/10.1016/j.epsl.2018.01.003

Brand, U., Morrison, J.O., Campbell, I.T., 1998. Strontium in Sedimentary Rocks. Geochemistry 600–603. https://doi.org/10.1007/1-4020-4496-8_301

Bro, R., Smilde, A.K., 2014. Principal component analysis. Anal. Methods 6, 2812–2831. https://doi.org/10.1039/c3ay41907j

Bruker, 2015. M4 Tornado.

Brumsack, H.-J., 2006. The trace metal content of recent organic carbon-rich sediments: Implications for Cretaceous black shale formation. Palaeogeogr. Palaeoclimatol. Palaeoecol. 232, 344–361. https://doi.org/10.1016/j.palaeo.2005.05.011

Chambers, J., 2021. What is R? [WWW Document]. URL https://www.r-project.org/about.html (accessed 5.25.21).

Chiarenza, A.A., Farnsworth, A., Mannion, P.D., Lunt, D.J., Valdes, P.J., Morgan, J.V., Allison, P.A., 2020. Asteroid impact, not volcanism, caused the end-Cretaceous dinosaur extinction. Proc. Natl. Acad. Sci. 117, 17084–17093. https://doi.org/10.1073/pnas.2006087117

da Silva, A.-C., De Vleeschouwer, D., Boulvain, F., Claeys, P., Fagel, N., Humblet, M., Mabille, C., Abadi Sardar, M., Pas, D., Dekkers, M.J., Michel, J., 2013. Magnetic susceptibility as a high-resolution correlation tool and as a climatic proxy in Paleozoic rocks e Merits and pitfalls: Examples from the Devonian in Belgium. Mar. Pet. Geol. 46, 173–189. https://doi.org/10.1016/j.marpetgeo.2013.06.012

da Silva, A.-C., Dekkers, M.J., Mabille, C., Boulvain, F., 2012. Magnetic susceptibility and its relationship with paleoenvironments, diagenesis and remagnetization: examples from the Devonian carbonates of Belgium. Stud. Geophys. Geod. 56, 677–704. https://doi.org/10.1007/s11200-011-9005-9

da Silva, A.-C., Potma, K., Weissenberger, J.A.W., Whalen, M.T., Humblet, M., Mabille, C., Boulvain, F., 2009. Magnetic susceptibility evolution and sedimentary environments on carbonate platform sediments and atolls, comparison of the Frasnian from Belgium and Alberta, Canada. Sediment. Geol. 214, 3–18. https://doi.org/10.1016/j.sedgeo.2008.01.010

da Silva, A.-C., Whalen, M.T., Hladil, J., Chadimova, L., Chen, D., Spassov, S., Boulvain, F., Devleeschouwer, X., 2015. Magnetic susceptibility application: a window onto ancient environments and climatic variations: foreword. Geol. Soc. Lond. 414, 1–13. https://doi.org/10.1144/SP414.12

de Winter, N.J., Sinnesael, M., Makarona, C., Vansteenberge, S., Claeys, P., 2017. Trace element analysis of carbonates using portable and micro-X-ray fluorescence: Performance and optimization of measurement parameters and strategies. J. Anal. At. Spectrom. 28. https://doi.org/10.1039/C6JA00361C

Dinarès-Turell, J., Martinez-Braceras, N., Payros, A., 2018. High-Resolution Integrated Cyclostratigraphy From the Oyambre Section (Cantabria, N Iberian Peninsula): Constraints for Orbital Tuning and Correlation of Middle Eocene Atlantic Deep-Sea Records. Geochem. Geophys. Geosystems 21. https://doi.org/10.1002/2017GC007367

Dressing, C.D., Spiegel, D.S., Scharf, C.A., Menou, K., Raymond, S.N., 2010. Habitable Climates: The Influence of Eccentricity. Astrophys. J. 721, 1295–1307. https://doi.org/10.1088/0004-637X/721/2/1295

Ellwood, B.B., Crick, R.E., 2000. Magnetosusceptibility event and cyclostratigraphy method applied to marine rocks: Detrital input versus carbonate productivity 5.

Ellwood, B.B., MacDonald, W.D., Wheeler, C., Benoist, S.L., 2003. The K-T boundary in Oman: identifed using magnetic susceptibility ¢eld measurements with geochemical confrmation. Earth Planet. Sci. Lett. 206, 529–540. https://doi.org/10.1016/S0012-821X(02)01124-X

Elskens, M., 2019. Chemometrics: Multivariate Analysis.

Engelke, J., Linnert, C., Niebuhr, B., Schnetger, B., Brumsack, H.-J., Mutterlose, J., Wilmsen, M., 2018. Tracking Late Cretaceous environmental change: Geochemical environment of the upper Campanian to lower Maastrichtian chalks at Kronsmoor, northern Germany. Cretac. Res. 84, 323–339. https://doi.org/10.1016/j.cretres.2017.10.001

Fantle, M.S., Barnes, D.B., Lau, K.V., 2020. The Role of Diagenesis in Shaping the Geochemistry of the Marine Carbonate Record. Annu. Rev. Earth Planet. Sci. 48, 549–583. https://doi.org/10.1146/annurev-earth-073019- 060021

Felder, P.J.S., 1997. The Vijlen Chalk Member (Maastrichtian, Late Cretaceous) in the Meuse-Rhine Euregion. Ann. Société Géologique Belg. 119, 119–133.

Felder, P.J.S., 1996. Late Cretaceous (Santonian-Maastrichtian) Sedimentation Rates in the Maastricht (NL), Liège/Campine (B) and Aachen (D) Area. Ann. Société Géologique Belg. 117, 311–319.

Felder, P.J.S., Bless, M.J.M., 1994. The Vijlen Chalk (Early Early to Early Late Maastrichtian) in its type area around Vijlen and Mamelis (Southern Limburg, The Netherlands). Ann. Société Géologique Belg. 116, 61–85.

Felder, P.J.S., Keppens, E., Declercq, B., Normand, S., Streel, M., 2003. Faunal/floral and isotopic responses to Milankovitch precession cycles and environmental changes in the upper Gulpen Formation (Upper Maastrichtian) at the CBR-Lixhe and ENCI-Maastricht bv quarries. Neth. J. Geosci. Geol. En Mijnb. 82, 275–281.

Felder, W.M., 1983. De kalksteengroeve van de cementfabriek Ciments Portland Liegeois bij Halembaye, gem. Visé, prov. Luik, België. Grondboor En Hamer 5, 122–138.

Folk, R.L., 1959. Practical Petrographic Classification of Limestones. Bull. Am. Assoc. Pet. Geol. 43, 38.

Font, E., Adatte, T., Andrade, M., Keller, G., Mbabi Bitchong, A., Carvallo, C., Ferreira, J., Diogo, Z., Mirão, J., 2018. Deccan volcanism induced high-stress environment during the Cretaceous–Paleogene transition at Zumaia, Spain: Evidence from magnetic, mineralogical and biostratigraphic records. Earth Planet. Sci. Lett. 484, 53–66. https://doi.org/10.1016/j.epsl.2017.11.055

Friedman, G.M., 1996. Chapter 8 Chalk Reservoirs. Dev. Pet. Sci. 44, 773–795. https://doi.org/10.1016/S0376-7361(96)80030-6

Gallagher, W.B., Jagt, J.W.M., Mulder, E.W.A., Schulp, A.S., 2004. A New Mosasour Speciment from Maastricht (The Netherlands), with a Review of the Late Cretaceous-Early Paleogene Marine Faunas of New Jersey and Limburg. The Mosasaur 7, 47–57.

Gao, Y., 2019. Aquatic Carbon Cycle and the Biological Pump.

Goderis, S., Sato, H., Ferrière, L., Schmitz, B., Burney, D., Kaskes, P., Vellekoop, J., Wittmann, A., Schulz, T., Chernonozhkin, S.M., Claeys, P., de Graaff, S.J., Déhais, T., de Winter, N.J., Elfman, M., Feignon, J.-G., Ishikawa, A., Koeberl, C., Kristiansson, P., Neal, C.R., Owens, J.D., Schmieder, M., Sinnesael, M., Vanhaecke, F., Van Malderen, S.J.M., Bralower, T.J., Gulick, S.P.S., Kring, D.A., Lowery, C.M., Morgan, J.V., Smit, J., Whalen, M.T., IODP-ICDP Expedition 364 Scientists, 2021. Globally distributed iridium layer preserved within the Chicxulub impact structure. Sci. Adv. 7, 1–13. https://doi.org/10.1126/sciadv.abe3647

Govin, A., Holzwarth, U., Heslop, D., Keeling, L.F., Zabel, M., Mulitza, S., Collins, J.A., Chiessi, C.M., 2012. Distribution of major elements in Atlantic surface sediments (36°N–49°S): Imprint of terrigenous input and continental weathering. Geochem. Geophys. Geosystems 13, 1–23. https://doi.org/10.1029/2011GC003785

Gradstein, F.M., Ogg, J.G., 2020. The Chronostratigraphic Scale, in: Geologic Time Scale 2020. Elsevier, pp. 21–32. https://doi.org/10.1016/B978-0-12-824360-2.00002-4

Håkansson, E., Bromley, R., Perch-Nielsen, K., 1974. Maastrichtian Chalk of North-West Europe-a Pelagic Shelf Sediment, in: Hsü, K.J., Jenkyns, H.C. (Eds.), Pelagic Sediments: On Land and under the Sea. Blackwell Publishing Ltd., Oxford, UK, pp. 211–233. https://doi.org/10.1002/9781444304855.ch9

Hancock, J.M., 1975. The petrology of the Chalk. Proc. Geol. Assoc. 86, 499–535.

Hays, J.D., Imbrie, J., Shackleton, N.J., 1976. Variations in the Earth's Orbit: Pacemaker of the Ice Ages 194, 1121–1132.

Hilgen, F.J., Hinnov, L.A., Abdul Aziz, H., Abels, H.A., Batenburg, S., Bosmans, J.H.C., de Boer, B., Hüsing, S.K., Kuiper, K.F., Lourens, L.J., Rivera, T., Tuenter, E., Van de Wal, R.S.W., Wotzlaw, J.-F., Zeeden, C., 2015. Stratigraphic continuity and fragmentary sedimentation: the success of cyclostratigraphy as part of integrated stratigraphy. Geol. Soc. Lond. Spec. Publ. 404, 157–197. https://doi.org/10.1144/SP404.12

Hilgen, F.J., Kuiper, K.F., Lourens, L.J., 2010. Evaluation of the astronomical time scale for the Paleocene and earliest Eocene. Earth Planet. Sci. Lett. 300, 139–151. https://doi.org/10.1016/j.epsl.2010.09.044

Hinnov, L.A., 2018. Cyclostratigraphy and Astrochronology in 2018, in: Stratigraphy & Timescales. Elsevier, pp. 1–80. https://doi.org/10.1016/bs.sats.2018.08.004

Hinnov, L.A., 2013. Cyclostratigraphy and its revolutionizing applications in the earth and planetary sciences. Geol. Soc. Am. Bull. 125, 1703–1734. https://doi.org/10.1130/B30934.1

Hofer, G., Wagreich, M., Neuhuber, S., 2013. Geochemistry of fine-grained sediments of the upper Cretaceous to Paleogene Gosau Group (Austria, Slovakia): Implications for paleoenvironmental and provenance studies. Geosci. Front. 4, 449–468. https://doi.org/10.1016/j.gsf.2012.11.009

Huber, B.T., Norris, R.D., 2002. Deep-sea paleotemperature record of extreme warmth during the Cretaceous. Geol. Soc. Am. 30, 123–126.

Huygh, J., 2019. Geochemical study on Maastrichtian chalk New insights into cyclostratigraphy by using stable isotopes (δ13C and δ18O) and elemental analysis. Vrije Universiteit Brussel (VUB).

IUPAC, 2019. Compendium of Chemical Technology Gold Book, 2nd ed. Blackwell Scientific Publications, Oxford.

Jagt, J.W.M., Jagt-Yazykova, E.A., 2012. Stratigraphy of the type Maastrichtian – a synthesis 5–32.

Jagt, J.W.M., Schulp, A.S., de Graaf, D.T., 2003. The 150th anniversary of the Maastrichtian Stage - a celebratory conference: Introduction. Neth. J. Geosci. - Geol. En Mijnb. 82, 223–224. https://doi.org/10.1017/S0016774600020801

Jurkowska, A., Świerczewska-Gładysz, E., 2020. Evolution of Late Cretaceous Si cycling reflected in the formation of siliceous nodules (flints and cherts). Glob. Planet. Change 195, 103334. https://doi.org/10.1016/j.gloplacha.2020.103334

Kaskes, P., Déhais, T., de Graaff, S.J., Goderis, S., Claeys, P., 2021. Micro–X-ray fluorescence (µXRF) analysis of proximal impactites: High-resolution element mapping, digital image analysis, and quantifications. Geol. Soc. Am. Special Paper 550, 1–36. https://doi.org/10.1130/2021.2550(07).

Keutgen, N., 2018. A bioclast-based astronomical timescale for the Maastrichtian in the type area (southeast Netherlands, northeast Belgium) and stratigraphic implications: the legacy of P.J. Felder. Neth. J. Geosci. 97, 229–260. https://doi.org/10.1017/njg.2018.15

Keutgen, N., Jagt, J.W.M., Felder, P.J., Jagt-Yazykova, E.A., 2010. Stratigraphy of the upper Vijlen Member (Gulpen Formation; Maastrichtian) in northeast Belgium, the southeast Netherlands and the Aachen area (Germany), with special reference to belemnitellid cephalopods. Neth. J. Geosci. - Geol. En Mijnb. 89, 109–136. https://doi.org/10.1017/S0016774600000731

Kodama, K.P., Hinnov, L.A., 2015. Rock Magnetic Cyclostratigraphy, First Edition. ed. John Wiley & Sons, Ltd.

Koutsoukos, E.A.M., Hart, M.B., 1990. Radiolarians and Diatoms from the mid-Cretaceous Successions of the Sergipe Basin, Northeastern Brazil: palaeoceanographic Assessment. J. Micropalaeontology 9, 45–63. https://doi.org/10.1144/jm.9.1.45

Laskar, J., Gastineau, M., Delisle, J.-B., Farrés, A., Fienga, A., 2011. Strong chaos induced by close encounters with Ceres and Vesta. Astron. Astrophys. 532, L4. https://doi.org/10.1051/0004-6361/201117504

Laskar, J., Robutel, P., Joutel, F., Gastineau, M., Correia, A.C.M., Levrard, B., 2004. A long-term numerical solution for the insolation quantities of the Earth. Astron. Astrophys. 428, 261–285. https://doi.org/10.1051/0004-6361:20041335

Levrard, B., Laskar, J., 2003. Climate friction and the Earth's obliquity. Geophys. J. Int. 154, 970–990. https://doi.org/10.1046/j.1365-246X.2003.02021.x

Leys, C., Ley, C., Klein, O., Bernard, P., Licata, L., 2013. Detecting outliers: Do not use standard deviation around the mean, use absolute deviation around the median. J. Exp. Soc. Psychol. 49, 764–766. https://doi.org/10.1016/j.jesp.2013.03.013

Lindgreen, H., Drits, V.A., Salyn, A.L., Jakobsen, F., Springer, N., 2011. Formation of flint horizons in North Sea chalk through marine sedimentation of nano-quartz. Clay Miner. 46, 525–537. https://doi.org/10.1180/claymin.2011.046.4.525

Marshak, S., 2008. Earth Portrait of a Planet, Third. ed. W. W. Norton & Company, Inc.

Meyers, S.R., 2019. Cyclostratigraphy and the problem of astrochronologic testing. Earth-Sci. Rev. 190, 190–223. https://doi.org/10.1016/j.earscirev.2018.11.015

Meyers, S.R., 2015. The evaluation of eccentricity-related amplitude modulation and bundling in paleoclimate data: An inverse approach for astrochronologic testing and time scale optimization: ASTROCHRONOLOGIC TESTING AND OPTIMIZATION. Paleoceanography 30, 1625–1640. https://doi.org/10.1002/2015PA002850

Meyers, S.R., 2012. Seeing red in cyclic stratigraphy: Spectral noise estimation for astrochronology: SEEING RED IN CYCLIC STRATIGRAPHY. Paleoceanography 27, n/a-n/a. https://doi.org/10.1029/2012PA002307

Meyers, S.R., Sageman, B.B., Hinnov, L.A., 2001. Integrated Quantitative Stratigraphy of the Cenomanian-Turonian Bridge Creek Limestone Member Using Evolutive Harmonic Analysis and Stratigraphic Modeling. J. Sediment. Res. 71, 628–644. https://doi.org/10.1306/012401710628

Murray, R.W., Knowlton, C., Leinen, M., Mix, A.C., Polsky, C.H., 2000. Export production and terrigenous matter in the Central Equatorial Pacific Ocean during interglacial oxygen isotope Stage 11. Glob. Planet. Change 24, 59–78. https://doi.org/10.1016/S0921-8181(99)00066-1

Nohl, T., Steinbauer, M.J., Sinnesael, M., Jarochowska, E., 2021. Detecting initial aragonite and calcite variations in limestone–marl alternations. Sedimentology sed.12885. https://doi.org/10.1111/sed.12885

Noir, J. Earth's Precession [WWW Document]. Cyclostratigraphy Intercomp. Proj. URL https://www.cyclostratigraphy.org/figure-repository (accessed 5.25.21).

Pälike, H., 2005. EARTH | Orbital Variation (Including Milankovitch Cycles), in: Encyclopedia of Geology. Elsevier, pp. 410–421. https://doi.org/10.1016/B0-12-369396-9/00123-4

Percival, D.B., Walden, A.T., 1993. Spectral Analysis for Physical Applications: Multitaper and Conventional Univariate Techniques.

Prieto, G.A., Parker, R.L., Vernon III, F.L., 2009. A Fortran 90 library for multitaper spectrum analysis. Comput. Geosci. 35, 1701–1710. https://doi.org/10.1016/j.cageo.2008.06.007

Renne, P.R., Karner, D.B., Ludwig, K.R., 1998. Absolute Ages Aren't Exactly. Science 282, 1840–1841. https://doi.org/10.1126/science.282.5395.1840

Robaszynski, F., Bless, M.J.M., Felder, P.J.S., Foucher, J.-C., Legoux, O., Manivit, H., Meessen, J.P.M.T., Van Der Tuuk, L.A., 1985. The Campanian-Maastrichtian boundary in the chalky facies close to the type-Maastrichtian area. Bull. Cent. Rech. Explor.-Prod. Elf-Aquitaine 9, 1–113.

Rosenzweig, C., Neofotis, P., 2013. Detection and attribution of anthropogenic climate change impacts: Anthropogenic climate change impacts. Wiley Interdiscip. Rev. Clim. Change 4, 121–150. https://doi.org/10.1002/wcc.209

Rousseau, R.M., 2004. Some considerations on how to solve the Sherman equation in practice. Spectrochim. Acta Part B At. Spectrosc. 59, 1491–1502. https://doi.org/10.1016/j.sab.2004.06.002

Rousseeuw, P.J., Croux, C., 1993. Alternatives to the Median Absolute Deviation. J. Am. Stat. Assoc. 88, 1273–1283. https://doi.org/10.1080/01621459.1993.10476408

Rubincam, D.P., 2004. The Precession Index, A Nonlinear Energy Balance Model, And Seversmith Psychroterms.

Schnetger, B., Brumsack, H.-J., Schale, H., Hinrichs, J., Dittert, L., 2000. Geochemical characteristics of deep-sea sediments from the Arabian Sea: a high-resolution study. Deep Sea Res. Part II Top. Stud. Oceanogr. 47, 2735–2768. https://doi.org/10.1016/S0967-0645(00)00047-3

Schuster, A., 1898. On the investigation of hidden periodicities with application to a supposed 26 day period of meteorological phenomena. J. Geophys. Res. 3, 13. https://doi.org/10.1029/TM003i001p00013

Sinnesael, M., De Vleeschouwer, D., Coccioni, R., Claeys, P., Frontalini, F., Jovane, L., Savian, J.F., Montanari, A., 2016. High-resolution multiproxy cyclostratigraphic analysis of environmental and climatic events across the Cretaceous-Paleogene boundary in the classic pelagic succession of Gubbio (Italy), in: Geological Society of America Special Papers. Geological Society of America, pp. 115–137. https://doi.org/10.1130/2016.2524(09)

Sinnesael, M., De Vleeschouwer, D., Zeeden, C., Batenburg, S.J., Da Silva, A.C., de Winter, N.J., Dinarès-Turell, J., Drury, A.J., Gambacorta, G., Hilgen, F.J., Hinnov, L.A., Hudson, A.J.L., Kemp, D.B., Lantink, M.L., Laurin, J., Li, M., Liebrand, D., Ma, C., Meyers, S.R., Monkenbusch, J., Montanari, A., Nohl, T., Pälike, H., Pas, D., Ruhl, M., Thibault, N., Vahlenkamp, M., Valero, L., Wouters, S., Wu, H., Claeys, P., 2019a. The Cyclostratigraphy Intercomparison Project (CIP): consistency, merits and pitfalls. Earth-Sci. Rev. 199, 102965. https://doi.org/10.1016/j.earscirev.2019.102965

Sinnesael, M., de Winter, N.J., Snoeck, C., Montanari, A., Claeys, P., 2018. An integrated pelagic carbonate multi-proxy study using portable X-ray fluorescence (pXRF): Maastrichtian strata from the Bottaccione Gorge, Gubbio, Italy. Cretac. Res. 91, 20–32. https://doi.org/10.1016/j.cretres.2018.04.010

Sinnesael, M., Montanari, A., Frontalini, F., Coccioni, R., Gattacceca, J., Snoeck, C., Wegner, W., Koeberl, C., Morgan, L.E., de Winter, N.J., DePaolo, D.J., Claeys, P., 2019b. Multiproxy Cretaceous-Paleogene oundary event stratigraphy: An Umbria-Marche basinwide perspective. Geol. Soc. Am. Special Paper 542, 133–158. https://doi.org/10.1130/2019.2542(07)

Stage, M., 2001. Magnetic susceptibility as carrier of a climatic signal in chalk. Earth Planet. Sci. Lett. 188, 17–27. https://doi.org/10.1016/S0012-821X(01)00304-1

Stage, M., 1999. Signal analysis of cyclicity in Maastrichtian pelagic chalks from the Danish North Sea. Earth Planet. Sci. Lett. 173, 75–90. https://doi.org/10.1016/S0012-821X(99)00213-7

Strasser, A.H., Heckel, P.H., Hilgen, F., 2006. Cyclostratigraphy concepts, definitions, and applications. Newsl. Stratigr. 42, 75–114. https://doi.org/10.1127/0078-0421/2006/0042-0075

Surlyk, F., Rasmussen, S.L., Boussaha, M., Schiøler, P., Schovsbo, N.H., Sheldon, E., Stemmerik, L., Thibault, N., 2013. Upper Campanian–Maastrichtian holostratigraphy of the eastern Danish Basin. Cretac. Res. 46, 232–256. https://doi.org/10.1016/j.cretres.2013.08.006

Swart, P.K., 2015. The geochemistry of carbonate diagenesis: The past, present and future. Sedimentology 62, 1233–1304. https://doi.org/10.1111/sed.12205

ten Kate, W.G.H.Z., Sprenger, A., 1993. Orbital cyclicities above and below the Cretaceous/Paleogene boundary at Zumaya (N Spain), Agost and Relleu (SE Spain). Sediment. Geol. 87, 69–101. https://doi.org/10.1016/0037-0738(93)90037-6

Thibault, N., Harlou, R., Schovsbo, N., Schiøler, P., Minoletti, F., Galbrun, B., Lauridsen, B., Sheldon, E., Stemmerik, L., Surlyk, F., 2012a. Upper Campanian–Maastrichtian nannofossil biostratigraphy and high-resolution carbon-isotope stratigraphy of the Danish Basin: Towards a standard δ13C curve for the Boreal Realm. Cretac. Res. 33, 72–90. https://doi.org/10.1016/j.cretres.2011.09.001

Thibault, N., Harlou, R., Schovsbo, N.H., Stemmerik, L., Surlyk, F., 2016. Late Cretaceous (late Campanian–Maastrichtian) sea-surface temperature record of the Boreal Chalk Sea. Clim. Past 12, 429–438. https://doi.org/10.5194/cp-12-429-2016

Thibault, N., Husson, D., Harlou, R., Gardin, S., Galbrun, B., Huret, E., Minoletti, F., 2012b. Astronomical calibration of upper Campanian–Maastrichtian carbon isotope events and calcareous plankton biostratigraphy in the Indian Ocean (ODP Hole 762C): Implication for the age of the Campanian–Maastrichtian boundary. Palaeogeogr. Palaeoclimatol. Palaeoecol. 337–338, 52–71. https://doi.org/10.1016/j.palaeo.2012.03.027

Thomson, D.J., 1982. Spectrum estimation and harmonic analysis. Proc. IEEE 70, 1055–1096. https://doi.org/10.1109/PROC.1982.12433

Uo, M., Wada, T., Sugiyama, T., 2015. Applications of X-ray fluorescence analysis (XRF) to dental and medical specimens. Jpn. Dent. Sci. Rev. 51, 2–9. https://doi.org/10.1016/j.jdsr.2014.07.001

Vaidyanathan, P.P., 2001. Generalizations of the sampling theorem: Seven decades after Nyquist. IEEE Trans. Circuits Syst. Fundam. Theory Appl. 48, 1094–1109. https://doi.org/10.1109/81.948437

Van Os, B.J.H., Lourens, L.J., Hilgen, F.J., De Lange, G.J., Beaufort, L., 1994. The formation of Pliocene sapropels and carbonate cycles in the Mediterranean: Diagenesis, dilution, and productivity. Paleoceanography 9, 601–617. https://doi.org/10.1029/94PA00597

Vellekoop, J., 2019. The Maastrichtian Geoheritage Project: an introduction, first results and outlook.

Vellekoop, J., Kaskes, P., Sinnesael, M., Déhais, T., Huygh, J., Jagt, J.W.M., Speijer, R.P., Claeys, P., In prep. A new age model and chemostratigraphic framework for the Maastrichtian type area (southeastern Netherlands, northeastern Belgium) In prep.

Vincze, L., 2021. X-ray Fluorescence.

Voigt, S., Gale, A.S., Jung, C., Jenkyns, H.C., 2012. Global correlation of Upper Campanian - Maastrichtian successions using carbon-isotope stratigraphy: development of a new Maastrichtian timescale. Newsl. Stratigr. 45, 25–53. https://doi.org/10.1127/0078-0421/2012/0016

Voigt, S., Schönfeld, J., 2010. Cyclostratigraphy of the reference section for the Cretaceous white chalk of northern Germany, Lägerdorf–Kronsmoor: A late Campanian–early Maastrichtian orbital time scale. Palaeogeogr. Palaeoclimatol. Palaeoecol. 287, 67–80. https://doi.org/10.1016/j.palaeo.2010.01.017

Waite, A.J., Gibbs, S.J., Diester-Haass, L., Rickaby, R.E.M., Billups, K., 2008. A top-down and bottom-up comparison of paleoproductivity proxies: Calcareous nannofossil Sr/Ca ratios and benthic foraminiferal accumulation rates: COMPARISON OF PALEOPRODUCTIVITY PROXIES. Geochem. Geophys. Geosystems 9, n/a-n/a. https://doi.org/10.1029/2007GC001812

Waltham, D., 2015. Milankovitch Period Uncertainties and Their Impact On Cyclostratigraphy. J. Sediment. Res. 85, 990–998. https://doi.org/10.2110/jsr.2015.66

Weedon, G., 2003. Time Series Analysis and Cyclostratigraphy, First Edition. ed. Cambridge University Press.

Westphal, H., Hilgen, F., Munnecke, A., 2010. An assessment of the suitability of individual rhythmic carbonate successions for astrochronological application. Earth-Sci. Rev. 99, 19–30. https://doi.org/10.1016/j.earscirev.2010.02.001

Wilmsen, M., Niebuhr, B., Hiss, M., 2005. The Cenomanian of northern Germany: facies analysis of a transgressive biosedimentary system. Facies 51, 242–263. https://doi.org/10.1007/s10347-005-0058-5

Winter, N.J., Goderis, S., Van Malderen, S.J.M., Sinnesael, M., Vansteenberge, S., Snoeck, C., Belza, J., Vanhaecke, F., Claeys, P., 2020. Subdaily-Scale Chemical Variability in a *Torreites Sanchezi* Rudist Shell: Implications for Rudist Paleobiology and the Cretaceous Day-Night Cycle. Paleoceanogr. Paleoclimatology 35. https://doi.org/10.1029/2019PA003723

Zachos, J., 2001. Trends, Rhythms, and Aberrations in Global Climate 65 Ma to Present. Science 292, 686–693. https://doi.org/10.1126/science.1059412

Zijlstra, H., 1994. Sedimentology of the late Cretaceous and early Tertiary (tuffaceous) chalk of northwest Europe, Geologica Ultraiectina. Faculteit Aardwetenschappen, Universiteit Utrecht], [Utrecht.

11. Appendix

11.1. RStudio Astrochron Script

Below most relevant parts of the script using the Astrochron application in Rstudio are listed.

```
# Script for data analysis
# Clear workspace
rm(list=ls())
# Load astrochron library
library(astrochron)
# Import data manually and define raw_data
raw_data = Detrended_TiAl_avg3
plot(raw_data, type = 'l', col = 'black')
detrended_data=raw_data

# Plot basic periodogram (spectral density info, e.g. amplitude versus frequency)
periodogram_data = periodogram(detrended_data, genplot = T)
periodogram(raw_data, genplot = T)

# Multitaper Method on detrended_data
mtm_detrended_data = mtm(detrended_data, demean = T, ar1 = T, tbw = 1.5, output = 1, genplot = F,
verbose = F )
# Write mtm_detrended_data to excel-csv file
write.table(mtm_detrended_data, file="mtm_detrended_K_tbw_3.csv", sep=",")
# Plotting of mtm data and confidence levels + labels in function of frequency custom
plot(mtm_detrended_data[,1], mtm_detrended_data[,2],lwd=1.2, type='l',  xlim = c(0,2),ylim = c(0,0.15),
xlab = 'Frequency (1/m)', ylab = 'MTM spectral power', xaxs="i", yaxs = "i")
lines(mtm_detrended_data[,1],mtm_detrended_data$AR1_95_power,type = "l", col = 'red')

# Bandpass filter on detrended_data
bandpass(detrended_data, flow = 1.05, fhigh = 1.45, genplot = T)

# EHA on detrended_data
eha_detrended_data = eha(detrended_data, tbw = 1.5, step = 0.05 , win = 4 , demean = F,detrend = F,
ydir = 1, genplot = 1, verbose = F)
eha_detrended_data = eha(detrended_data, fmin =0 , fmax = 5, tbw = 1.5, step = 0.05 , win = 4 ,
demean = F,detrend = F, ydir = 1, genplot = 4, verbose = F)

# TimeOpt with long-term 405k eccentricity
timeopt_detrended_data = timeOpt(detrended_data, sedmin = 1, sedmax = 3.3, numsed = 1000, linLog
= 1, fit = 1, targetE = c(405, 125, 95), targetP =  c(23.2,18.7),roll=1000, output = 1, verbose = T, genplot =
T, detrend = F)

# eTimeOpt with long-term 405k eccentricity
eTimeOpt(detrended_data,win=5,step=0.1,sedmin=1,sedmax=3.3,numsed = 100, fit = 1, targetE=c(405,
125,95),targetP=c(23.2,18.7),limit=F)
```

```
# Age model for tuning of the stratigraphic record
agemodel=matrix(nrow = 29, ncol = 2, data =
c(12.175,12.875,13.725,14.275,15.275,16.125,16.825,17.425,18.475,19.425,20.225,21.075,21.825,22.57
5,23.375,24.225,24.825,25.625,26.175,26.775,27.575,28.375,29.275,30.175,30.925,31.675,32.475,33.27
5,34.025,20,60,100,140,180,220,260,300,340,380,420,460,500,540,580,620,660,700,740,780,820,860,9
00,940,980,1020,1060,1100,1140))
signal_T1=tune(detrended_data,agemodel,extrapolate = F, genplot = T, verbose = F)
signal_T1[,1]=signal_T1[,1]-signal_T1[1,1]
plot(signal_T1,type="l", xlab = "Floating time (kyr)", ylab = "Virtual proxy", xaxs = "i")
write.table(signal_T1, file="Tuned Series TiAl.csv", sep=",")

# Linear interpolation and MTM power spectrum of time series
interptsign=linterp(signal_T1)
mtm_signal_T1=mtm(interptsign,demean = T, ar1 = T, tbw = 2,output = 1, xmax = 0.07, genplot = F,
verbose = F)
plot(mtm_signal_T1[,1],mtm_signal_T1[,2],lwd = 1.2, type="l", xlim = c(0,0.07), xlab = 'Frequency
(1/kyr)', ylab  = 'MTM spectral power', xaxs="i")
lines(mtm_signal_T1[,1],mtm_signal_T1$AR1_95_power,type = "l", col = rgb(8/255,164/255,172/255))
write.table(mtm_signal_T1, file="mtm tuned series TiAl.csv", sep=",")

# Bandpass filter on tuned, linearly interpolated time series

bandpass(interptsign, flow = 0.006, fhigh = 0.012, genplot = T)

bandpass(interptsign, flow = 0.022, fhigh = 0.027, genplot = T)

bandpass(interptsign, flow = 0.046, fhigh = 0.052, genplot = T)

write.table(interptsign, file="Tuned Series TiAlinterp.csv", sep=",")
```

11.2. Fully assigned µXRF spectrum

Assigned µXRF spectrum of sample HAL18_A_30.85a using Bruker M4 Esprit software.

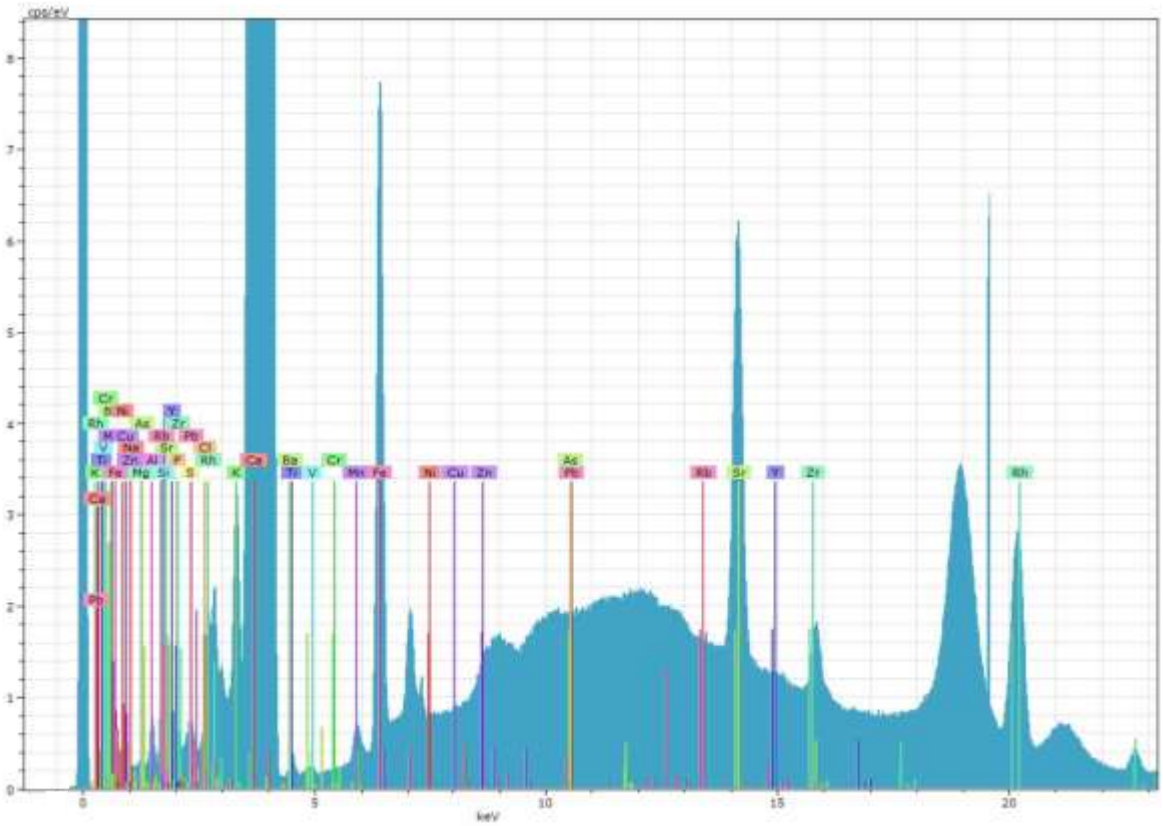

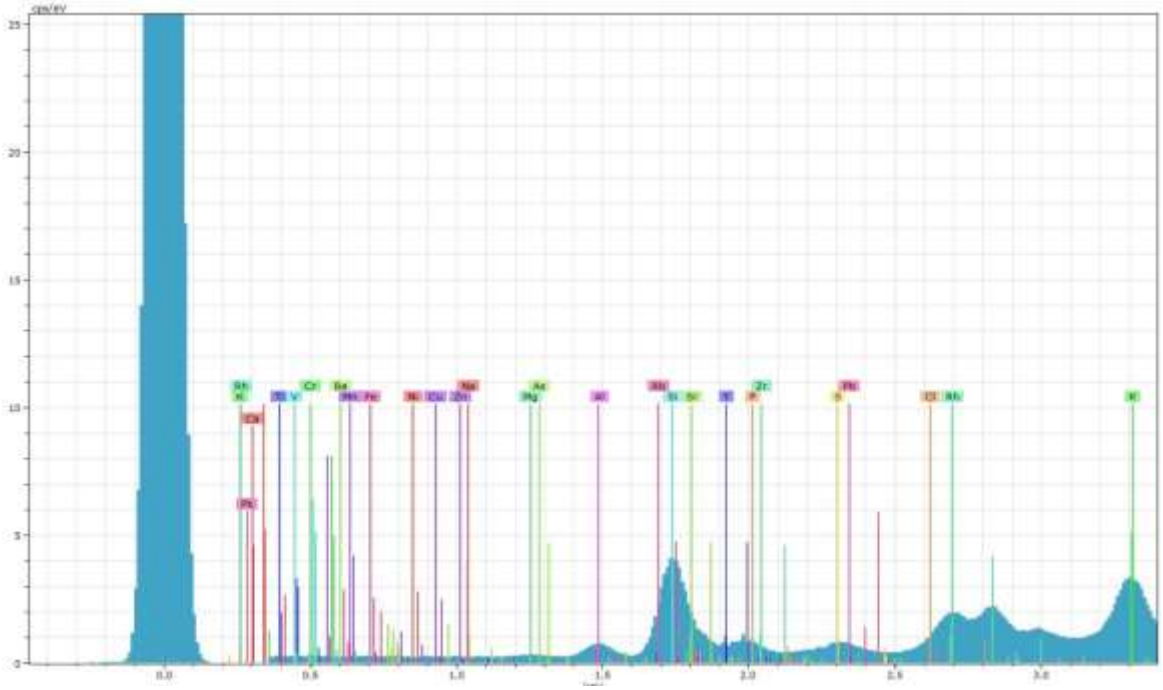

11.3. 3D PCA Loading Plots

PCA Loading Plots (PC1,PC2 and PC3 accounting for 62% of all variance) for all elemental concentrations for the 5 cm-high resolution sampled interval from 11.75 m to 34.50 m.

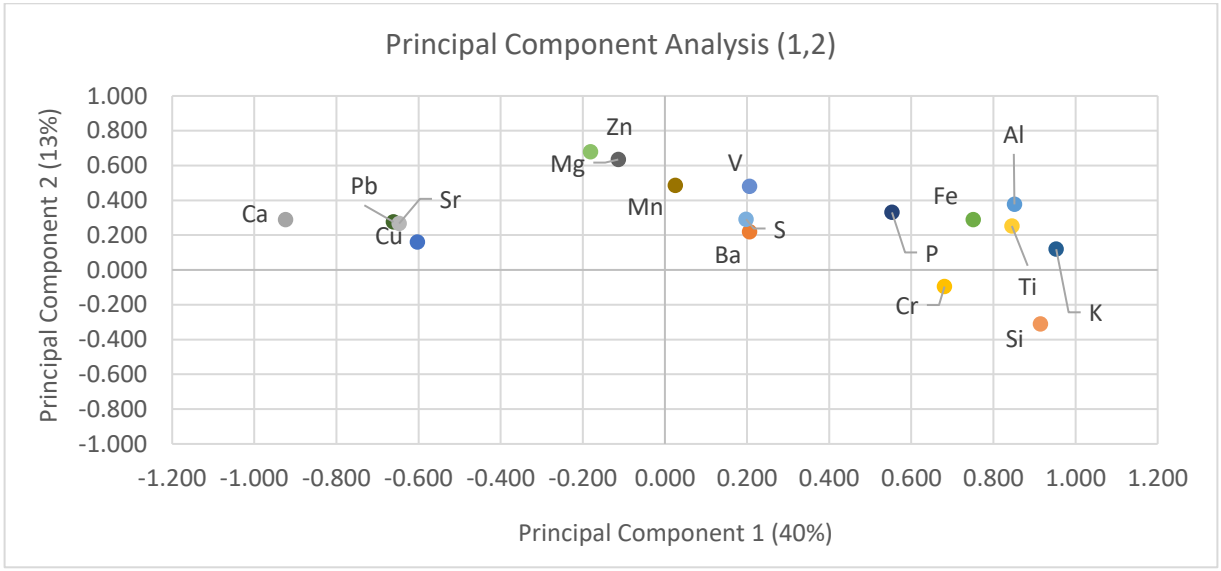

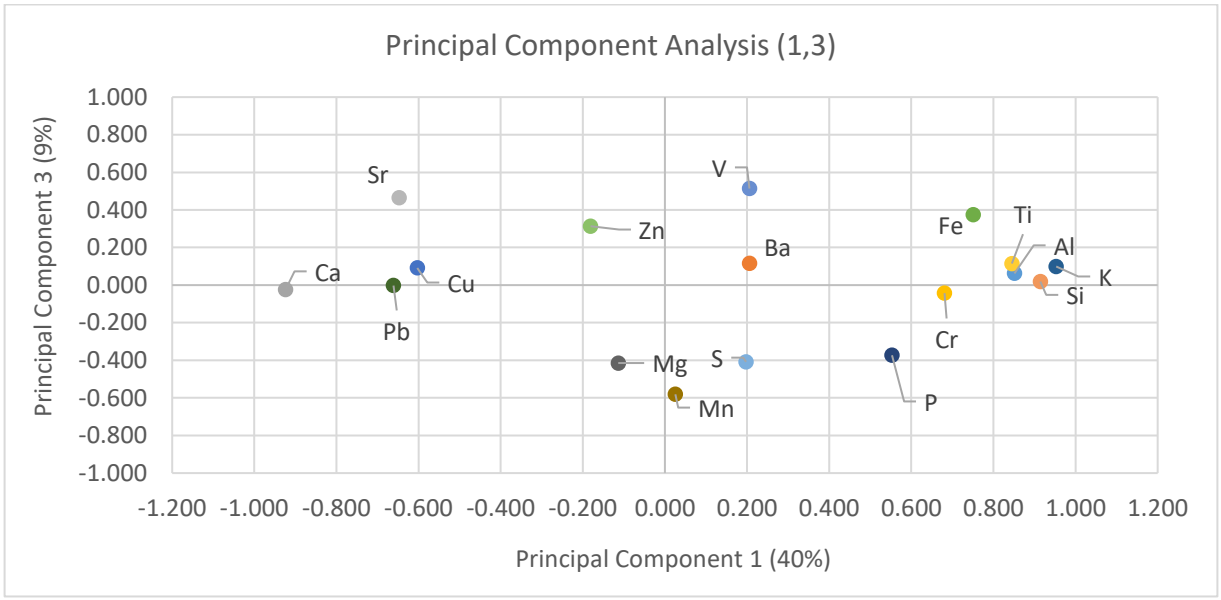

k

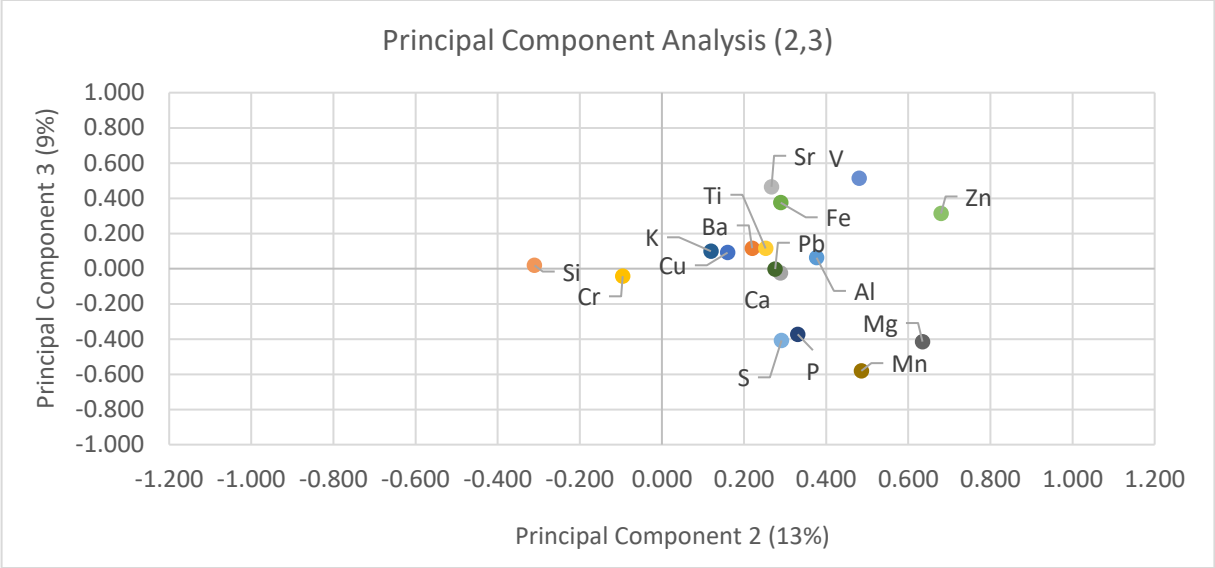

PCA Loading Plots (PC1,PC2 and PC3 accounting for 73% of all variance) for all elemental concentrations and MS for the 1 m-low resolution data set.

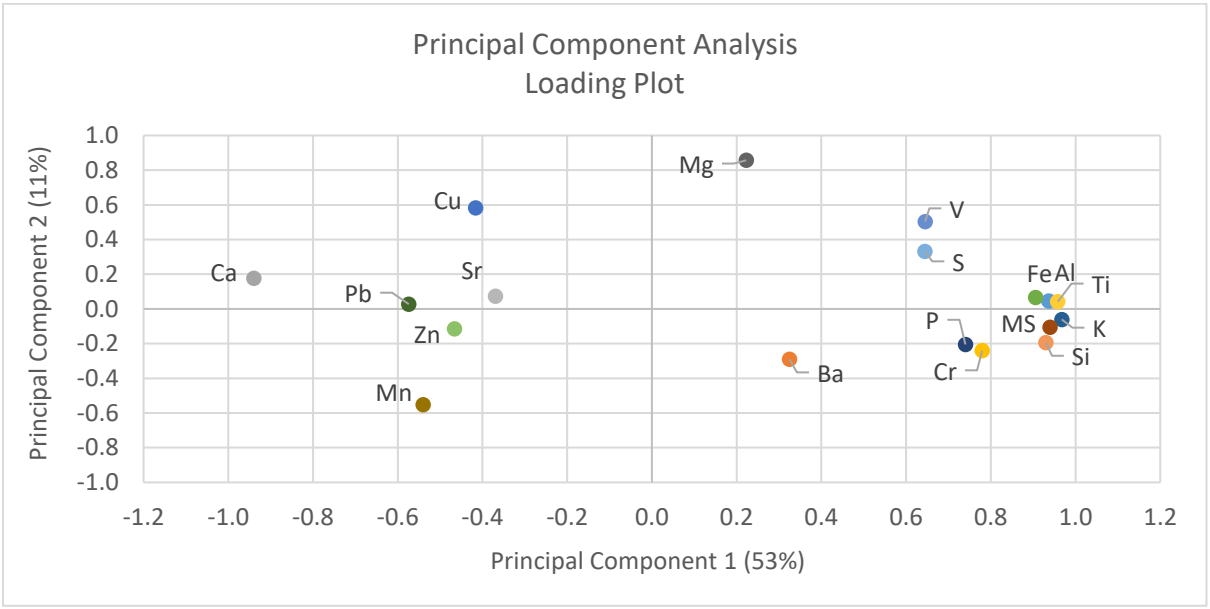

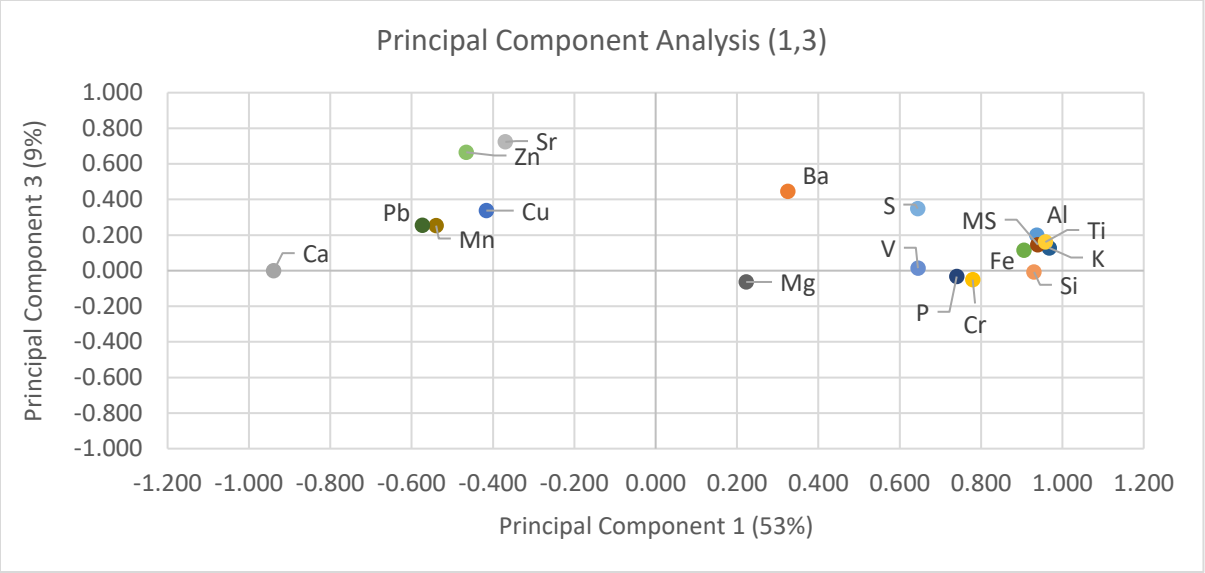
Principal Component Analysis (1,3)
Principal Component 3 (9%)
Principal Component 1 (53%)
1.000
0.800
0.600
0.400
0.200
0.000
-0.200
-0.400
-0.600
-0.800
-1.000
-1.200 -1.000 -0.800 -0.600 -0.400 -0.200 0.000 0.200 0.400 0.600 0.800 1.000 1.200
Sr
Zn
Ba
Pb
Cu
S
MS
Al
Ti
Mn
V
Fe
K
Ca
Mg
Si
P
Cr

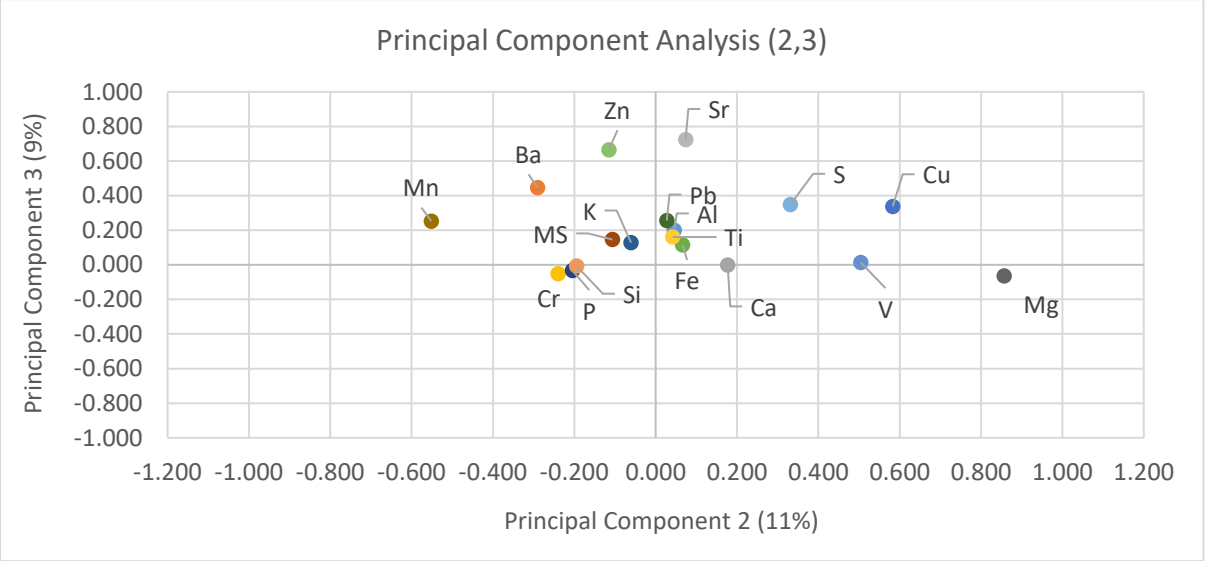
Principal Component Analysis (2,3)
Principal Component 3 (9%)
Principal Component 2 (11%)
1.000
0.800
0.600
0.400
0.200
0.000
-0.200
-0.400
-0.600
-0.800
-1.000
-1.200 -1.000 -0.800 -0.600 -0.400 -0.200 0.000 0.200 0.400 0.600 0.800 1.000 1.200
Zn
Sr
Ba
S
Cu
Mn
Pb
K
Al
MS
Ti
Fe
Cr
Si
P
Ca
V
Mg

m

11.4. Geochemical Confirmation of Vijlen Member – Lixhe 1 Member Transition

Variation in trends observed along the stratigraphic interval 11.75 cm – 34.50 cm, exemplified for calcium but is similar for silicium.

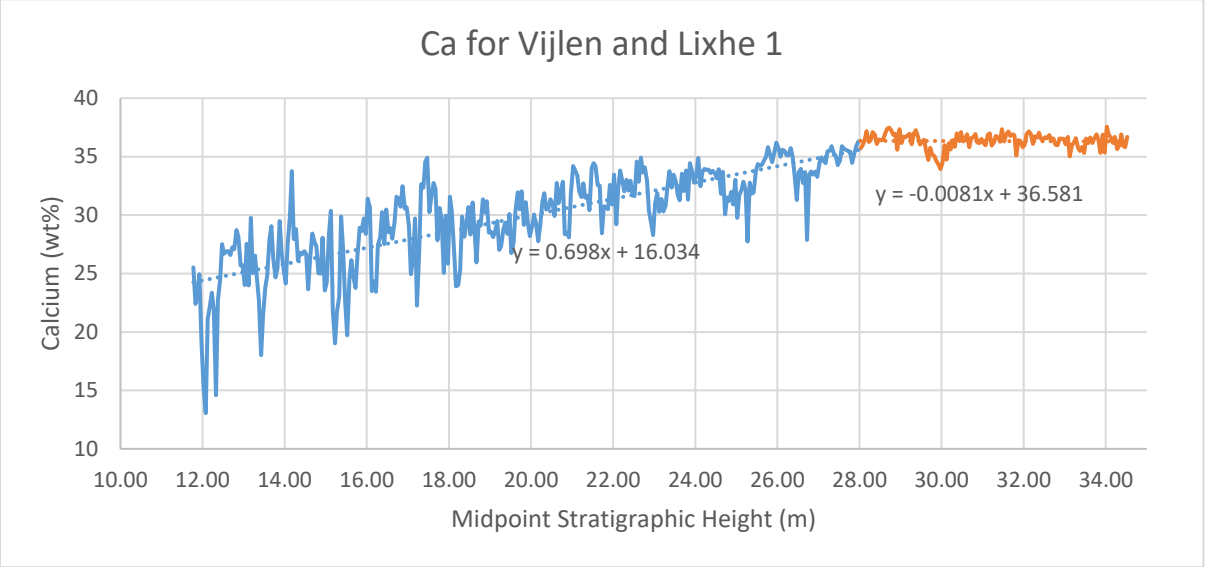

11.5. Correlation between calcium and silicium – Cross-plot

Calcium and Silicium cross-plot for the stratigraphic interval 11.75 cm – 34.50 cm.

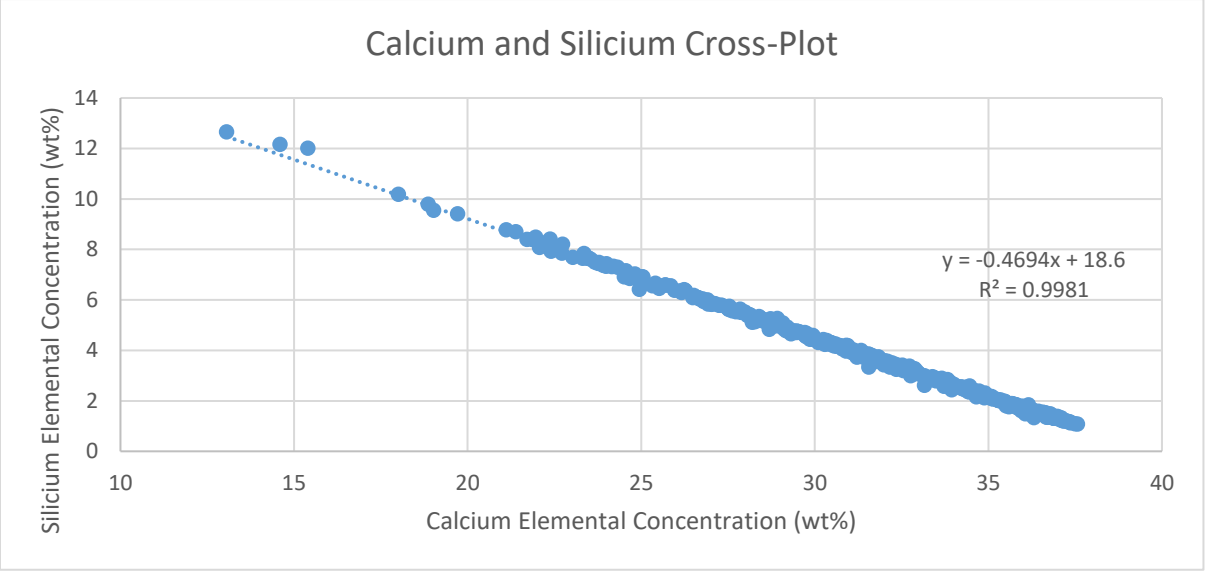

n

11.6. References to Additional Files – Master Data

MSc Master Data µXRF_v.6 used for re-calibration and outlier identification and removal.

MSc Master Data MS used for outlier identification and removal.

o